Advanced Mission Scenarios of the Three-Body Problem

Vladimir S. Aslanov

2026

- A brief overview is provided of the author's book and articles (2019–2026), in which possible scenarios for future space missions are discussed
- These preliminary studies aim to implement cost-effective space programmes and promote the responsible use of outer space
- The issues discussed could form the basis of further detailed research

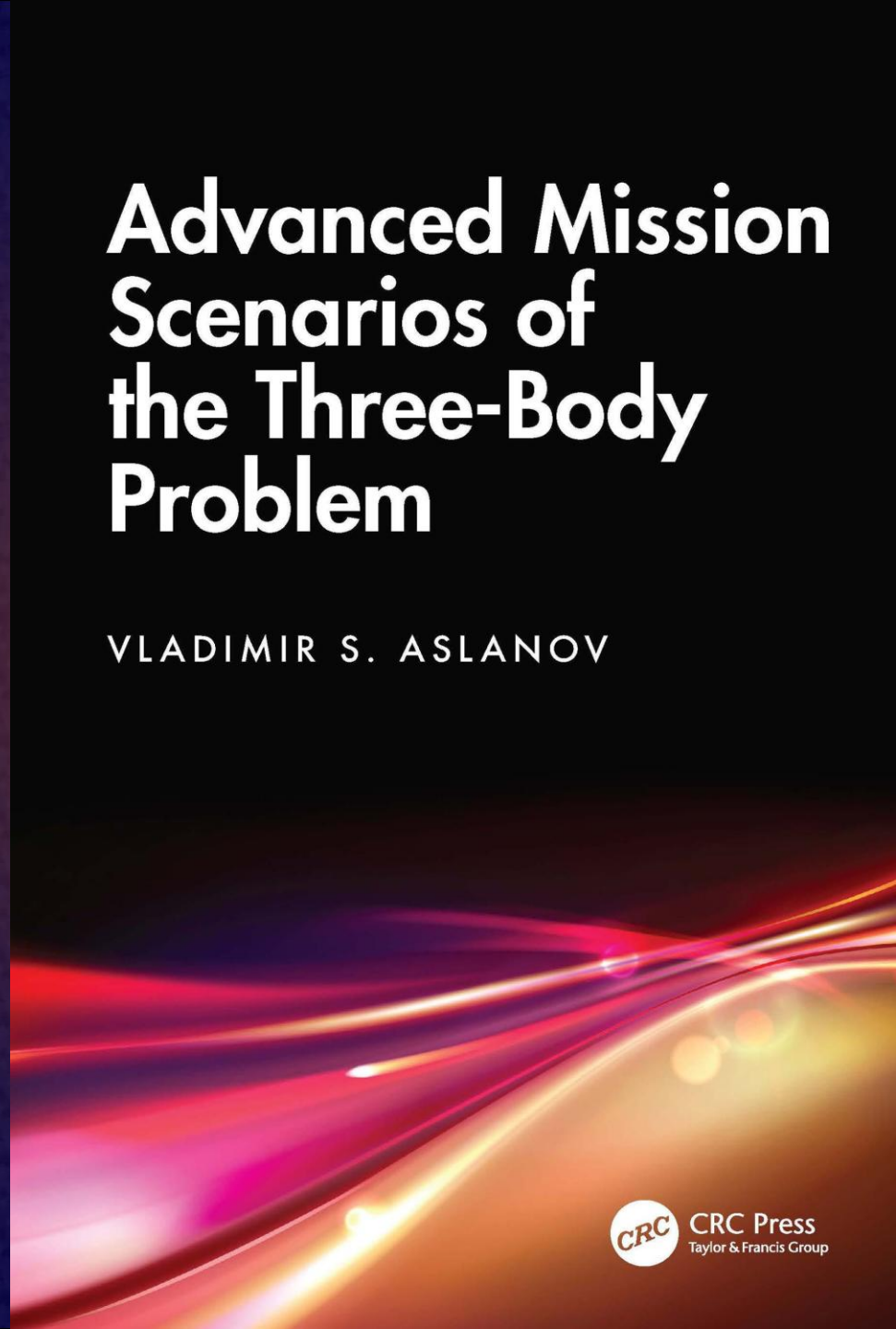

ABSTRACT

Advanced Mission Scenarios of the Three-Body Problem introduces one of the classical problems of celestial mechanics through the prism of the problems and challenges of modern astrodynamics. It examines current issues in modern astronautics related to the study and colonization of Mars, exploration of the Moon, space debris, and contactless space transportation technologies.

Describing the dynamics of space tether systems and space elevators in the gravitational field created by two massive bodies, the book presents an original technology for contactless gravitational transportation of space debris using a heavy gravitational collector. It provides practical recommendations for the implementation of new pioneering missions related to tether transportation in the vicinity of libration points, the construction of space elevators on planetary moons, and contactless electrostatic and gravitational transportation, including in the context of the space debris problem.

This book is intended for space systems and spacecraft engineering industry experts and researchers studying space transportation and modern challenges in astronautics.

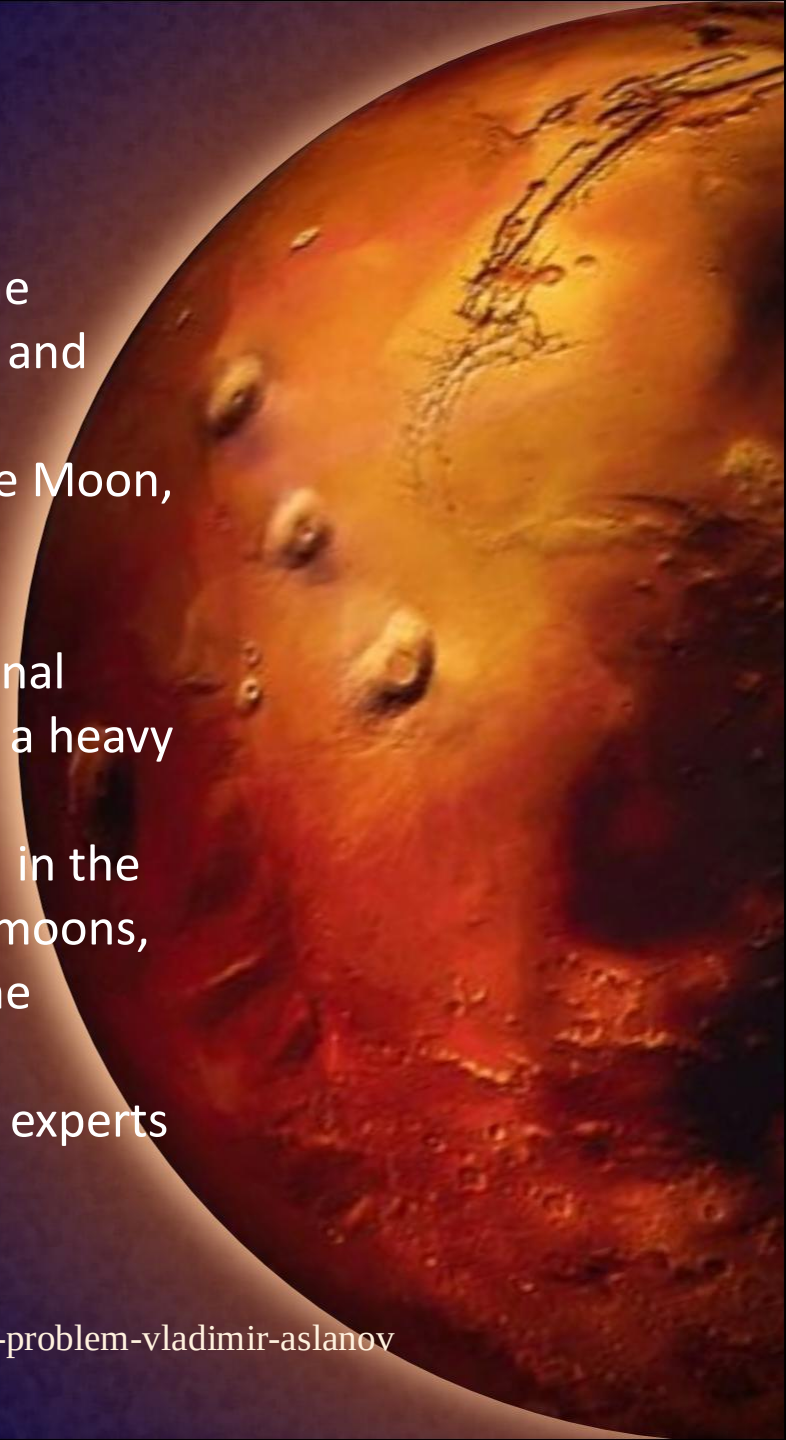

https://www.taylorfrancis.com/books/mono/10.1201/9781003643357/advanced-mission-scenarios-three-body-problem-vladimir-aslanov

Contents

Chapter 1

Classical Approaches and Methods for Studying the Three-Body Problem

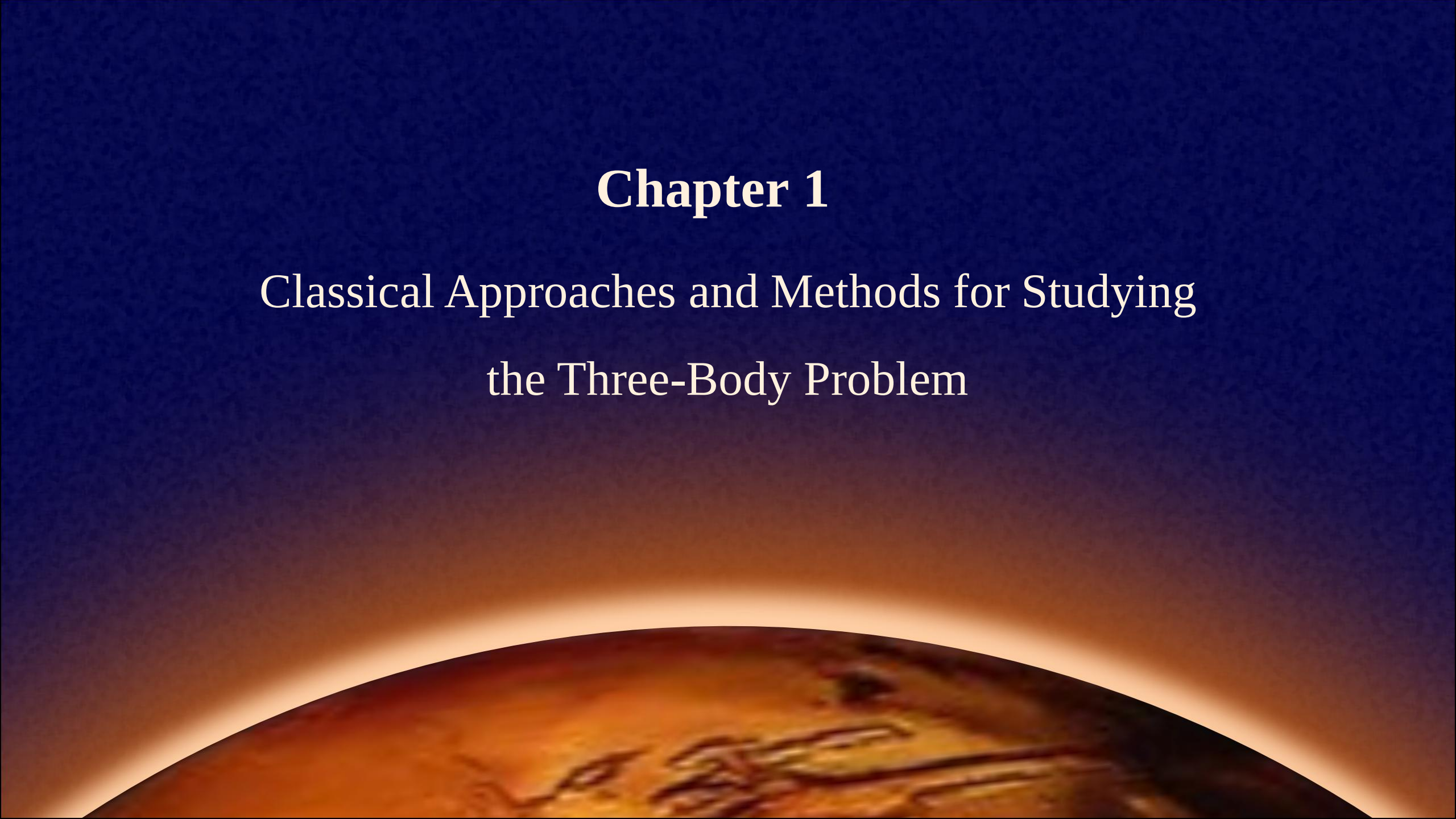

The Three-Body Problem

$$\ddot{\mathbf{r}}_1 = -Gm_2\frac{\mathbf{r}_1-\mathbf{r}_2}{|\mathbf{r}_1-\mathbf{r}_2|^3} - Gm_3\frac{\mathbf{r}_1-\mathbf{r}_3}{|\mathbf{r}_1-\mathbf{r}_3|^3}$$

$$\ddot{\mathbf{r}}_2 = -Gm_1\frac{\mathbf{r}_2-\mathbf{r}_1}{|\mathbf{r}_1-\mathbf{r}_2|^3} - Gm_3\frac{\mathbf{r}_2-\mathbf{r}_3}{|\mathbf{r}_2-\mathbf{r}_3|^3} \qquad (1.1)$$

$$\ddot{\mathbf{r}}_3 = -Gm_1\frac{\mathbf{r}_3-\mathbf{r}_1}{|\mathbf{r}_1-\mathbf{r}_3|^3} - Gm_2\frac{\mathbf{r}_3-\mathbf{r}_2}{|\mathbf{r}_2-\mathbf{r}_3|^3}$$

$$\frac{m_1\mathbf{r}_1+m_2\mathbf{r}_2+m_3\mathbf{r}_3}{m_1+m_2+m_3} = \mathbf{0} \qquad (1.2)$$

- $m_1,\ m_2,\ m_3$ are masses of the material points
- $G = 6.67430(15)\cdot 10^{-11}\ \mathrm{m^3 s^{-2} kg^{-1}}$ is the gravitational constant
- $\mathbf{r}_i$ is the position vector of *i*-th point

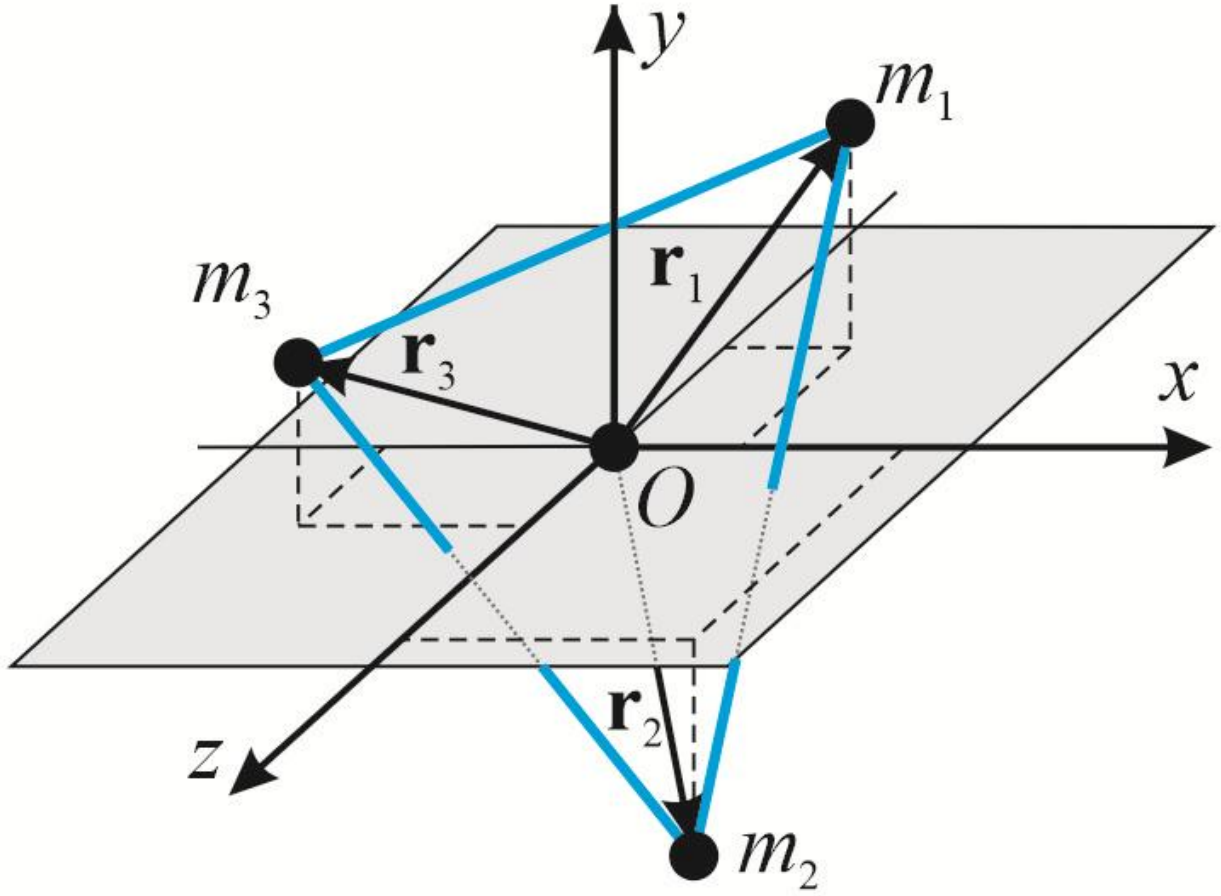

Figure 1.1. The three body problem.

The Restricted Three-Body Problem

$$M_1 \geq M_2 \gg m \qquad (1.3)$$

$$r = \frac{p}{1 + e\cos f} \qquad (1.4)$$

$$\ddot{x} - 2\dot{f}\dot{y} - \ddot{f}y - \dot{f}^2 x = \frac{\partial W}{\partial x}$$

$$\ddot{y} + 2\dot{f}\dot{x} + \ddot{f}x - \dot{f}^2 y = \frac{\partial W}{\partial y} \qquad (1.5)$$

$$\ddot{z} = \frac{\partial W}{\partial z}$$

$$\ddot{f} = -\frac{2c^2 e}{p^4}\sin f\,(1 + e\cos f)^3$$

- p is the semilatus rectum
- e is the eccentricity of the two-body orbit of the primaries
- f is the true anomaly

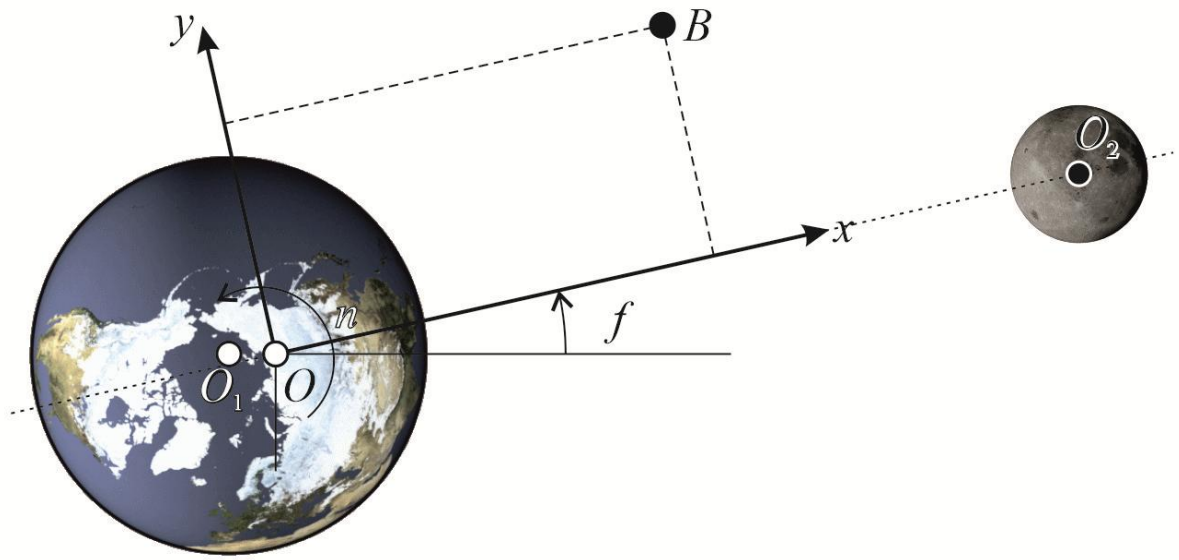

Figure 1.2. The *Oxyz* reference frame.

- $W = U / m$
- U is potential of the gravitational field

Nechvile's variables

$$x = r\xi \qquad y = r\eta \qquad z = r\zeta \qquad (1.6)$$

$$\ddot{x} - 2\dot{f}\dot{y} - \ddot{f}y - \dot{f}^2 x = \frac{\partial W}{\partial x}$$

$$\ddot{y} + 2\dot{f}\dot{x} + \ddot{f}x - \dot{f}^2 y = \frac{\partial W}{\partial y}$$

$$\ddot{z} = \frac{\partial W}{\partial z} \qquad (1.5)$$

$$\ddot{f} = -\frac{2c^2 e}{p^4}\sin f\,(1 + e\cos f)^3$$

$$\xi'' - 2\eta' = \frac{1}{1+e\cos f}\frac{\partial \Omega}{\partial \xi}$$

$$\eta'' + 2\xi' = \frac{1}{1+e\cos f}\frac{\partial \Omega}{\partial \eta} \qquad (1.7)$$

$$\zeta'' = \frac{1}{1+e\cos f}\frac{\partial \Omega}{\partial \zeta}$$

- $\Omega = \frac{1}{2}(\xi^2 + \eta^2) - \frac{1}{2}e\zeta^2\cos f + \frac{1-\mu}{\sqrt{(\xi+\mu)^2 + \eta^2 + \zeta^2}} + \frac{\mu}{\sqrt{(\xi+\mu-1)^2 + \eta^2 + \zeta^2}}$

Jacobi Integral

$$r = p = const \qquad \dot{f} = n = \frac{c}{p^2} = const \qquad e = 0 \qquad (1.8)$$

$$\ddot{x} - 2n\dot{y} - n^2 x = \frac{\partial W_C}{\partial x}$$

$$\ddot{y} + 2n\dot{x} - n^2 y = \frac{\partial W_C}{\partial y} \qquad (1.9)$$

$$\ddot{z} = \frac{\partial W_C}{\partial z}$$

$$C = -V_r^2 + n^2(x^2 + y^2) + 2W_C$$

$$\xi'' - 2\eta' = \frac{\partial \Omega_C}{\partial \xi}$$

$$\eta'' + 2\xi' = \frac{\partial \Omega_C}{\partial \eta} \qquad (1.10)$$

$$\zeta'' = \frac{\partial \Omega_C}{\partial \zeta}$$

$$\bar{C} = -(\xi'^2 + \eta'^2 + \zeta'^2) + 2\Omega_C$$

Jacobi Integral

- $W_C = G\left(\frac{M_1}{\sqrt{(x+\mu p)^2 + y^2 + z^2}} + \frac{M_2}{\sqrt{(x-(1-\mu)p)^2 + y^2 + z^2}}\right)$

- $\Omega_C = \frac{1}{2}(\xi^2 + \eta^2) + \frac{1-\mu}{\sqrt{(\xi+\mu)^2 + \eta^2 + \zeta^2}} + \frac{\mu}{\sqrt{(\xi+\mu-1)^2 + \eta^2 + \zeta^2}}$

Lagrange Libration Points

$$\frac{\partial \Omega}{\partial \xi} = \xi - \frac{(1-\mu)(\xi+\mu)}{((\xi+\mu)^2+\eta^2+\zeta^2)^{3/2}} - \frac{\mu(\xi+\mu-1)}{((\xi+\mu-1)^2+\eta^2+\zeta^2)^{3/2}} = 0$$

$$\frac{\partial \Omega}{\partial \eta} = \eta - \frac{(1-\mu)\eta}{((\xi+\mu)^2+\eta^2+\zeta^2)^{3/2}} - \frac{\mu\eta}{((\xi+\mu-1)^2+\eta^2+\zeta^2)^{3/2}} = 0 \qquad (1.11)$$

$$\frac{\partial \Omega}{\partial \zeta} = -\zeta e \cos f - \frac{(1-\mu)\zeta}{((\xi+\mu)^2+\eta^2+\zeta^2)^{3/2}} - \frac{\mu\zeta}{((\xi+\mu-1)^2+\eta^2+\zeta^2)^{3/2}} = 0$$

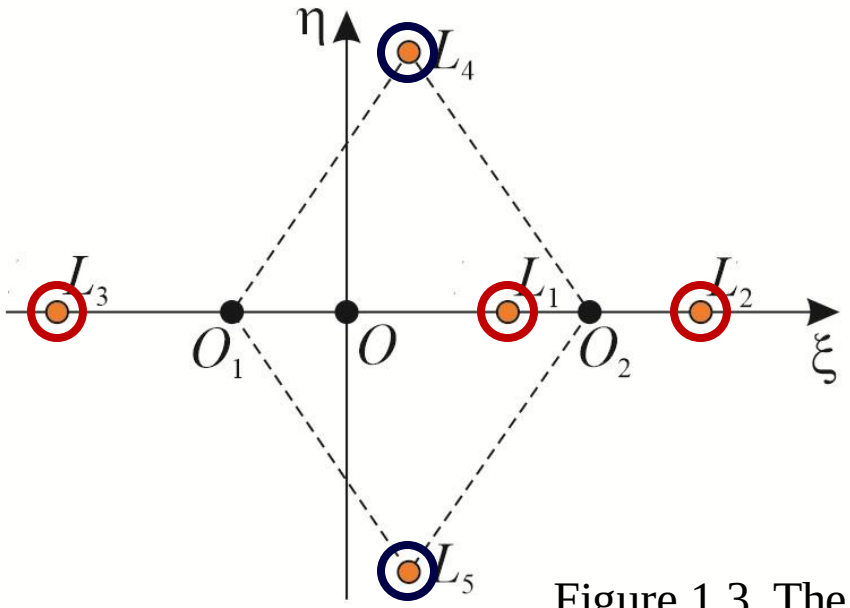

Collinear points

Triangular points

Figure 1.3. The libration points.

Lagrange Libration Points

$$F(\xi^*) = \xi^* - \mu\frac{\left|\mu+\xi^*-1\right|}{\left(-1+\mu+\xi^*\right)^3} - (1-\mu)\frac{\left|\mu+\xi^*\right|}{\left(\mu+\xi^*\right)^3} = 0 \qquad (1.12)$$

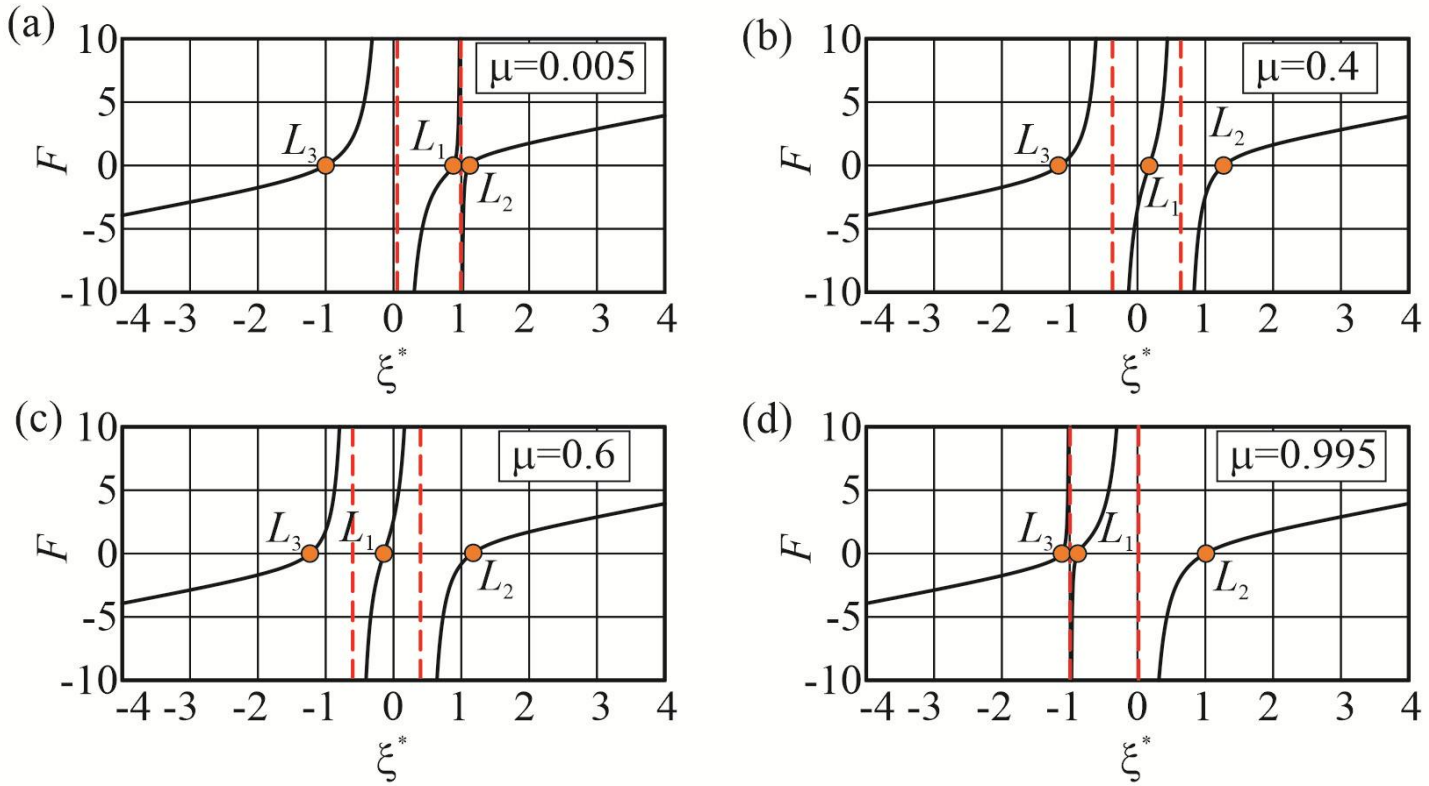

Figure 1.4. The function (1.12) constructed for various values of μ.

Hill's Radius

The **Hill sphere** is the space around an astronomical object (such as a planet) in which it is able to hold its satellite despite the gravitational pull of the object around which it orbits.

$$r_H \approx r\left(\frac{\mu}{3}\right)^{1/3} \approx a(1-e)\left(\frac{\mu}{3}\right)^{1/3} \approx a\left(\frac{\mu}{3}\right)^{1/3} \qquad (1.13)$$

Zero-Relative-Velocity Surfaces

$$\xi^2+\eta^2+\frac{2(1-\mu)}{\sqrt{(\xi+\mu)^2+\eta^2+\zeta^2}}+\frac{2\mu}{\sqrt{(\xi+\mu-1)^2+\eta^2+\zeta^2}}=\bar{C} \qquad (1.14)$$

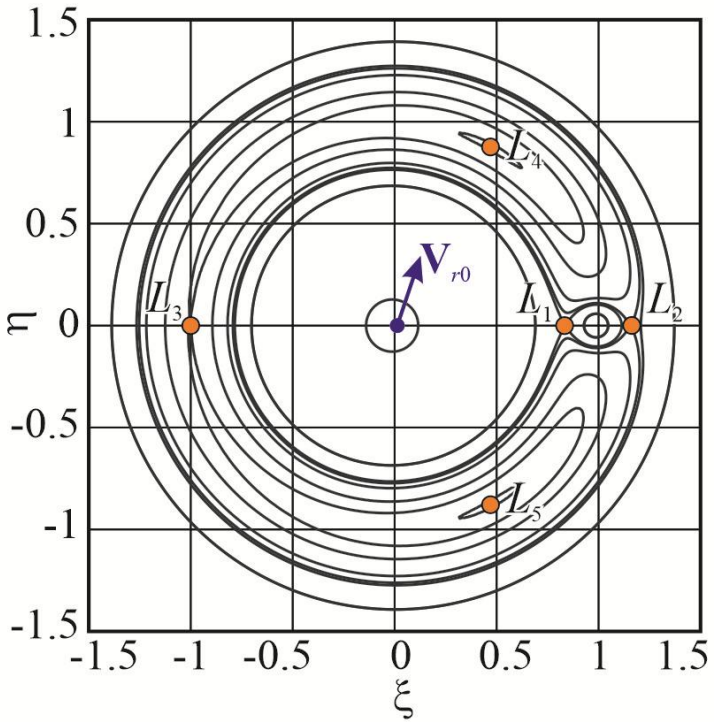

Figure 1.5. Intersection of zero-velocity surfaces with the plane $\zeta = 0$ for different values of Jacoby integral $\bar{C}$.

Periodic Orbits

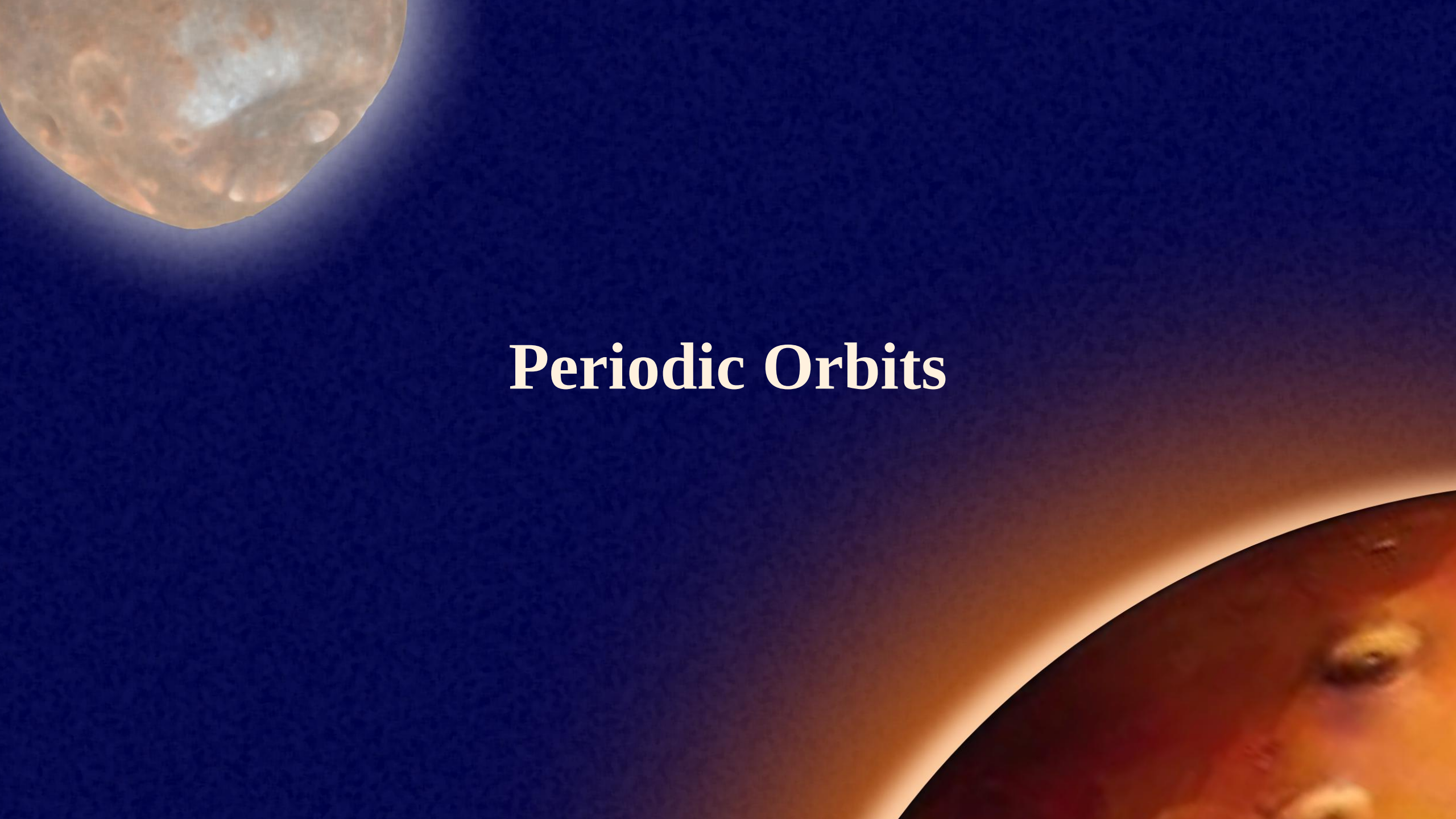

Quasi-satellite orbits

A **quasi-satellite orbit** (QSO) in a planet-moon system can be defined as an orbit that is in resonance with the moon's orbital motion around the planet. These types of orbits are located farther away than the coplanar libration points L_1, L_2.

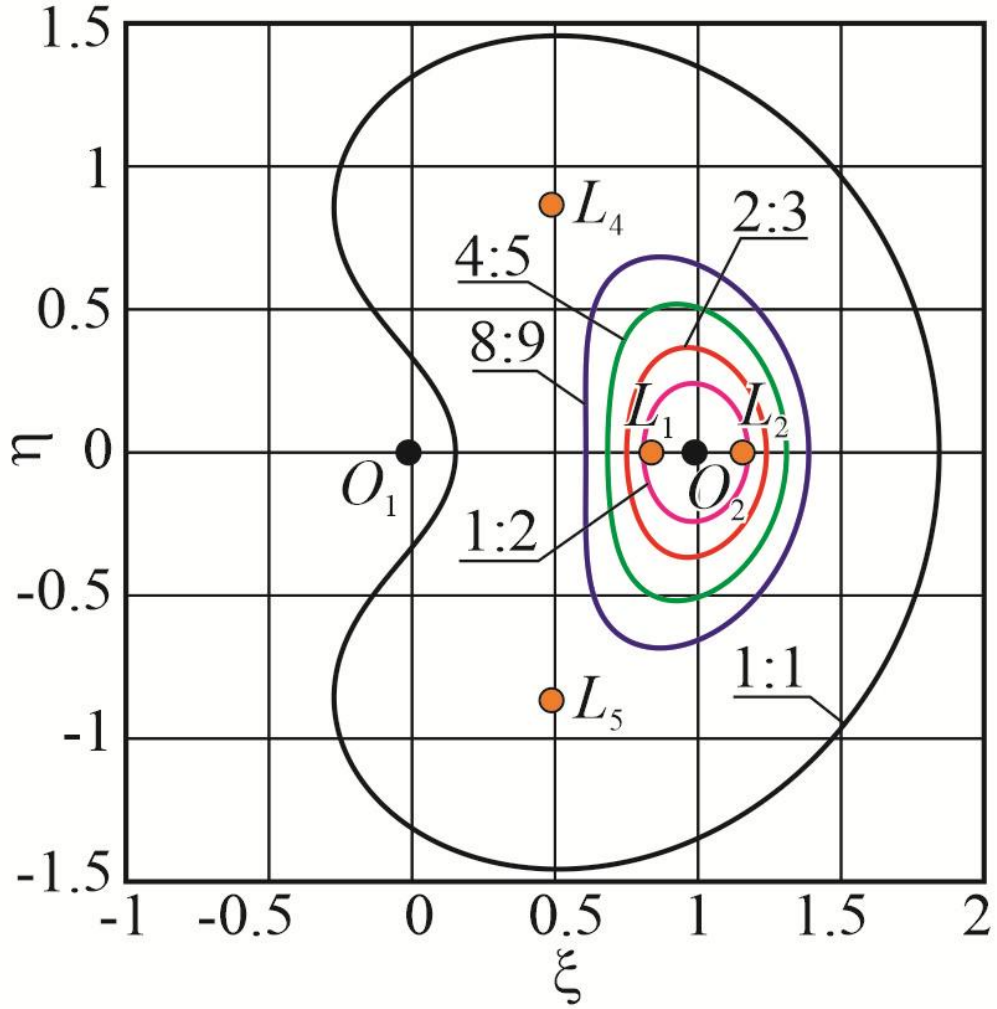

Figure 1.6. Quasi-satellite orbits around the Moon obtained for different resonance ratios.

Chaos in the restricted three-body problem

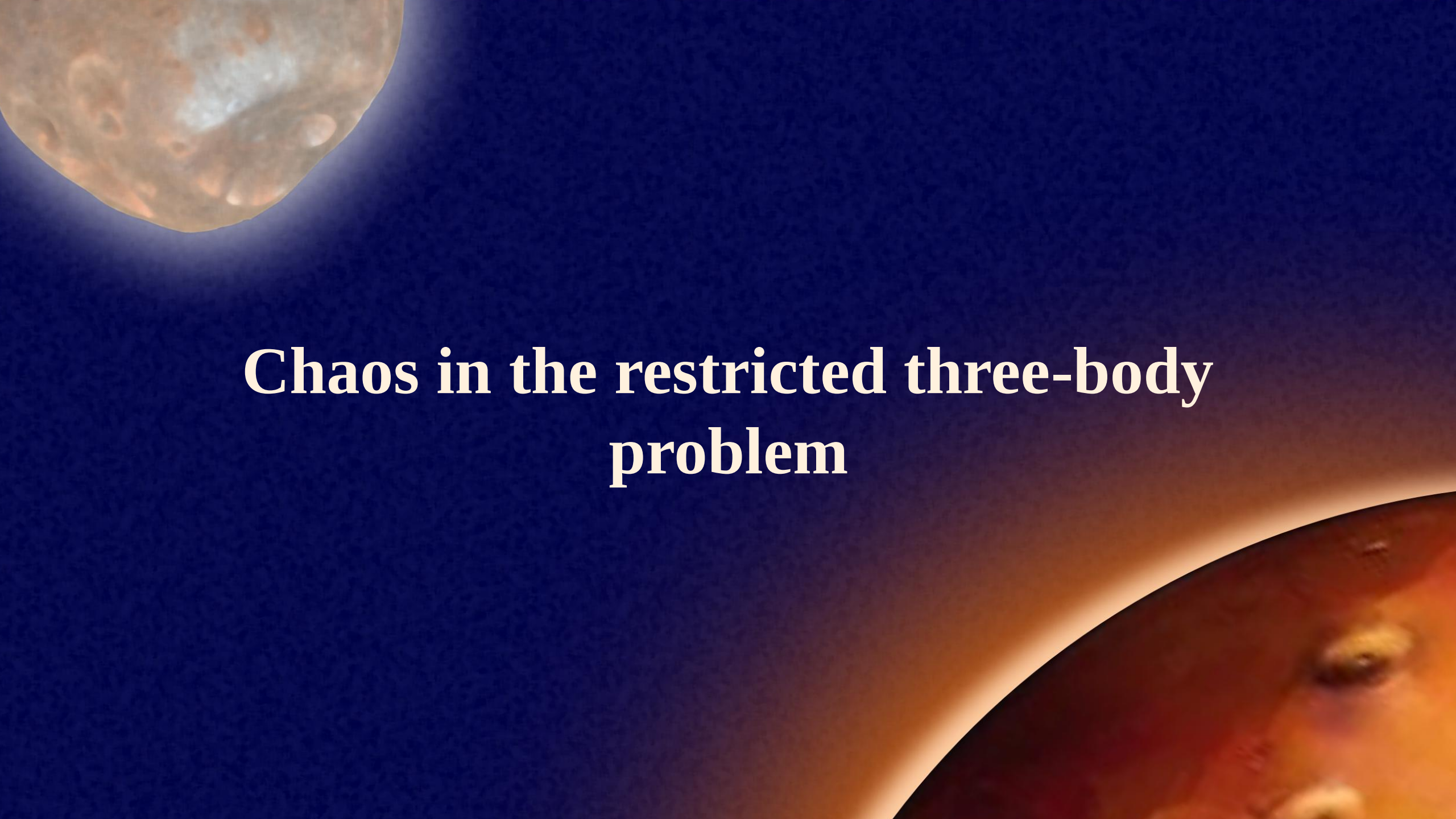

Chapter 2

Space Tether Systems

for Mars-Phobos Exploration

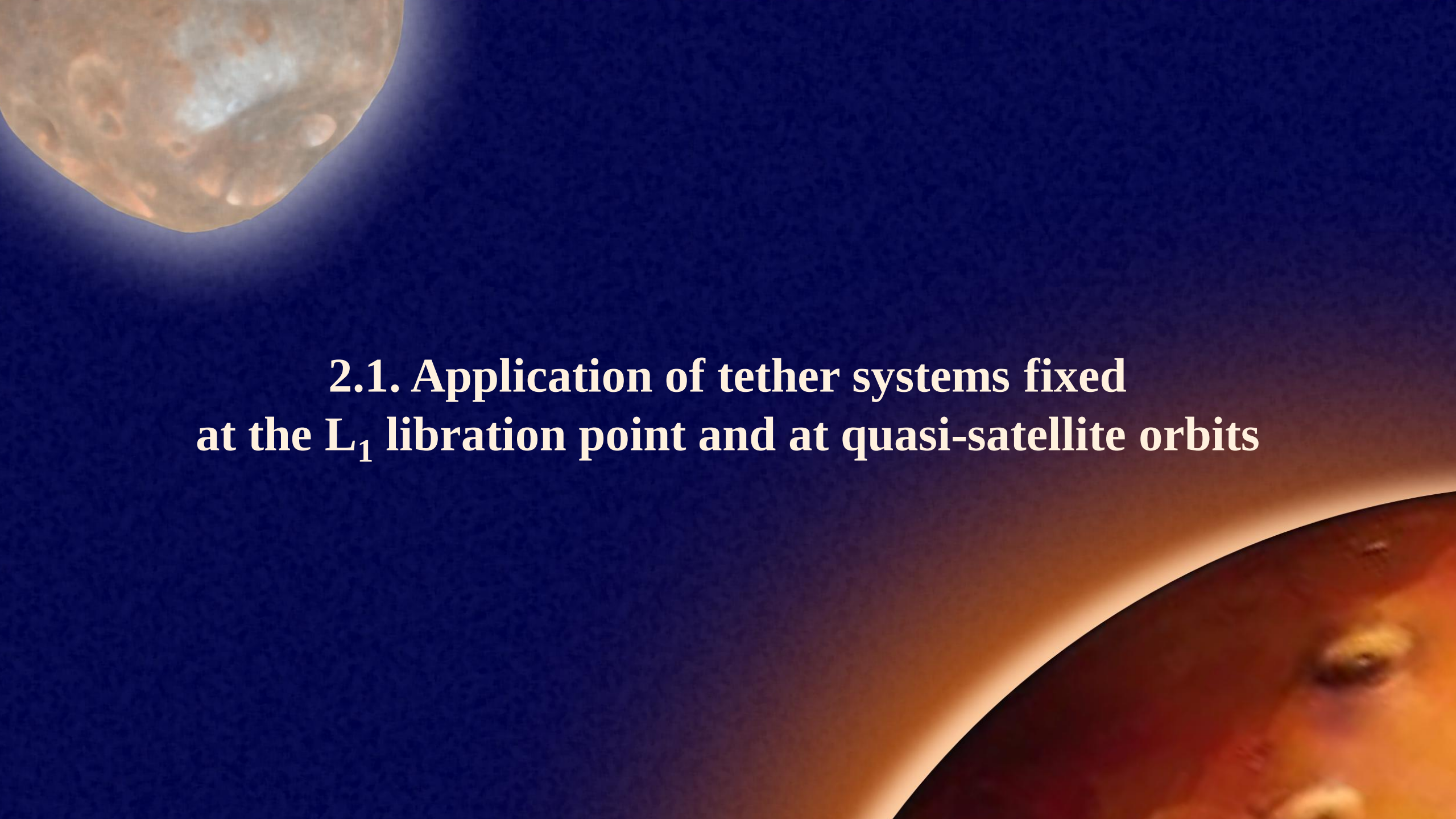

2.1. Application of tether systems fixed at the L_1 libration point and at quasi-satellite orbits

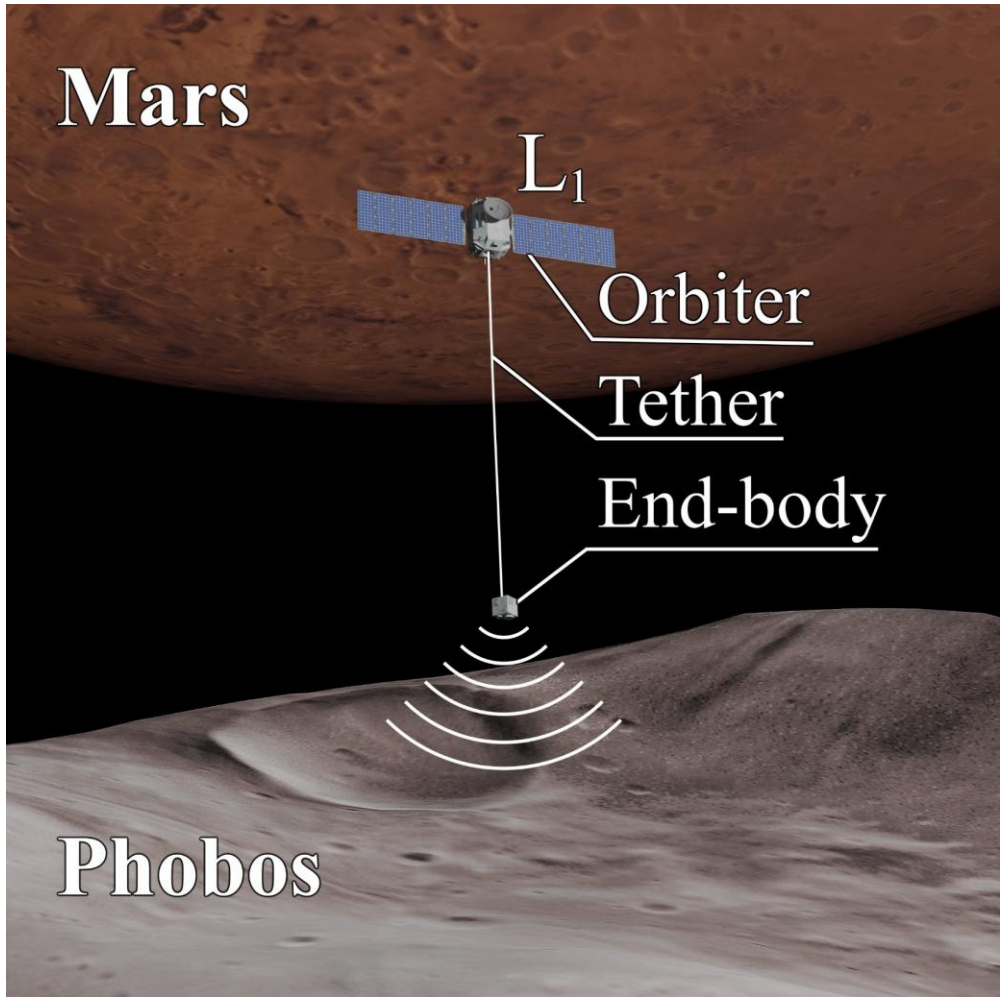

Figure 2.1. Concept art of PHLOTE mission to explore the surface of Phobos.

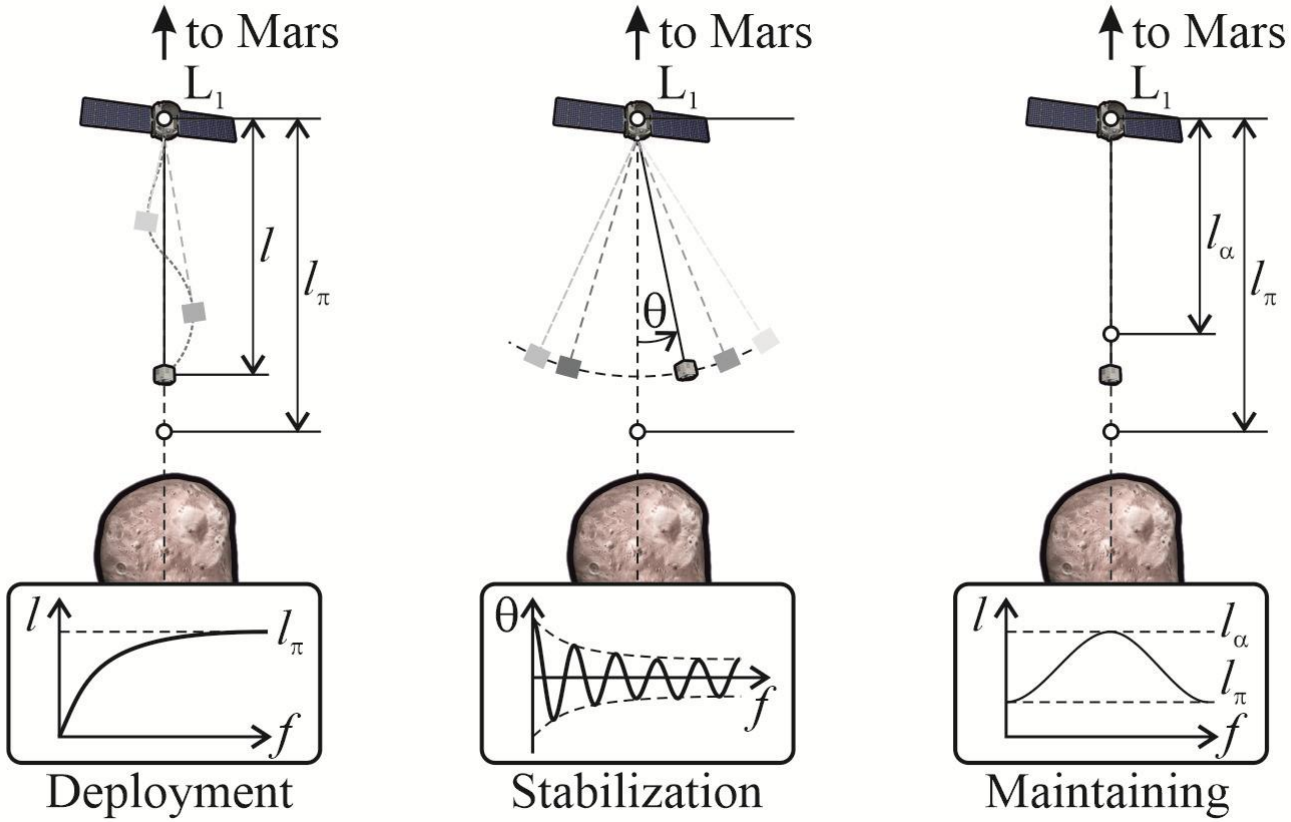

Figure 2.2. The scheme of the proposed mission to explore the surface of Phobos.

2.2. A space tether system as a pendulum fixed at the L1 libration point

Constant-length tether oscillations

$$L = const \qquad l = const \qquad (2.1)$$

$$W(\theta) = -\frac{\sigma\cos\theta}{l} - \frac{\mu}{l^2\sqrt{l^2+(\mu-1+\sigma)^2+2l(\mu-1+\sigma)\cos\theta}} - \frac{1-\mu}{l^2\sqrt{l^2+(\mu+\sigma)^2+2l(\mu+\sigma)\cos\theta}} \qquad (2.2)$$

- $(l,\ \theta)$ are polar coordinates of the small body
- $W(\theta)$ is the dependence of the potential energy W on the angle θ

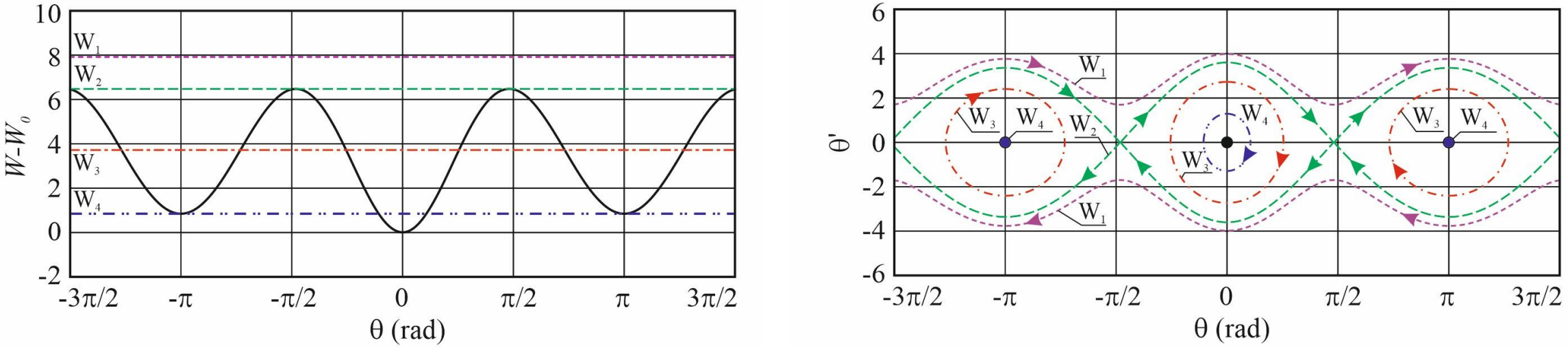

Figure 2.3. Dependences of the potential energy and the corresponding phase portrait for various levels of energy for the tether length.

The tension force control for the tether deployment, angular stabilization and maintaining the required distance above the moon surface

Stage 1. Tether deployment from the orbiter to a given length. At the end of the deployment, the tether rate should be zero.

$$T_1 = k_{1l}\left(l - l_f\right) + k_{1V} l' \tag{2.3}$$

Stage 2. The angular stabilization of the end body relative to the lower stable equilibrium position ($\theta = 0$) closest to the moon's surface.

$$T_2 = k_{2l}\left[l - \left(l_f + \lambda\theta' \sin\theta\right)\right] + k_{2V} l' \tag{2.4}$$

Stage 3. Maintaining a constant altitude between the lower end of the tether system and the moon's surface to counteract the change in altitude due to pulsation in the L1 libration point position.

$$T_3 = k_{3l}\left[l - \left(\frac{1-\sigma}{1+e\cos f} - \delta\right)\right] + k_{3V} l' \tag{2.5}$$

Numerical simulation of the mission to explore the surface of Phobos under the L1 libration point

Stage 1

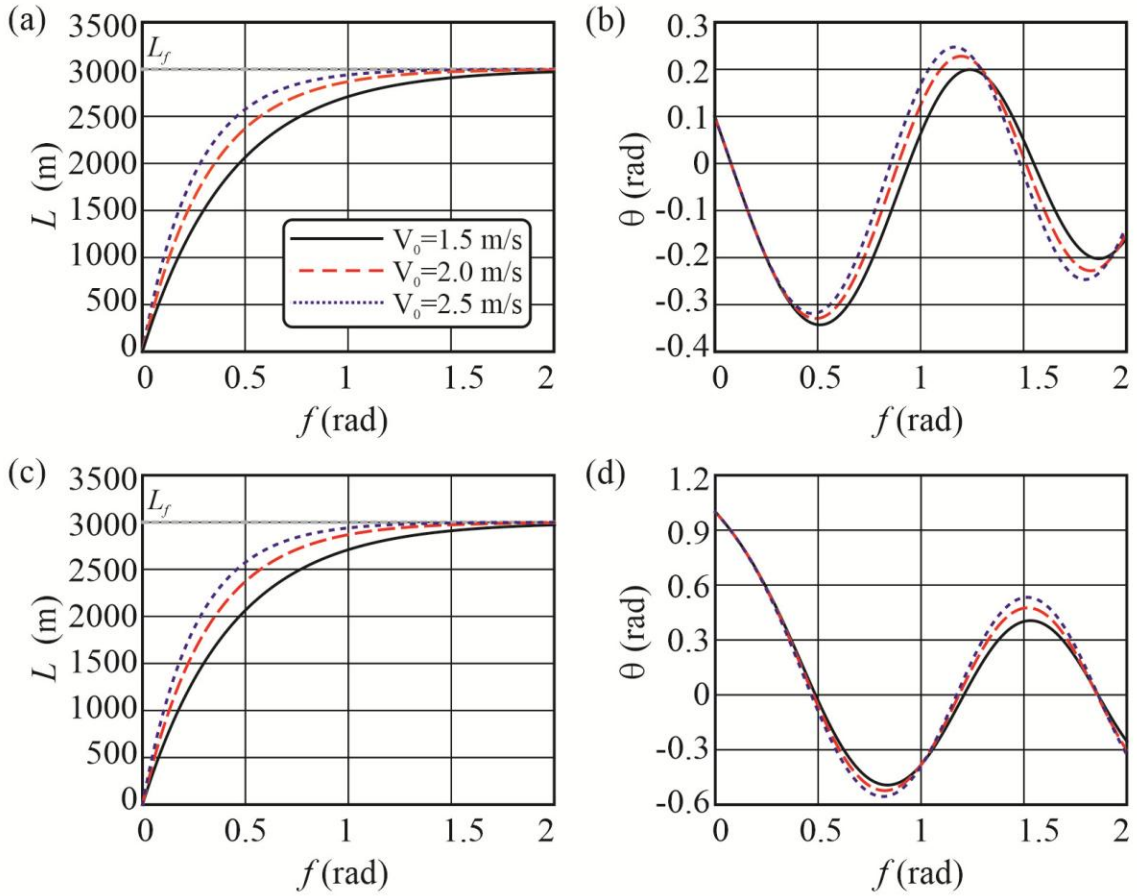

Figure 2.4. The tether deployment length and the oscillation angle of the tether for the ejection velocity.

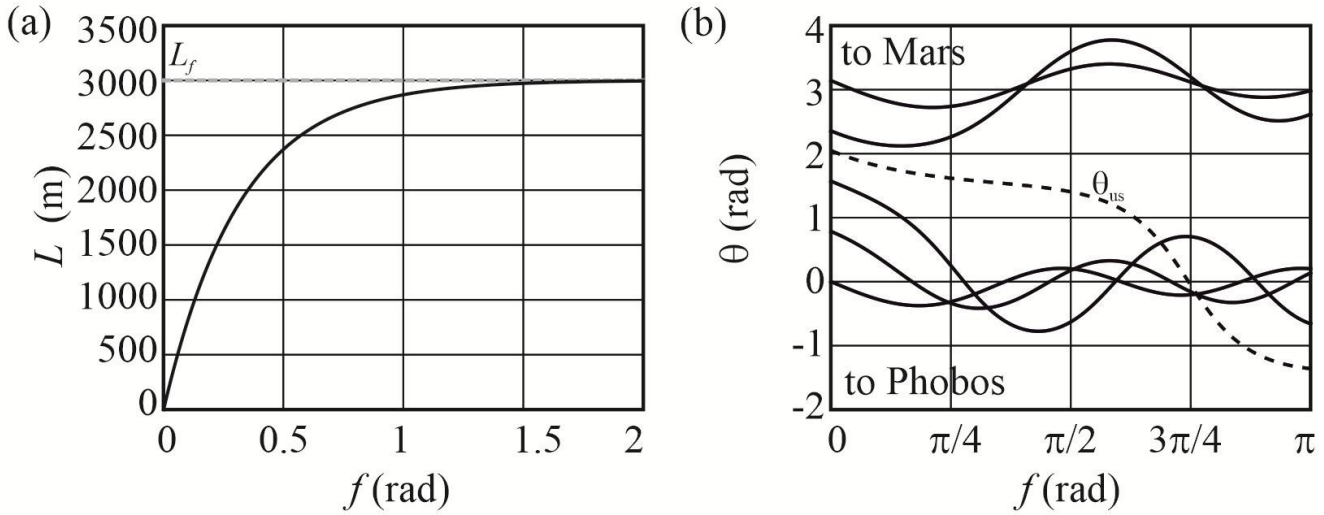

Figure 2.5. The tether deployment length and the oscillation angle of the tether for different initial ejection angles.

Numerical simulation of the mission to explore the surface of Phobos under the L1 libration point

Stage 2

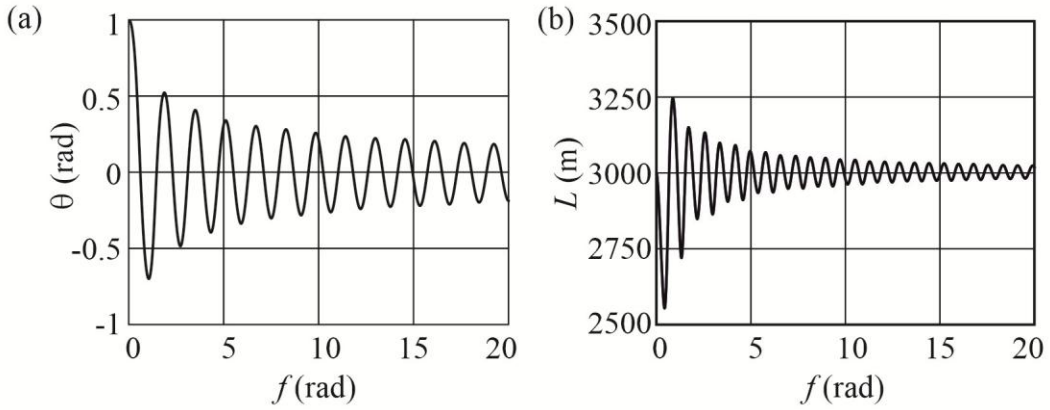

Figure 2.6. Tether angular stabilization towards Phobos.

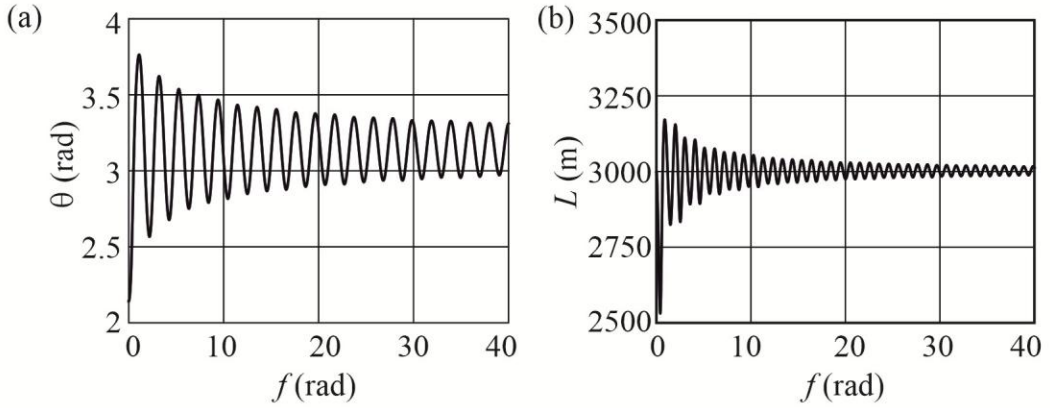

Figure 2.7. Tether angular stabilization towards Mars.

Stage 3

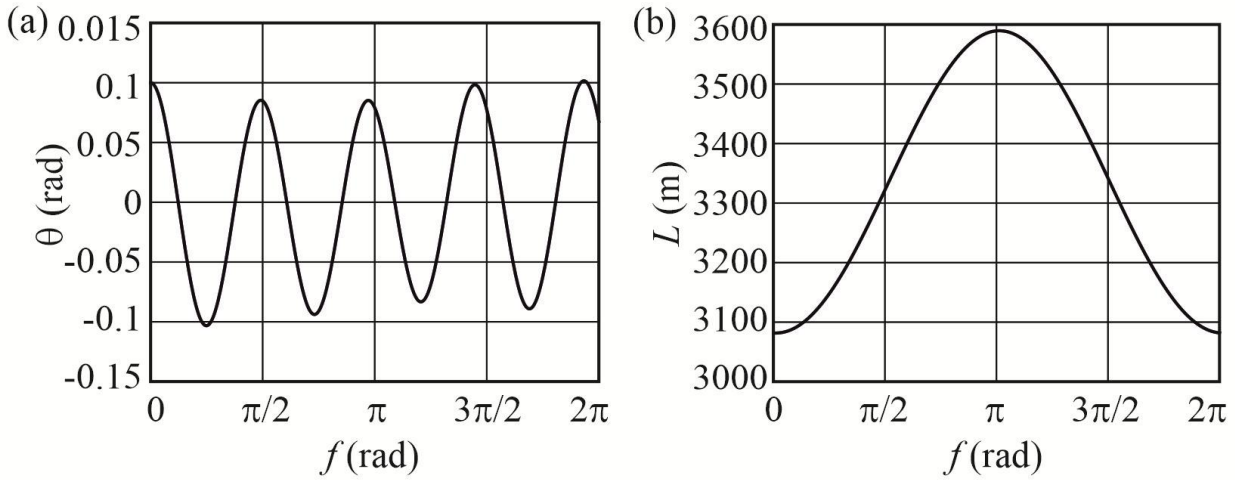

Figure 2.8. The tether oscillation angle and the tether length during the maintaining stage.

2.3. A double pendulum fixed at the L1 libration point

Equations of motion of a double pendulum fixed at the L1 libration point

$$m_1, m_2 \ll M_2 \le M_1 \qquad (2.6) \qquad\qquad n = \frac{df}{dt} = \text{const} \qquad (2.7)$$

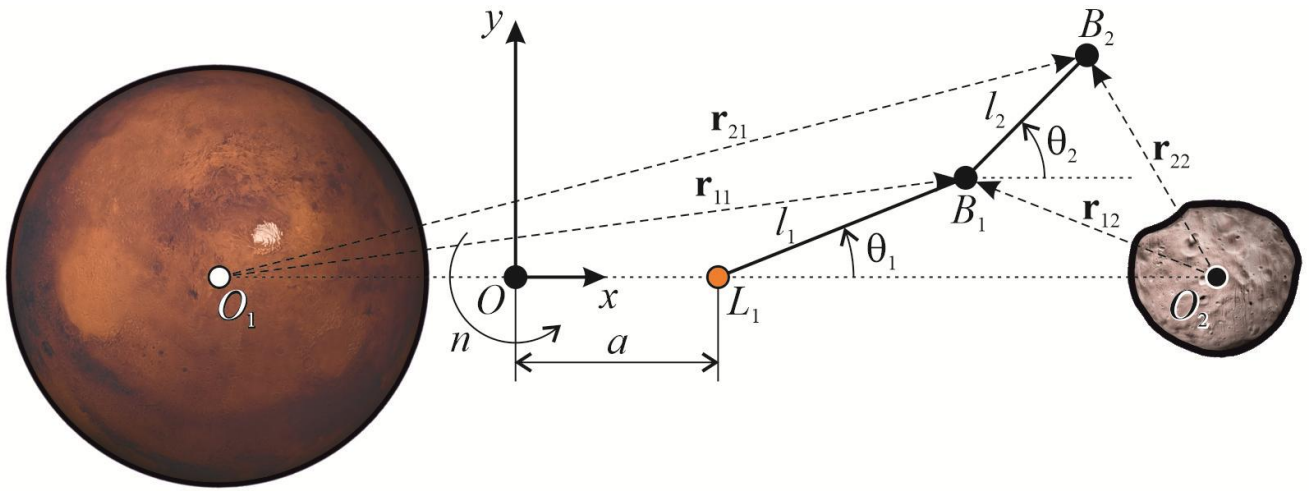

Figure 2.9. The double pendulum fixed at the L1 libration point.

$$\frac{1}{1+\lambda} l(2n\lambda\sigma\dot{\theta}_2 \sin\theta_{12} + \lambda\sigma(n^2 + \dot{\theta}_2^{\,2})\sin\theta_{12} + (1+\sigma)\ddot{\theta}_1 + \lambda\sigma\cos\theta_{12}\ddot{\theta}_2)$$

$$+ an^2(1+\sigma)\sin\theta_1 - GM_1\left(\frac{\sin\theta_1\rho_1}{r_{11}^{3/2}} + \frac{\sigma\left(\frac{\lambda}{1+\lambda} l\sin\theta_{12} + \rho_1\sin\theta_1\right)}{r_{21}^{3/2}}\right)$$

$$- GM_2\left(\frac{\rho_2\sin\theta_1}{r_{12}^{3/2}} + \frac{\sigma\left(\frac{\lambda}{1+\lambda} l\sin\theta_{12} + \rho_2\sin\theta_1\right)}{r_{22}^{3/2}}\right) = 0$$

$$\frac{l}{1+\lambda}(-2n\dot{\theta}_1\sin\theta_{12} - \dot{\theta}_1^{\,2}\sin\theta_{12} + \cos\theta_{12}\ddot{\theta}_1 + \lambda\ddot{\theta}_2)$$

$$+ \sin\theta_2\left(an^2 - G\left(\frac{M_1\rho_1}{r_{21}^{3/2}} + \frac{M_2\rho_2}{r_{22}^{3/2}}\right)\right) + \frac{l}{1+\lambda}\sin\theta_{12}\left(-n^2 + G\left(\frac{M_1}{r_{21}^{3/2}} + \frac{M_2}{r_{22}^{3/2}}\right)\right) = 0$$

(2.8)

Total potential energy and equilibrium positions of a double pendulum

$$T = T^* + \tau \qquad (2.9) \qquad \nu = U + T^* \qquad (2.10)$$

- T is the kinetic energy of the system
- T^* is the energy of concealed motions
- τ is the energy part that depends on velocities $\dot{\theta}_1,\ \dot{\theta}_2$
- ν is the total potential energy

$$T^* = \frac{m}{2(1+\sigma)(1+\lambda)^2} n^2 \Big[\left(a + a\lambda + l\cos\theta_1\right)^2 + l^2 \sin^2\theta_1 + \sigma\left(\left(a + a\lambda + l\cos\theta_1 + l\lambda\cos\theta_2\right)^2 + l^2\left(\sin\theta_1 + \lambda\sin\theta_2\right)^2\right)\Big] \qquad (2.11)$$

$$\tau = \frac{ml}{2(1+\sigma)(1+\lambda)^2} \Big[l\left(1+\sigma\right)\dot{\theta}_1^2 + \lambda\sigma\dot{\theta}_2\left(2n\left(l\lambda + l\cos\theta_{12} + a\left(1+\lambda\right)\cos\theta_2\right) + l\lambda\dot{\theta}_2\right) + \sigma\left(\left(a + a\lambda + l\cos\theta_1 + l\lambda\cos\theta_2\right)^2 + l^2\left(\sin\theta_1 + \lambda\sin\theta_2\right)^2\right)\Big]$$

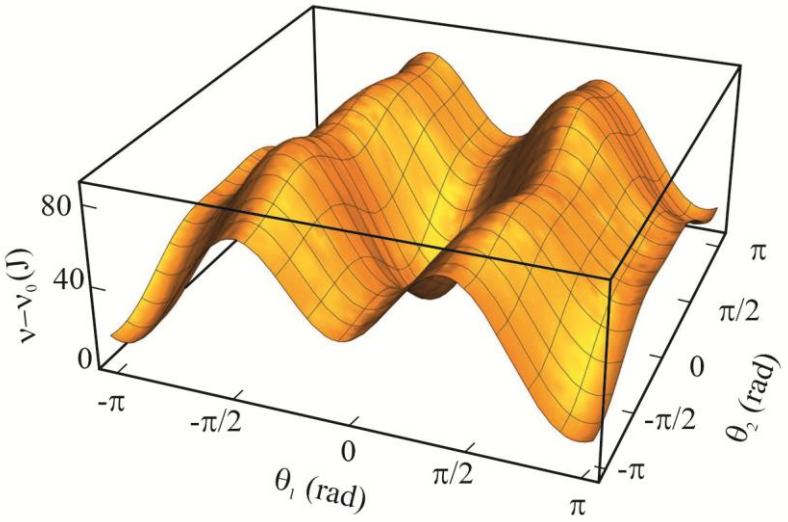

Figure 2.10. The total potential energy surface for an equal pendulum.

Equilibrium positions map of a double pendulum

$$F_1(\theta_1,\theta_2)=n^2\left((1+\sigma)a\sin\theta_1+\frac{\lambda\sigma}{1+\lambda}l\sin\theta_{12}\right)-GM_1\left(\frac{\rho_1}{r_{11}^{3/2}}\sin\theta_1+\frac{\sigma}{r_{21}^{3/2}}\left(\frac{\lambda}{1+\lambda}l\sin\theta_{12}+\rho_1\sin\theta_1\right)\right)-GM_2\left(\frac{\rho_2}{r_{12}^{3/2}}\sin\theta_1+\frac{\sigma}{r_{22}^{3/2}}\left(\frac{\lambda}{1+\lambda}l\sin\theta_{12}+\rho_2\sin\theta_1\right)\right)=0$$

$$F_2(\theta_1,\theta_2)=n^2\left(a\sin\theta_2-\frac{l}{1+\lambda}\sin\theta_{12}\right)+\frac{GM_1}{r_{21}^{3/2}}\left(-\rho_1\sin\theta_2+\frac{l}{1+\lambda}\sin\theta_{12}\right)+\frac{GM_2}{r_{22}^{3/2}}\left(-\rho_2\sin\theta_2+\frac{l}{1+\lambda}\sin\theta_{12}\right)=0 \qquad (2.12)$$

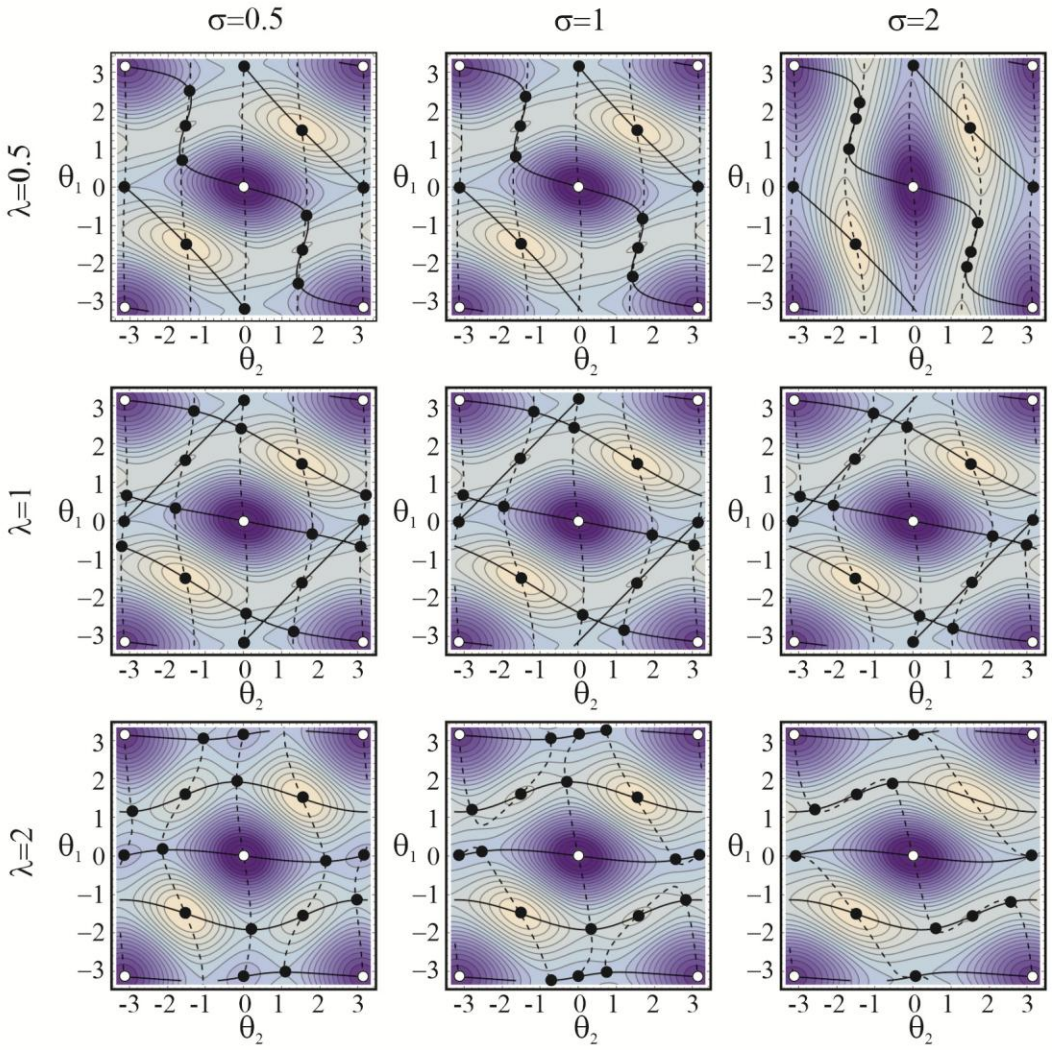

Figure 2.11. The total potential energy surface for an equal pendulum.

Equilibrium positions map of a double pendulum

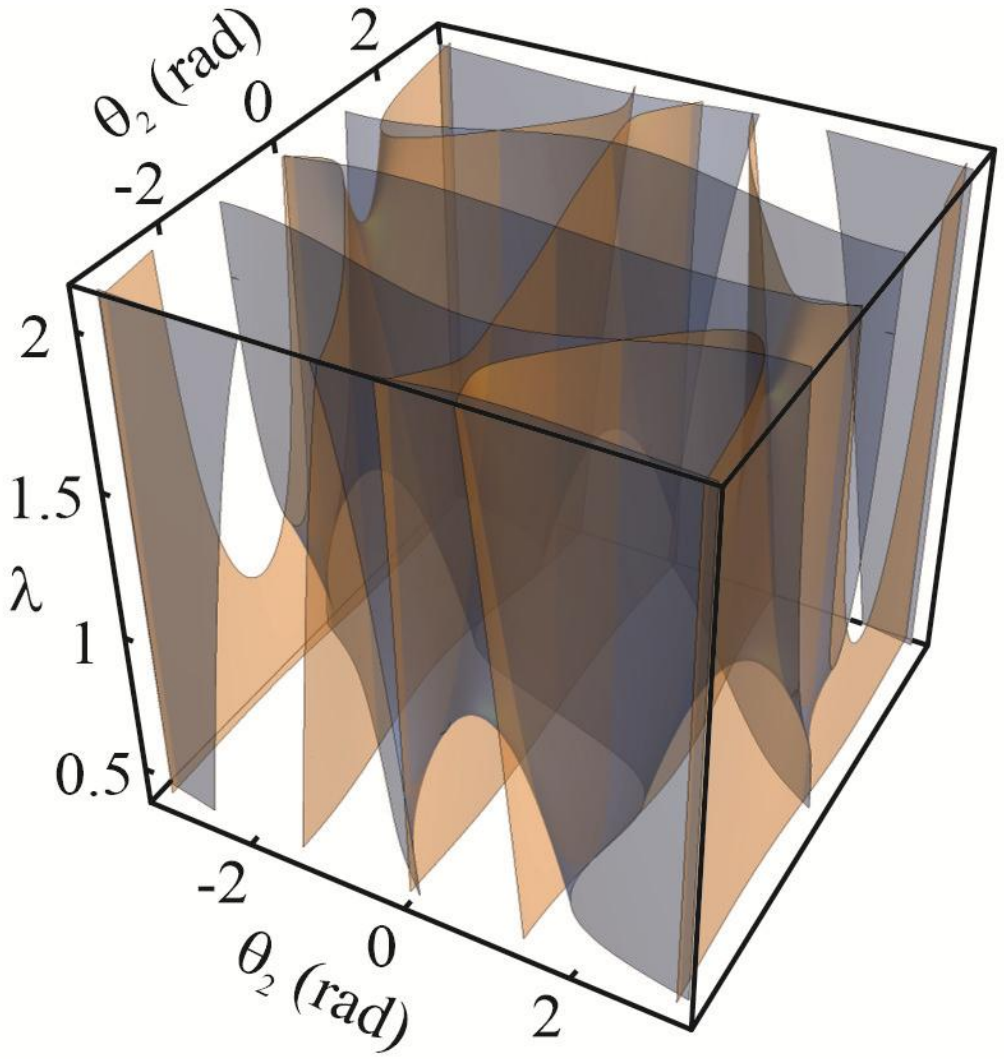

Figure 2.12. The influence of the parameter λ on the equilibrium lines (2.12).

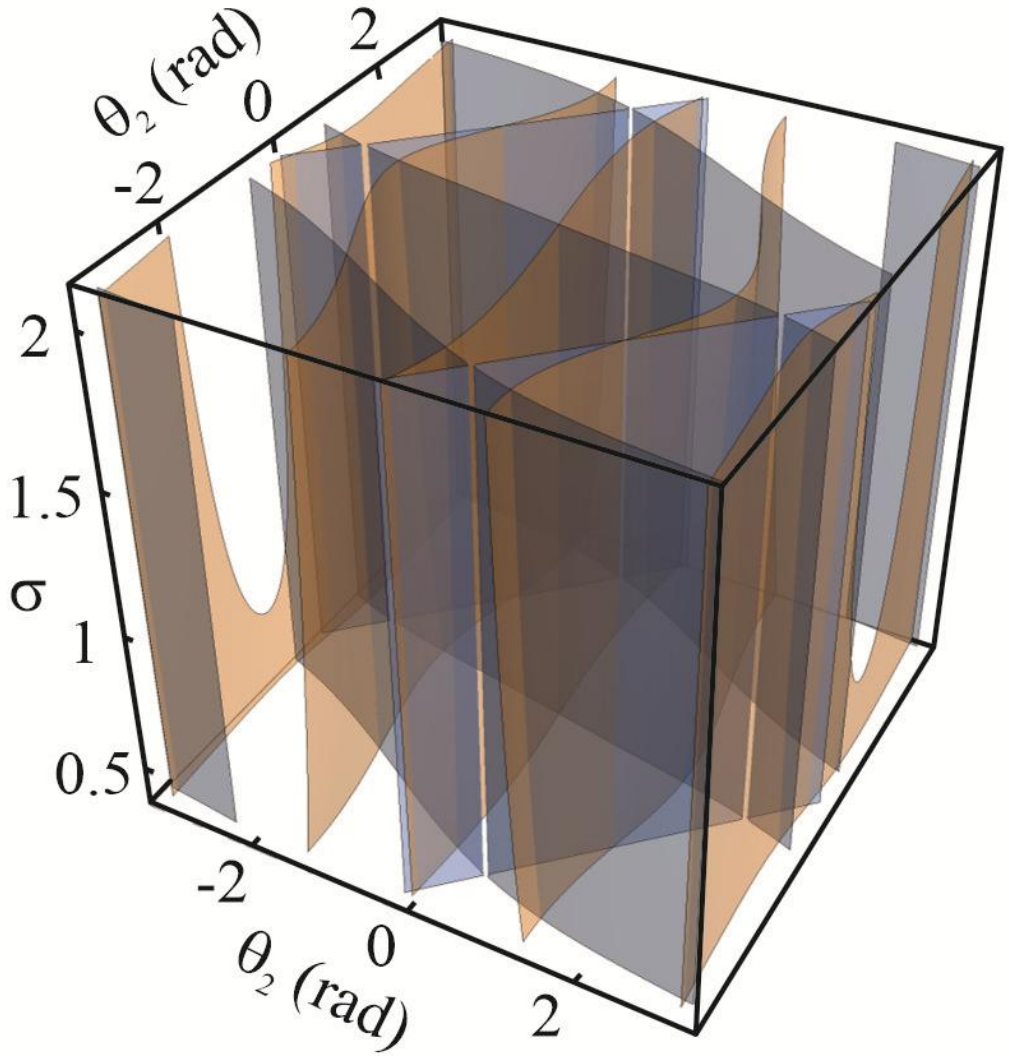

Figure 2.13. The influence of the parameter σ on the equilibrium lines (2.12).

Small motion around lower equilibrium configuration

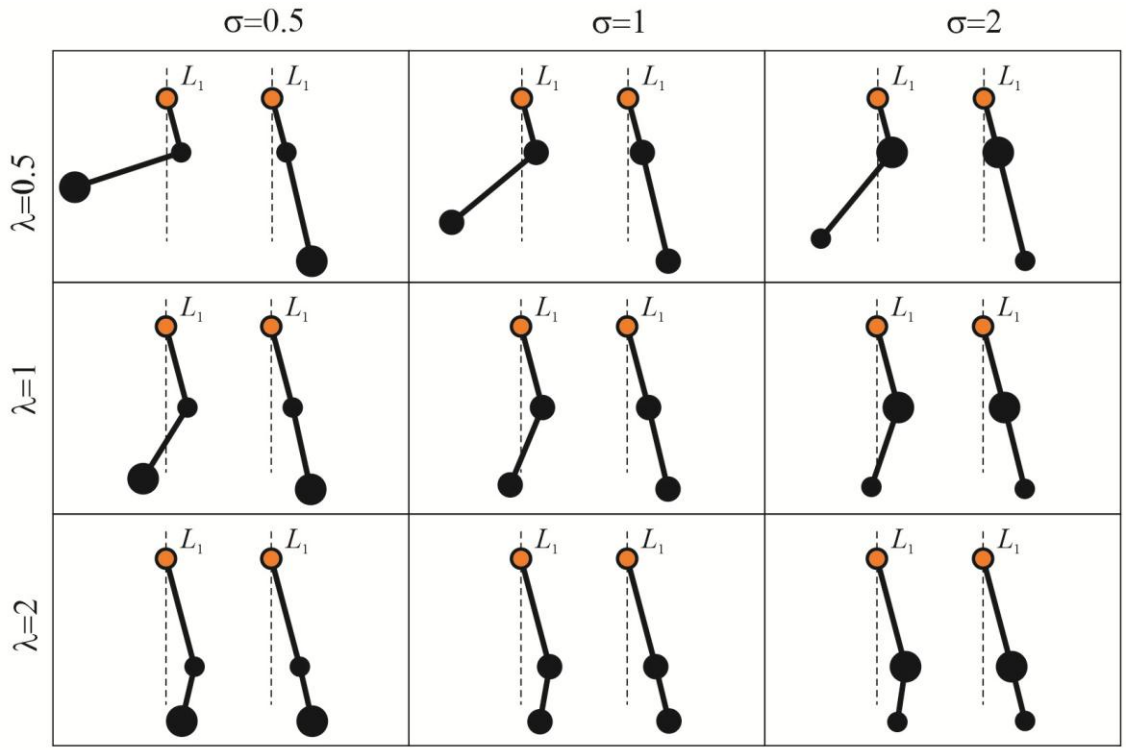

Figure 2.14. The mode ratios for the double pendulum swinging toward Phobos.

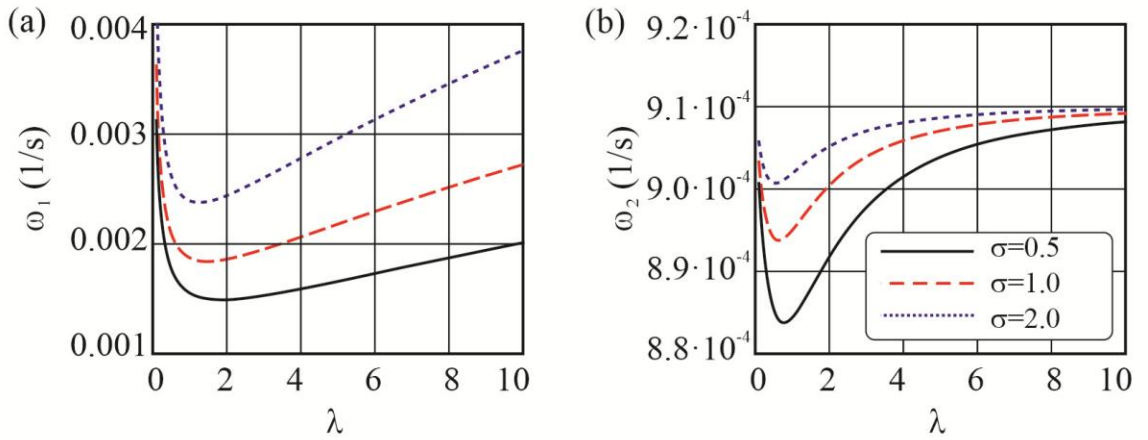

Figure 2.15. Dependence of the natural frequencies ω_1, ω_2 on the length ratio for various mass ratios $\sigma = 0.5, 1, 2$.

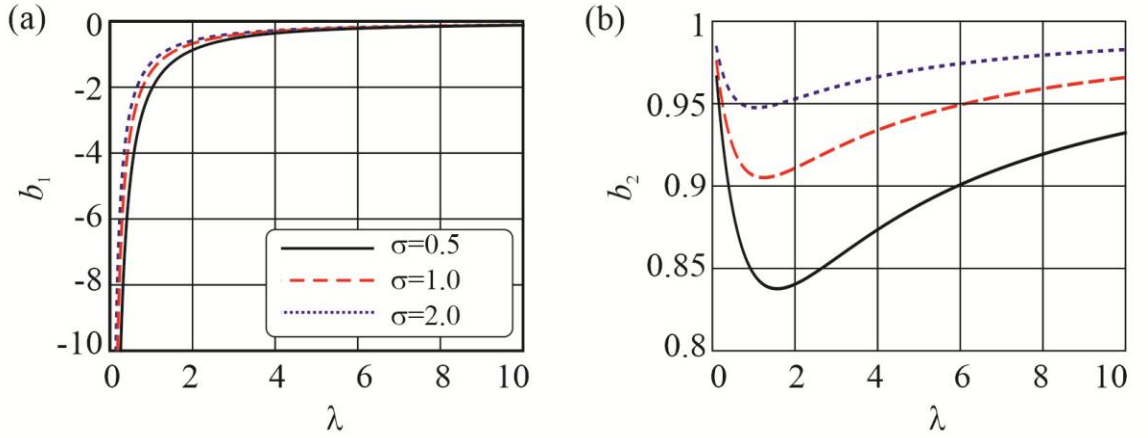

Figure 2.16. Dependence of the mode ratios b_1, b_2 on the length ratio for various mass ratios $\sigma = 0.5, 1, 2$.

Small motion around upper equilibrium configuration

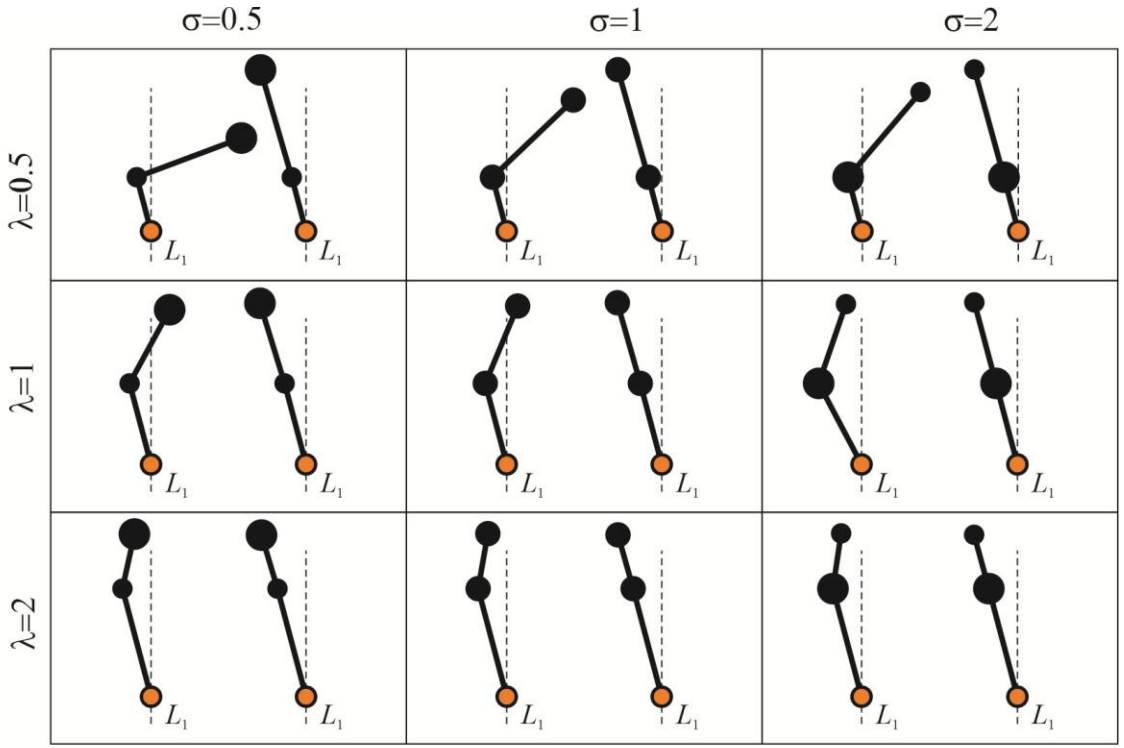

Figure 2.17. The mode ratios for the double pendulum swinging toward Mars.

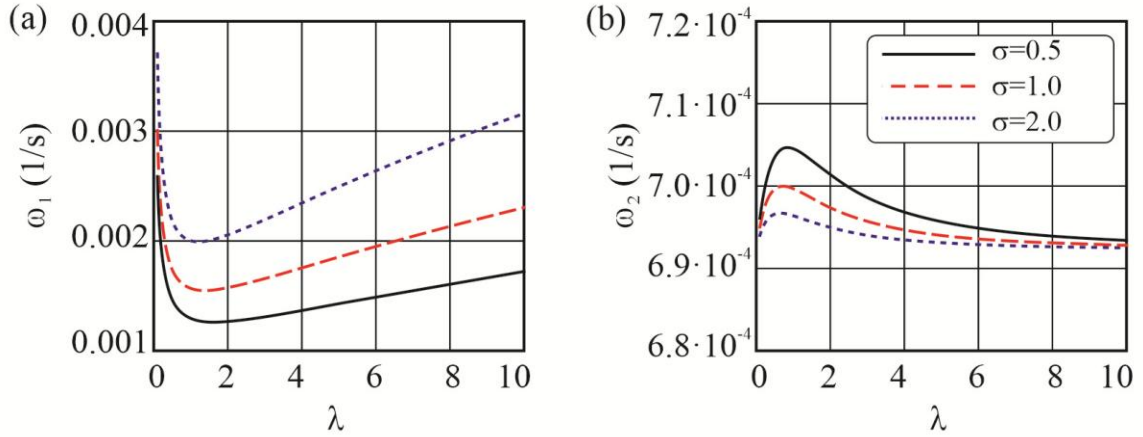

Figure 2.18. Dependence of the natural frequencies ω_1, ω_2 on the length ratio for various mass ratios $\sigma = 0.5, 1, 2$.

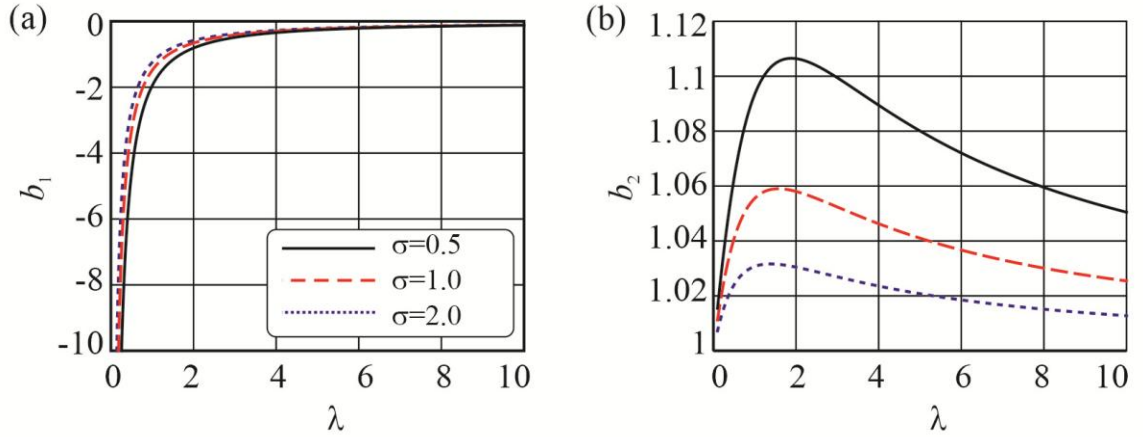

Figure 2.19. Dependence of the mode ratios b_1, b_2 on the length ratio for various mass ratios $\sigma = 0.5, 1, 2$.

2.4. Partial space elevator fixed at the L1 libration point

Tethers' tension forces during acceleration, movement at constant velocity and braking of a climber

$$m_1, m_2 \ll M_2 \le M_1 \qquad (2.13) \qquad l_0 = l_1 + l_2 = \text{const} \qquad l_1 = l_0 + Vt \qquad l_2 = -Vt \qquad (2.14)$$

$$\ddot{\theta}_1 = \frac{1}{l_1}\left[G\left(\frac{M_1\rho_1 \sin\theta_1}{r_{11}^{\ 3}} + \frac{M_2\rho_2 \sin\theta_1}{r_{12}^{\ 3}} \right) - an^2 \sin\theta_1 - 2V\left(n + \dot{\theta}_1\right) - \frac{T_2}{m_1}\sin\theta_{12} \right]$$

$$\ddot{\theta}_2 = \frac{1}{l_2}\left[G\left(\frac{\left(r_{12}^3 - r_{22}^3\right)M_2\left(\rho_2 \sin\theta_2 - \sin\theta_{12} l_1\right)}{r_{12}^3 r_{22}^3} + \frac{\left(r_{11}^3 - r_{21}^3\right)M_1\left(\rho_1 \sin\theta_2 - \sin\theta_{12} l_1\right)}{r_{11}^3 r_{21}^3} \right) \right. \qquad (2.15)$$

$$\left. + 2V\left(n + \dot{\theta}_2\right) + \frac{T_1}{m_1}\sin\theta_{12} \right]$$

$$T_1 = \frac{m_1 m_2}{m_1 + m_2 \sin\theta_{12}^{\ 2}}\left[GM_1\left(-\frac{\left(l_1 + \rho_1\cos\theta_1\right)}{\mu r_{11}^3} - \cos\theta_{12}\left(-\frac{\rho_1\cos\theta_2 + l_1\cos\theta_{12}}{r_{11}^3} \right.\right.\right.$$

$$\left.\left.\left. + \frac{\rho_1\cos\theta_2 + l_1\cos\theta_{12} + l_2}{r_{21}^3} \right) \right) + GM_2\left(-\frac{\left(l_1 + \rho_2\cos\theta_1\right)}{\mu r_{12}^3} - \cos\theta_{12}\left(-\frac{\rho_2\cos\theta_2 + l_1\cos\theta_{12}}{r_{12}^3} \right.\right.$$

$$\left.\left. + \frac{\rho_2\cos\theta_2 + l_1\cos\theta_{12} + l_2}{r_{22}^3} \right) \right) + \frac{1}{\mu}\left(an^2\cos\theta_1 + l_1\left(n + \dot{\theta}_1\right)^2 \right) + l_2\cos\theta_{12}\left(n + \dot{\theta}_2\right)^2 \Big] \qquad (2.16)$$

$$T_2 = \frac{m_1 m_2}{m_1 + m_2 \sin\theta_{12}^{\ 2}}\left[GM_1\left(\frac{\rho_1 \sin\theta_1 \sin\theta_{12}}{r_{11}^3} - \frac{\rho_1\cos\theta_2 + l_1\cos\theta_{12} + l_2}{r_{21}^3} \right) \right.$$

$$\left. + GM_2\left(\frac{\rho_2 \sin\theta_1 \sin\theta_{12}}{r_{12}^3} - \frac{\rho_2\cos\theta_2 + l_1\cos\theta_{12} + l_2}{r_{22}^3} \right) + \frac{an^2}{2}\left(\cos\left(2\theta_1 - \theta_2\right) + \cos\theta_2\right) + l_1\left(n + \dot{\theta}_1\right)^2\cos\theta_{12} + l_2\left(n + \dot{\theta}_2\right)^2 \right]$$

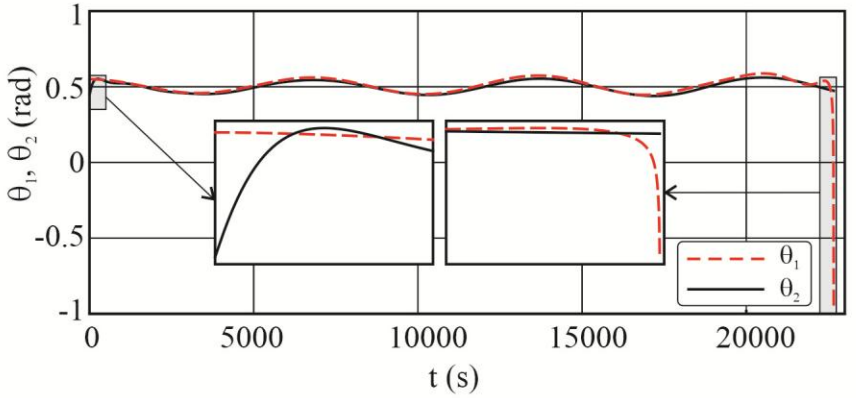

Figure 2.20. The deflection angles of the partial space elevator tethers θ_1, θ_2

Tethers' tension forces during acceleration, movement at constant velocity and braking of a climber

The acceleration phase:

$$l_1 = l_0 + \frac{4Vt_V}{\pi}\sin\left[\frac{\pi(t-t_0)}{4t_V}\right]^2 \qquad l_2 = l_0 - l_1$$

$$V_1 = \frac{dl_1}{dt} = V\sin\left[\frac{\pi(t-t_0)}{2t_V}\right] \qquad V_2 = -V_1 \qquad (2.17)$$

$$W_1 = \frac{dV_1}{dt} = \frac{\pi V}{2t_V}\cos\left[\frac{\pi(t-t_0)}{2t_V}\right] \qquad W_2 = -W_1$$

The main phase:

$$l_1 = l_0 + V\left[t - t_V\left(1 - \frac{2}{\pi}\right) - t_0\right] \qquad l_2 = l_0 - l_1$$

$$V_1 = \frac{dl_1}{dt} = V \qquad V_2 = -V_1 \qquad (2.18)$$

$$W_1 = \frac{dV_1}{dt} = 0 \qquad W_2 = 0$$

The deceleration phase:

$$l_1 = l_0 + (t_f - t_0 - 2t_V)V + \frac{4Vt_V}{\pi}\cos\left[\frac{\pi(t_f - t)}{4t_V}\right]^2 \qquad l_2 = l_0 - l_1$$

$$V_1 = \frac{dl_1}{dt} = V\sin\left[\frac{\pi(t_f - t)}{2t_V}\right] \qquad V_2 = -V_1 \qquad (2.19)$$

$$W_1 = \frac{dV_1}{dt} = -\frac{\pi V}{2t_V}\cos\left[\frac{\pi(t_f - t)}{2t_V}\right] \qquad W_2 = 0$$

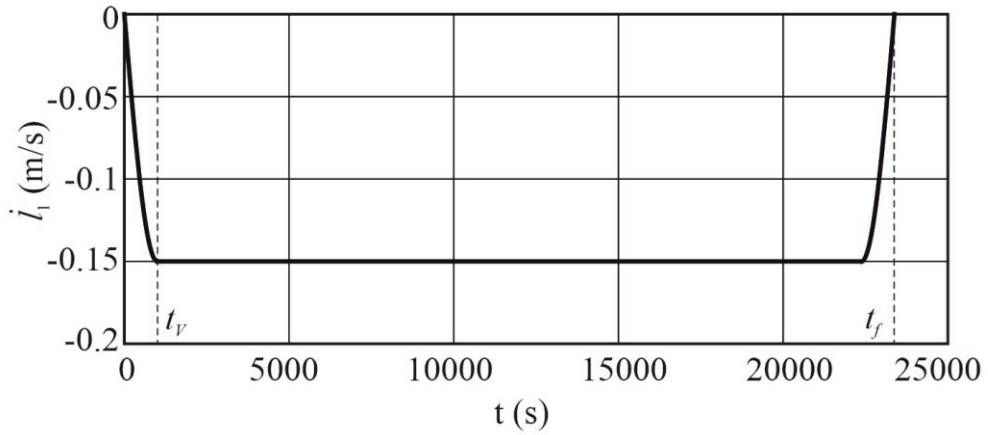

Figure 2.21. The climber's velocity profile

Climbing from the surface of Phobos to the L1 libration point and return using a partial space elevator deployed towards Phobos

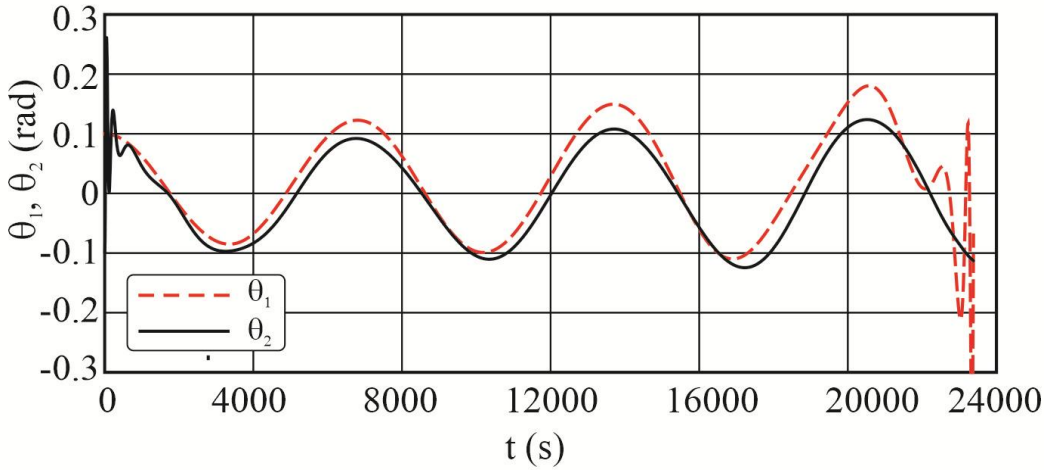

Figure 2.22. Changing the deflection angles of the partial space elevator tethers during the climber lifting from the surface of Phobos to the orbiter ($\sigma = 1$).

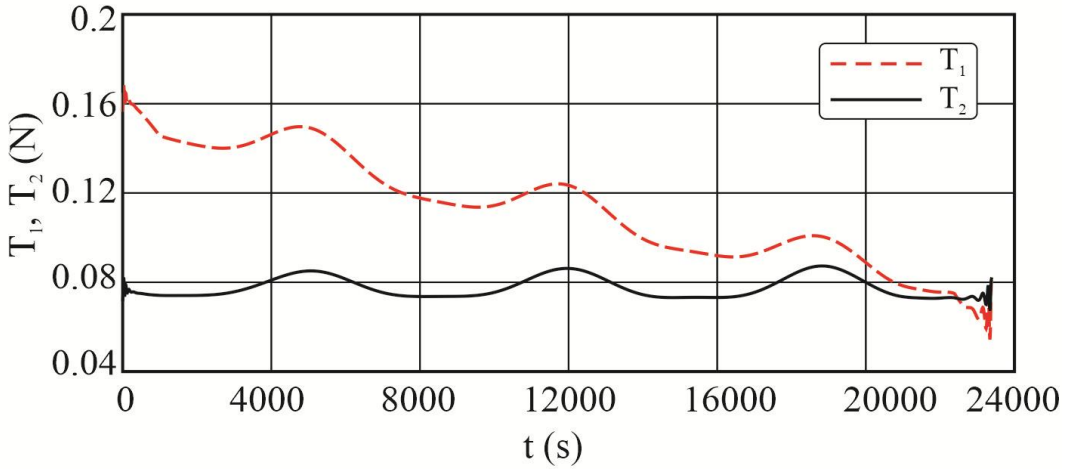

Figure 2.23. The dependences of the tension forces on time during the climber lifting from the surface of Phobos to the orbiter ($\sigma = 1$).

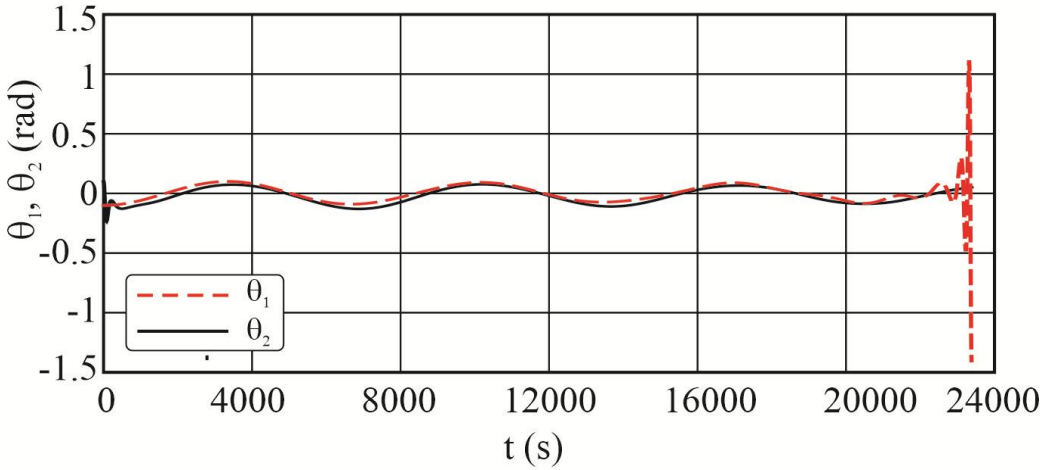

Figure 2.24. Changing the deflection angles of the partial space elevator tethers during the climber lowering from the orbiter to the surface of Phobos.

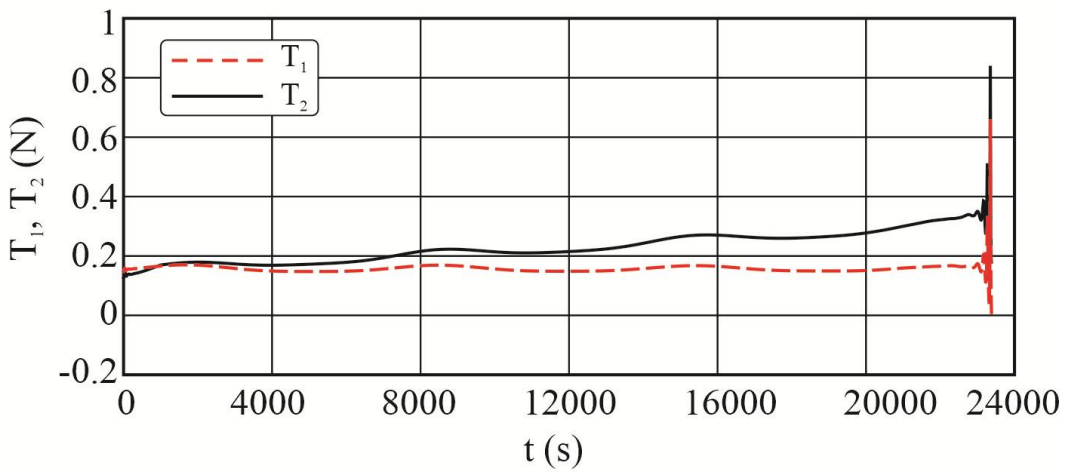

Figure 2.25. The dependences of the tension forces on time during the climber lowering from the orbiter to the surface of Phobos.

Climbing from the surface of Phobos to the L1 libration point and return using a partial space elevator deployed towards Phobos

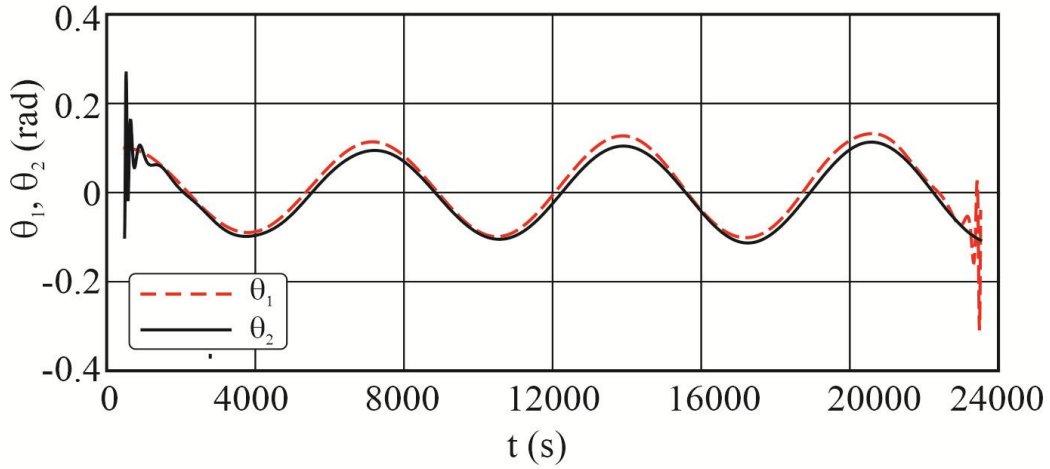

Figure 2.26. Changing the deflection angles of the partial space elevator tethers during the climber lifting from the surface of Phobos to the orbiter ($\sigma = 2$).

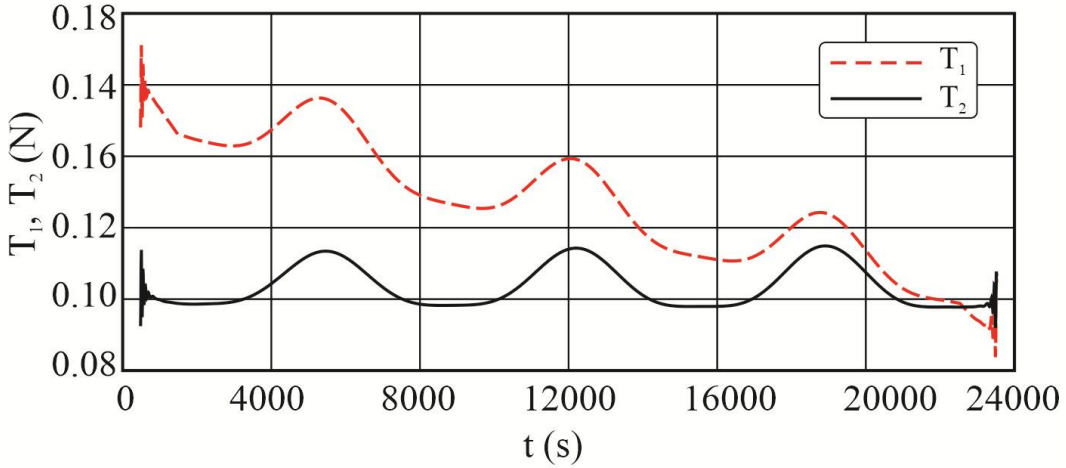

Figure 2.27. The dependences of the tension forces on time during the climber lifting from the surface of Phobos to the orbiter ($\sigma = 2$).

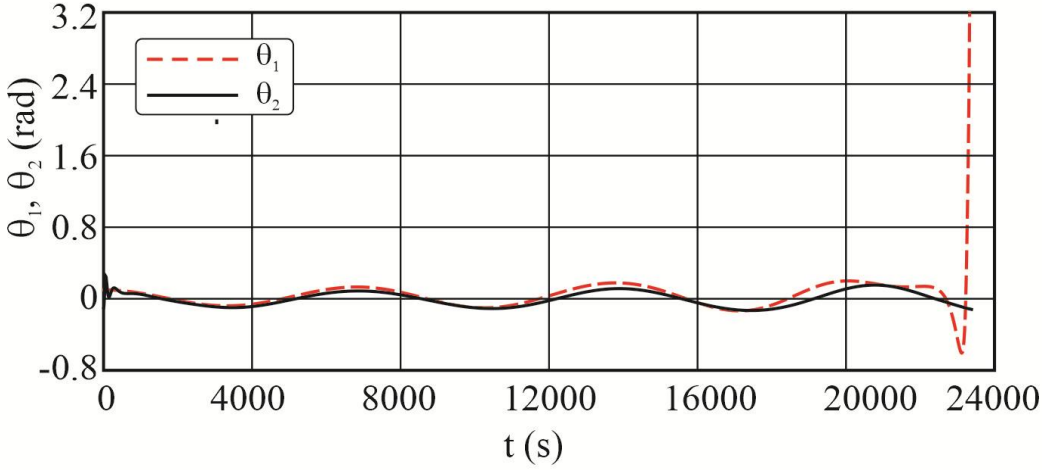

Figure 2.28. Changing the deflection angles of the partial space elevator tethers during the climber lifting from the surface of Phobos to the orbiter ($\sigma = 0.5$).

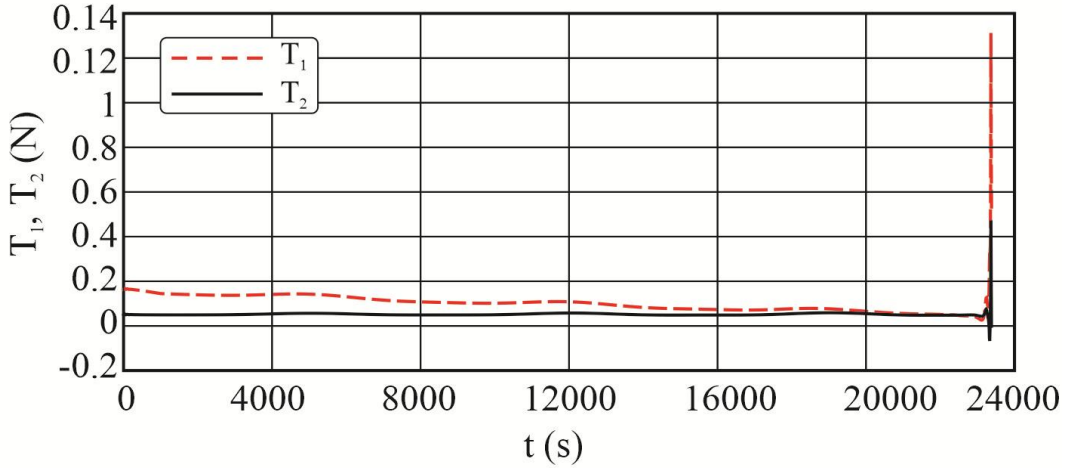

Figure 2.29. The dependences of the tension forces on time during the climber lifting from the surface of Phobos to the orbiter ($\sigma = 0.5$).

Climbing to the L1 libration point and return to the elevator's end using a partial space elevator deployed towards Mars

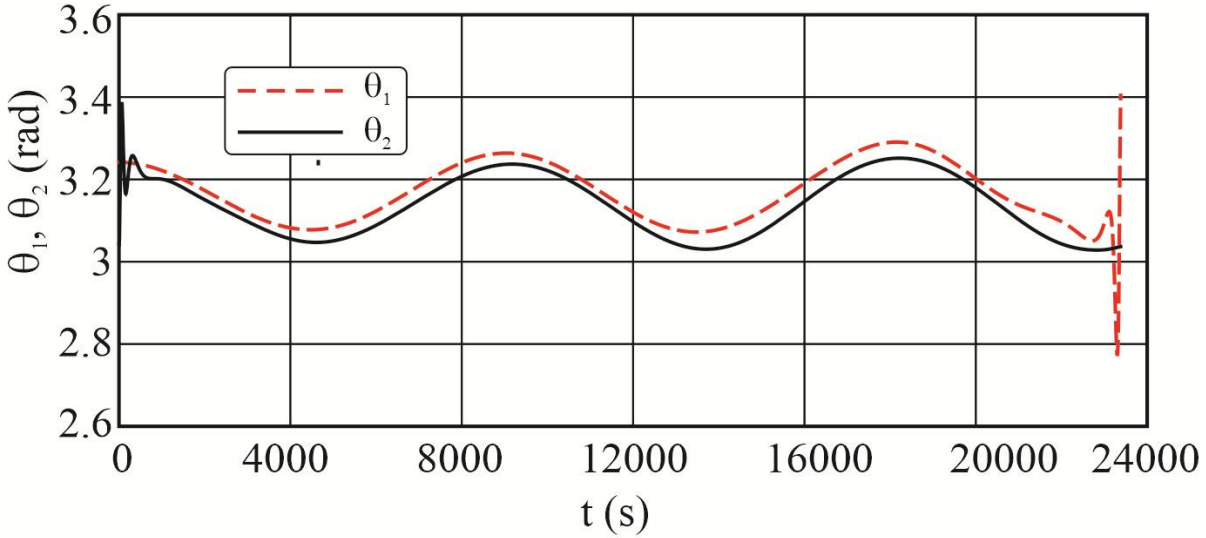

Figure 2.30. Changing the deflection angles of the partial space elevator tethers during the climber motion towards the L1 libration point.

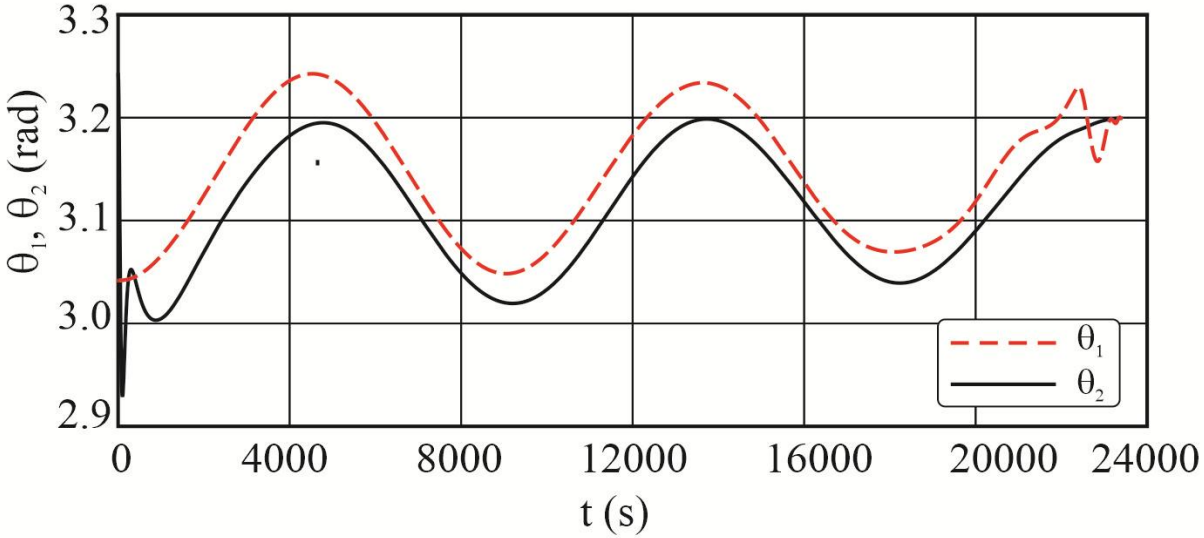

Figure 2.31. Changing the deflection angles of the partial space elevator tethers during the climber motion towards Mars.

Turning the partial space elevator from Phobos towards Mars and back

$$l_1 = l_0(+c\dot{\theta}_1 \sin\theta_1) \qquad (2.20) \qquad l_1\ddot{\theta}_1 = G\left[\frac{M_1\rho_1 \sin\theta_1}{r_{11}^{\ 3}} + \frac{M_2\rho_2 \sin\theta_1}{r_{12}^{\ 3}}\right] - an^2 \sin\theta_1 - 2\dot{l}_1\left(n + \dot{\theta}_1\right) \qquad (2.21)$$

$$\theta_{10} = -0.2\,\text{rad} \qquad \dot{\theta}_{10} = 0$$

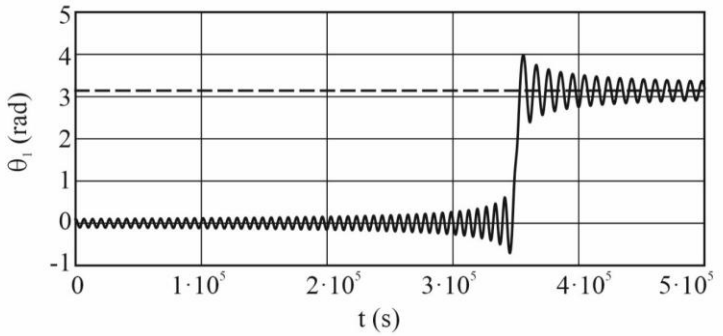

Figure 2.32. Dependence of the tether deflection angle θ_1 on time when using control.

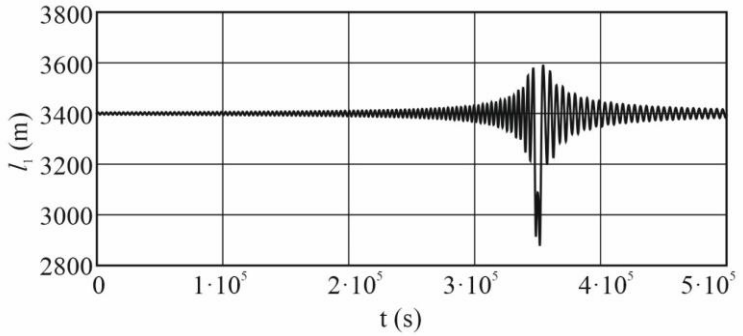

Figure 2.33. Dependence of the tether length l_1 on time when using control.

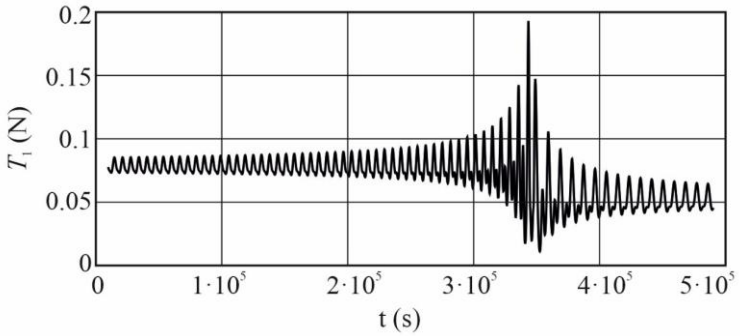

Figure 2.34. Dependence of the tether tension force on time when using control.

$$\theta_{10} = \pi + 0.2\,\text{rad} \qquad \dot{\theta}_{10} = 0$$

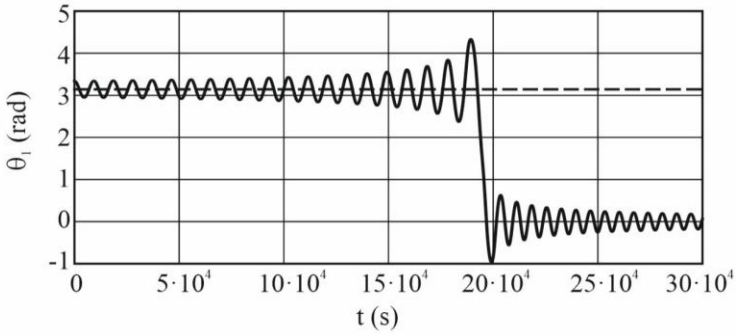

Figure 2.35. Dependence of the tether deflection angle θ_1 on time when using control.

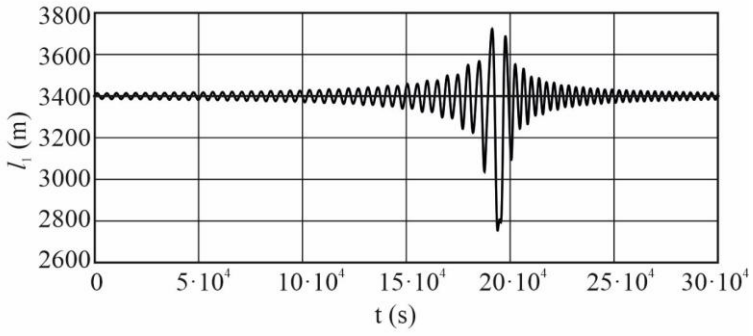

Figure 2.36. Dependence of the tether length l_1 on time when using control.

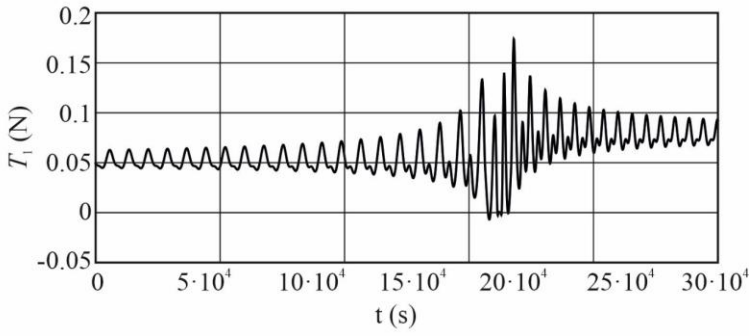

Figure 2.37. Dependence of the tether tension force on time when using control.

2.5. Space tether system at quasi-satellite orbit

Equations of motion of a space tether system at quasi-satellite orbit

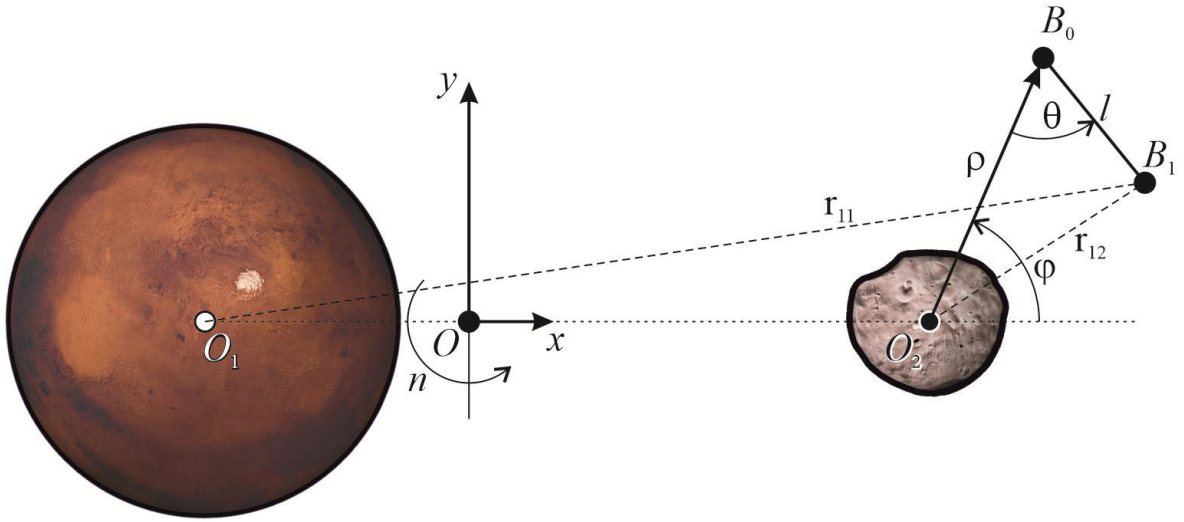

Figure 2.38. Space tether system in the restricted three-body problem.

$$\ddot{\rho} = -\frac{GM_1(p\cos\varphi+\rho)}{r_{11}^3} - \frac{Gm_2}{\rho^2} + n^2 x_2\cos\varphi + \rho(n+\dot{\varphi})^2$$

$$\rho\ddot{\varphi} = -n^2 x_2\sin\varphi + \frac{GM_1 p\sin\varphi}{r_{11}^3} - 2\dot{\rho}\left(n+\dot{\varphi}\right) \qquad (2.22)$$

$$\ddot{l} - \rho\ddot{\varphi}\sin\theta - \ddot{\rho}\cos\theta = GM_1\frac{\rho\cos\theta - l + p\cos(\theta+\varphi)}{r_{11}^3} + GM_2\frac{\rho\cos\theta - l}{r_{12}^3}$$
$$+ l(\dot{\theta}+\dot{\varphi})(2\omega+\dot{\theta}+\dot{\varphi}) + n^2(l-\rho\cos\theta - p(1-\mu)\cos(\theta+\varphi))$$
$$+ 2\dot{\rho}(n+\dot{\varphi})\sin\theta - \rho\dot{\varphi}(2n+\dot{\varphi})\cos\theta - \frac{1}{m_1}T$$

$$l\ddot{\theta} + (l-\rho\cos\theta)\ddot{\varphi} + \ddot{\rho}\sin\theta = -\frac{GM_1(\rho\sin\theta + p\sin(\theta+\varphi))}{r_{11}^3} - \frac{GM_2\rho\sin\theta}{r_{12}^3} -$$
$$-(n^2(\rho\sin\theta + (p(1-\mu)+l\cos(\theta+\varphi))\sin(\theta+\varphi)) + 2(n+\dot{\varphi})\dot{\rho}\cos\theta \qquad (2.23)$$
$$+ \rho(2n+\dot{\varphi})\dot{\varphi}\sin\theta) + \frac{1}{2}l\,n^2\sin 2(\theta+\varphi) - 2\dot{l}(n+\dot{\theta}+\dot{\varphi})$$

Deployment of tether system from the orbiter in low QSO to study the Phobos's surface

$$T = \begin{cases} k_d(d - R - h) + k_V \dfrac{d(d)}{dt}, & if: d - R - h < 0 \\ 0, & if: d - R - h \geq 0 \end{cases} \qquad (2.24)$$

- It is assumed that Phobos has the shape of an ellipse.
- k_d, k_V are the control law coefficients.
- R is the distance from the observation point on the Phobos's surface to the Phobos center.
- d is the distance between the tethered end body and the center of Phobos.

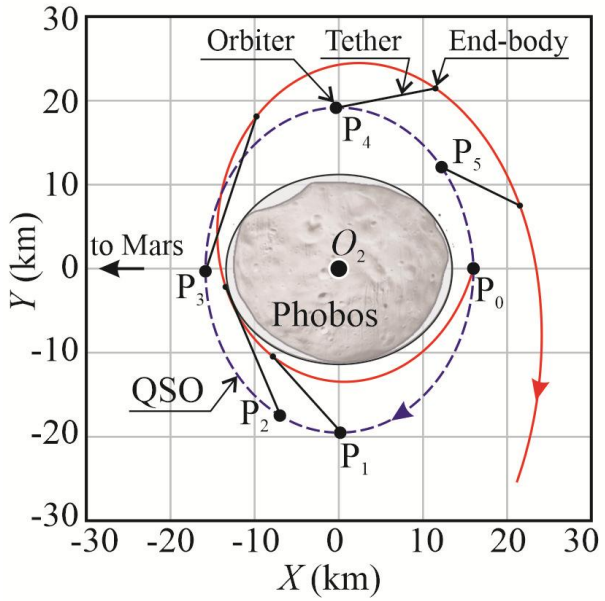

Figure 2.39.
Deployment of the space tether system from the rightmost point.

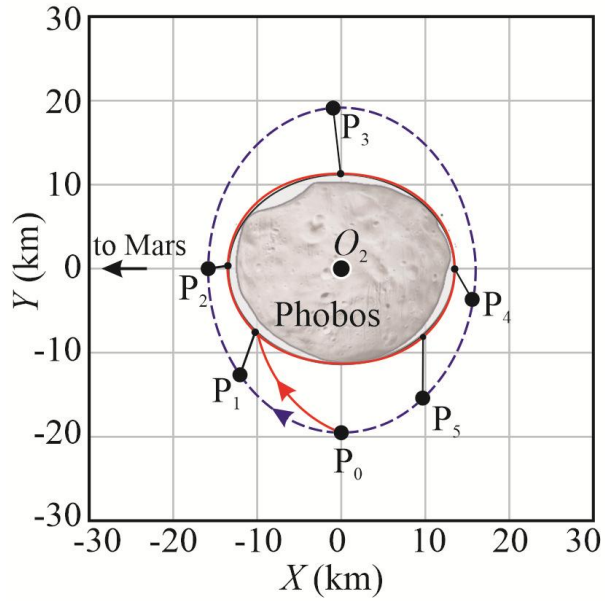

Figure 2.40.
Deployment of the space tether system from the lowest point.

Deployment of tether system from the orbiter in low QSO to study the Phobos's surface

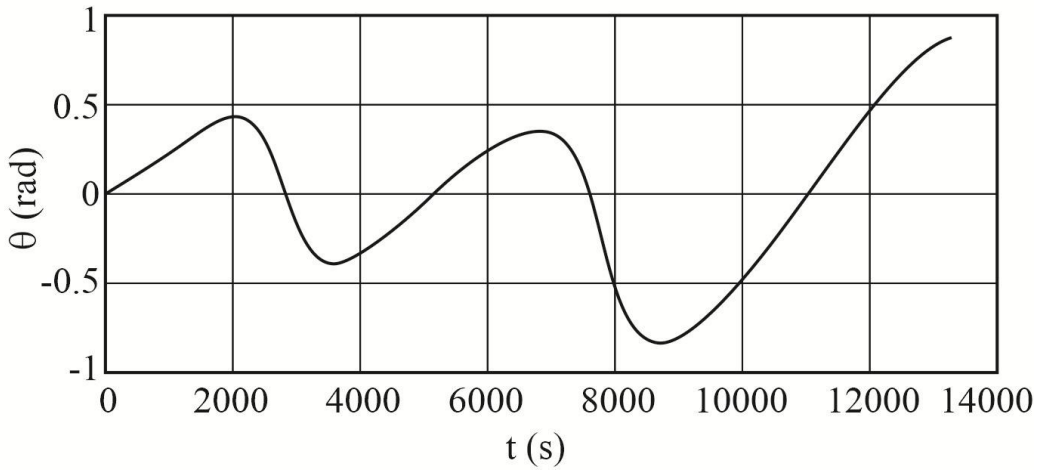

Figure 2.41. Time history of the tether deflection angle.

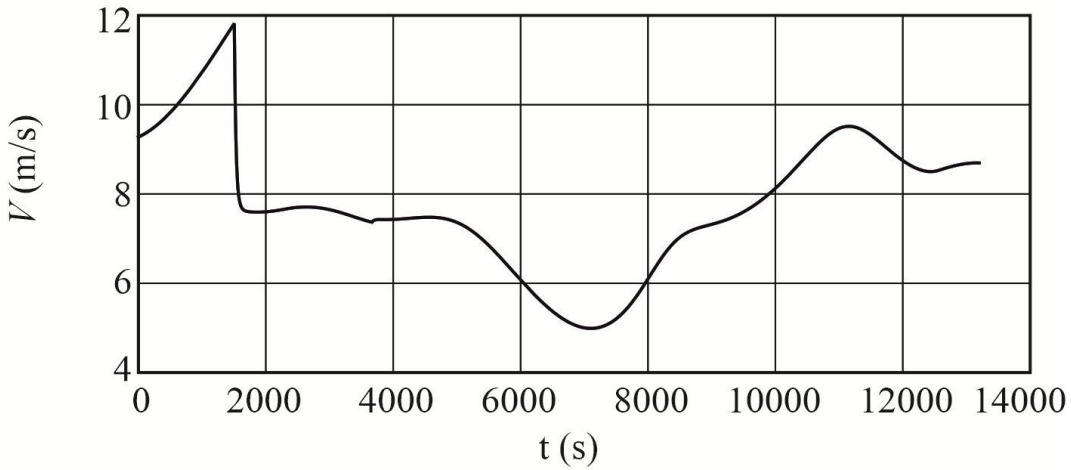

Figure 2.43. Time history of the flight velocity of the tethered end-body.

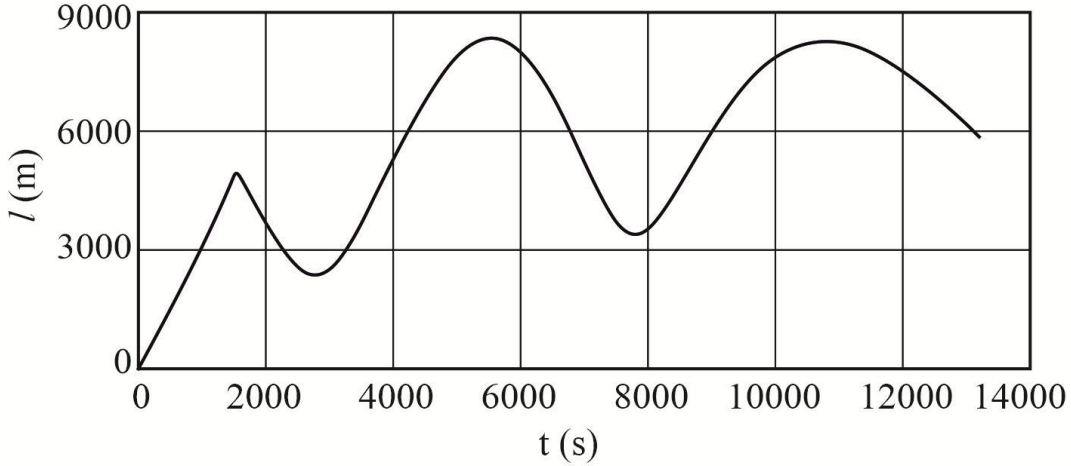

Figure 2.42. Time history of the tether length.

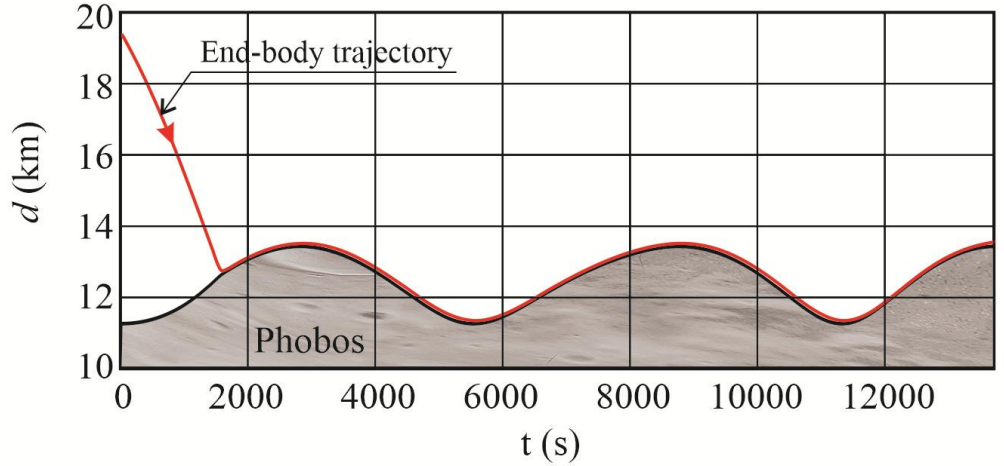

Figure 2.44. The flight trajectory of the tethered end-body over the Phobos’s surface.

Retrieval of the tether system into orbiter in low QSO

$$\dot{l} = -V_r = \text{const} \qquad l = l_{r0} - V_r t \qquad (2.25)$$

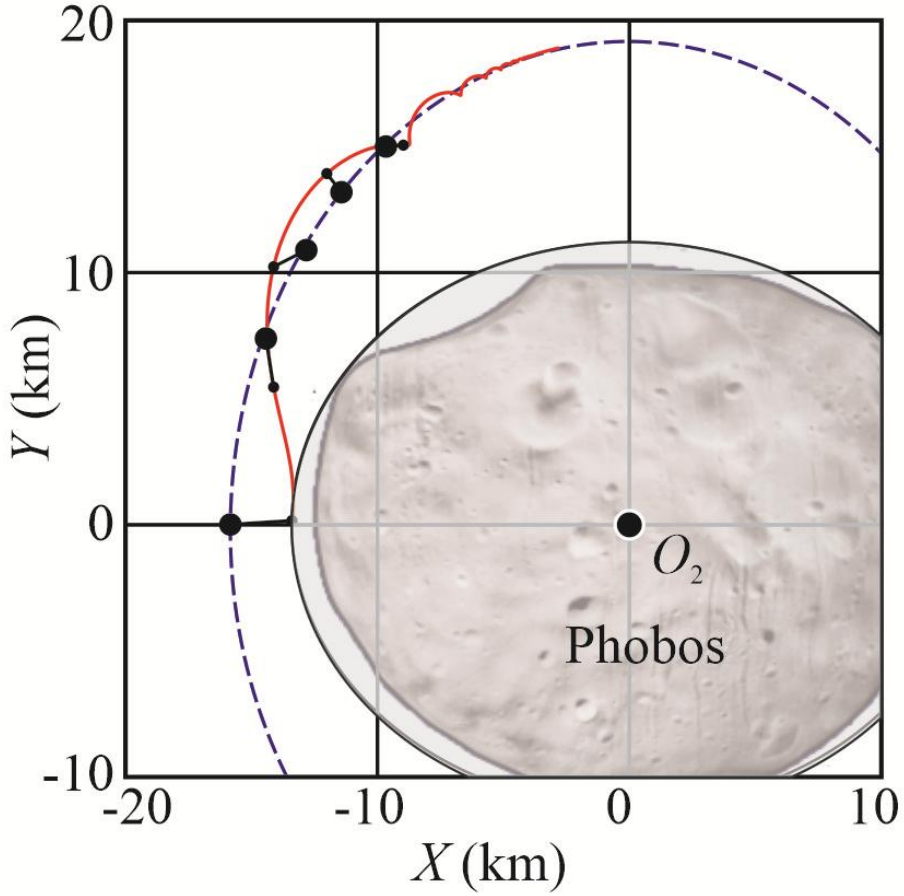

Figure 2.45. The tether retrieval at a constant velocity.

$$u = k_\theta(\theta - \theta_d) + k_\omega \dot{\theta} \qquad (2.26)$$

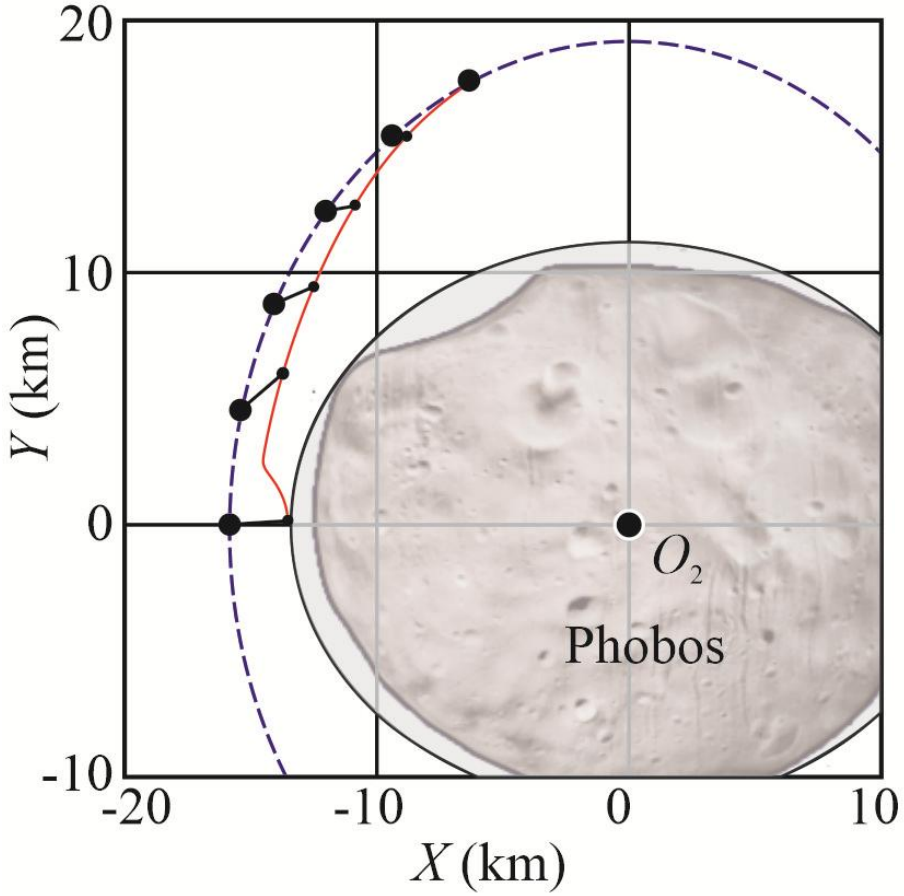

Figure 2.46. The tether retrieval at a constant velocity with an additional control thruster.

Chapter 3

Moon-Anchored Space Elevators

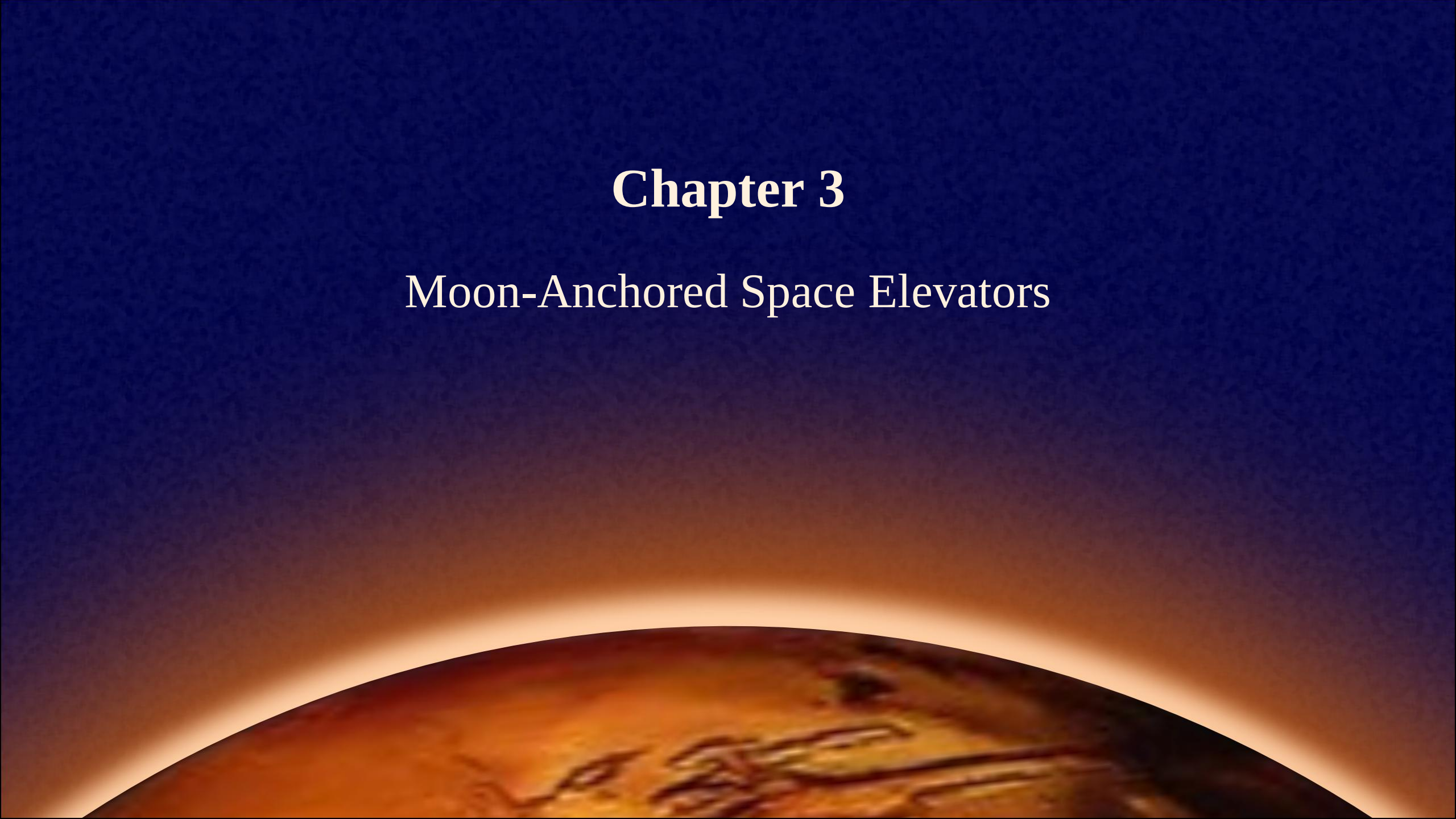

Space elevator concept

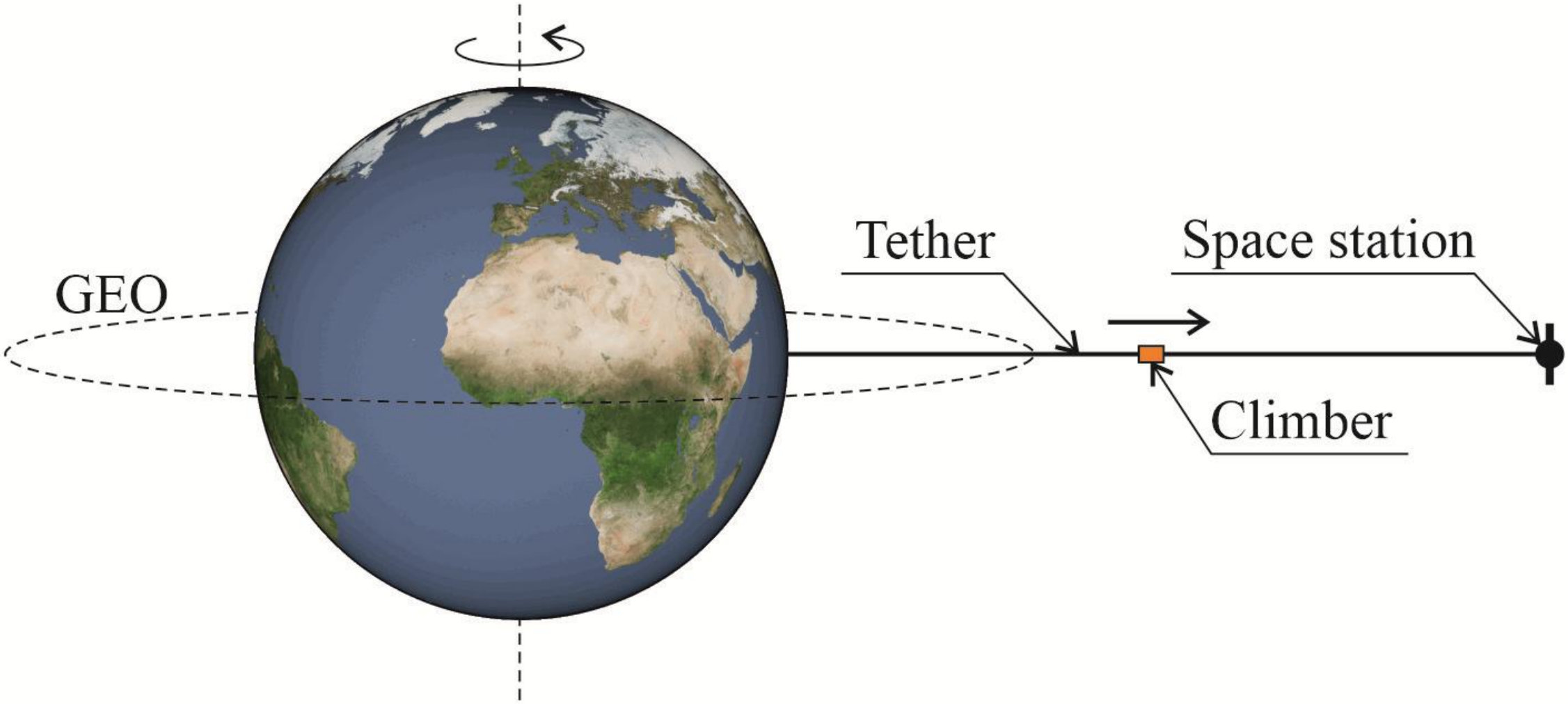

Figure 3.1. Space elevator scheme.

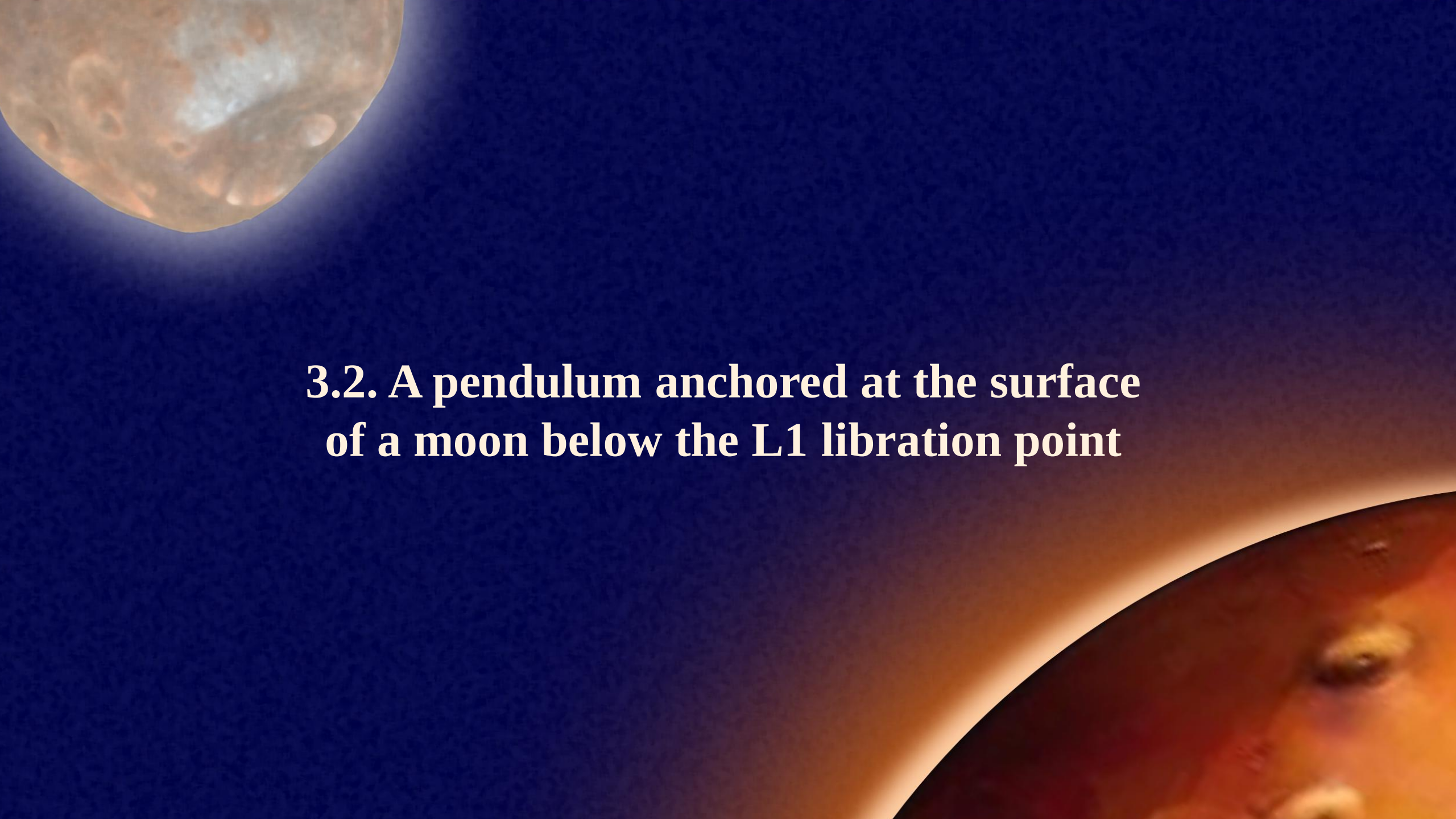

3.2. A pendulum anchored at the surface of a moon below the L1 libration point

Motion equations in the circular case

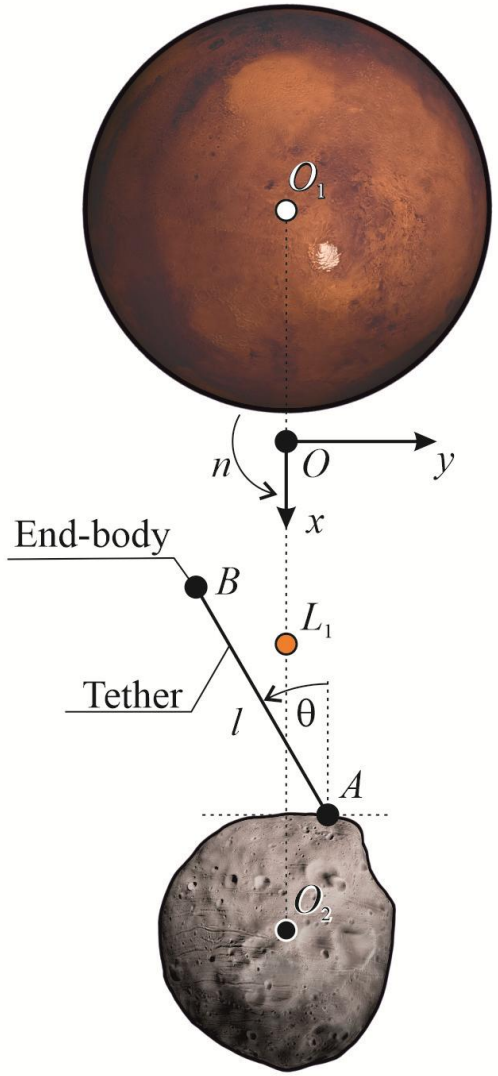

Figure 3.2. Moon-anchored space tether system in Mars-Phobos system.

$$m \ll M_2 \le M_1 \qquad (3.1)$$

$$\ddot{\theta} + F_\theta = 0$$
$$\ddot{l} + F_l = -\frac{1}{m}T \qquad (3.2)$$

$$F_\theta = \frac{n^2}{l}\left(y_A\cos\theta - x_A\sin\theta\right) + \frac{2\dot{l}(n+\dot{\theta})}{l} - \frac{G}{l}\left(\frac{\left(-\left(p\mu + x_A\right)\sin\theta + y_A\cos\theta\right)M_1}{r_1^3}\right.$$
$$\left. + \frac{\left(-\left(p(-1+\mu) + x_A\right)\sin\theta + y_A\cos\theta\right)M_2}{r_2^3}\right) \qquad (3.3)$$

$$F_l = n^2\left(\left(x_A\cos\theta + y_A\sin\theta\right) - l\right) - l\dot{\theta}\left(2n + \dot{\theta}\right)$$
$$-\frac{G}{l}\left(\frac{\left(y_A\sin\theta + \left(x_A + p\mu\right)\cos\theta - l\right)M_1}{r_1^3} + \frac{\left(a_y\sin\theta + \left(y_A + p\left(-1+\mu\right)\right)\cos\theta - l\right)M_2}{r_2^3}\right)$$

- T is the tension force.

Phase portraits and bifurcation diagram in the circular case

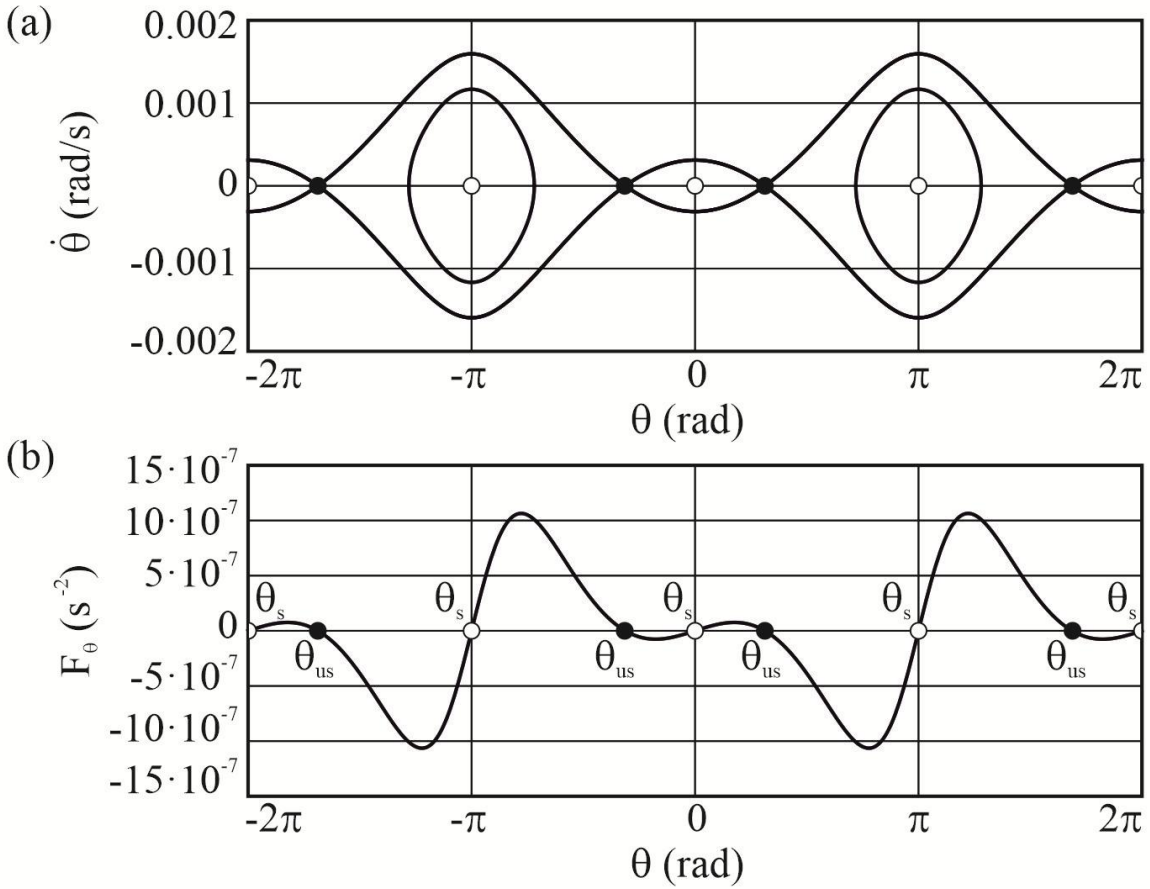

Figure 3.3. a) Phase portrait $\dot{\theta}(\theta)$,
and b) the function $F_\theta(\theta)$ for $l = 4000\,\text{m}$, $y_A = 0$.

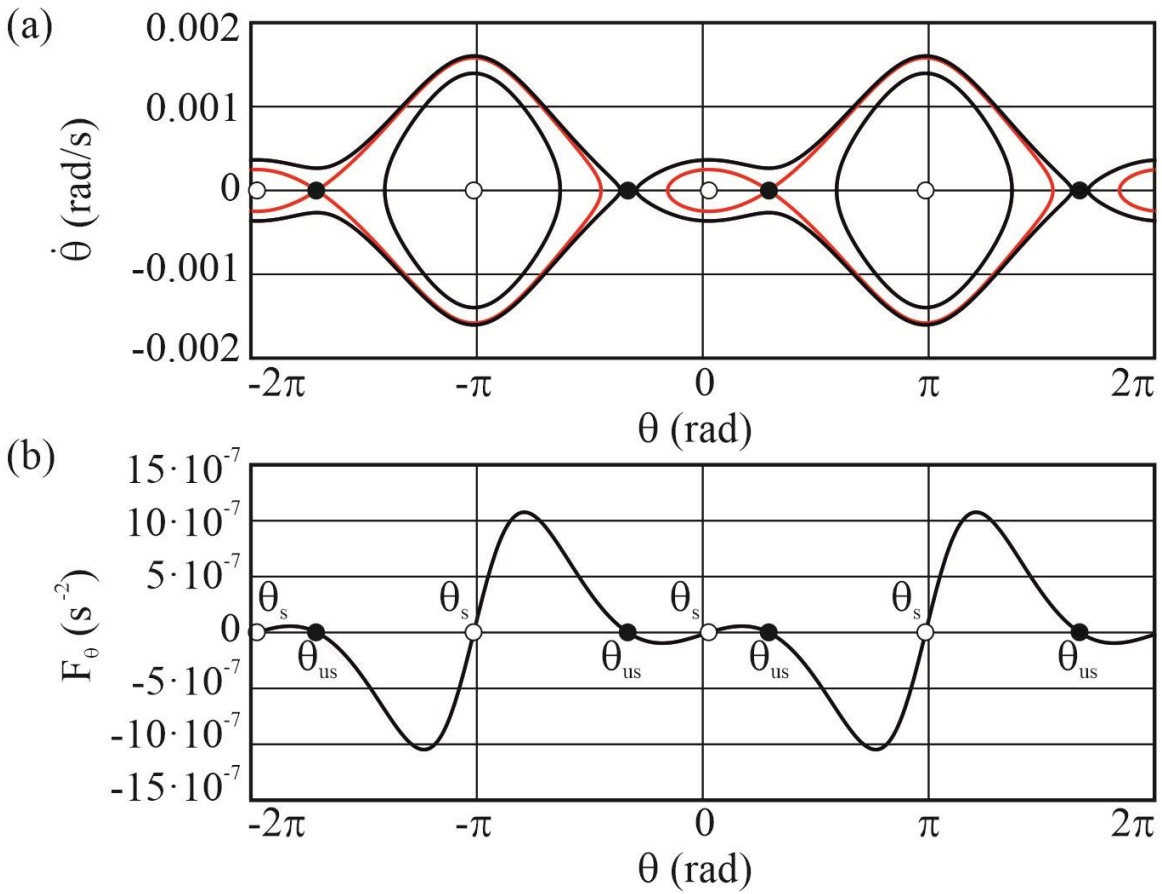

Figure 3.4. a) Phase portrait $\dot{\theta}(\theta)$,
and b) the function $F_\theta(\theta)$ for $l = 4000\,\text{m}$, $y_A = 500$

Phase portraits and bifurcation diagram in the circular case

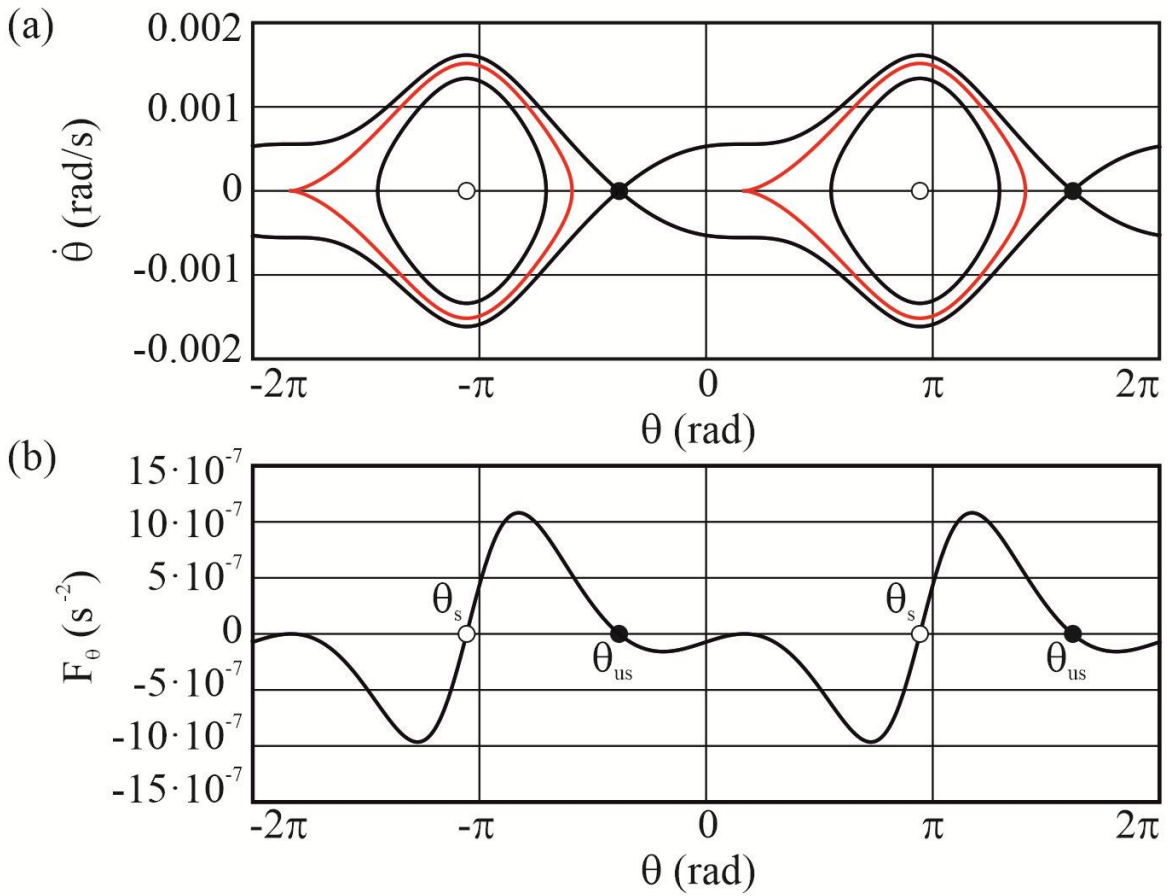

Figure 3.5. a) Phase portrait $\dot{\theta}(\theta)$,
and b) the function $F_\theta(\theta)$ for $l = 4000\,\text{m}$, $y_A = 2091.88$

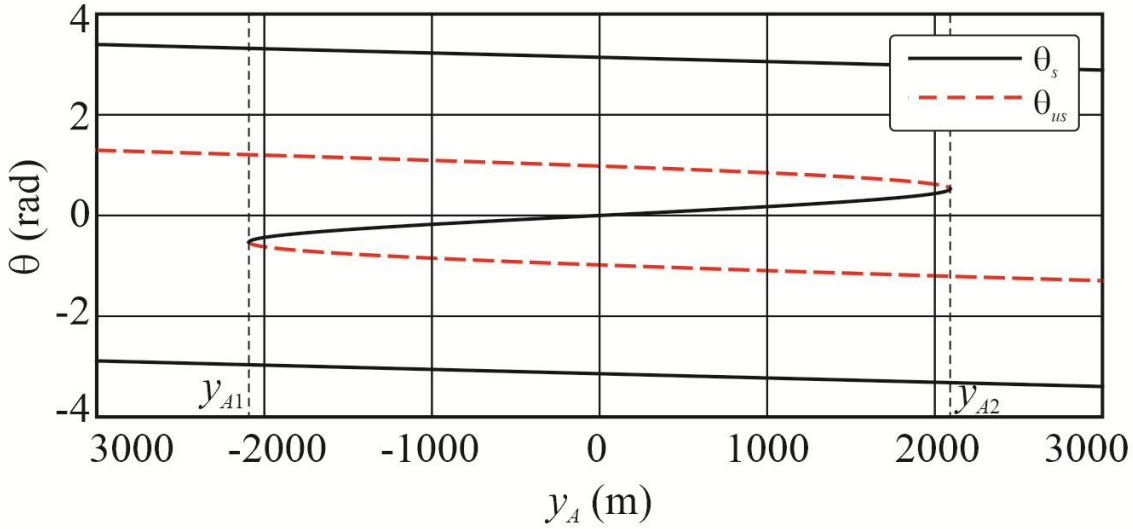

Figure 3.6. Bifurcation diagram.

Tether tension force

$$T = -mF_l = m\Big[n^2\left(l - \left(x_A\cos\theta + y_A\sin\theta\right)\right) + 2nl\dot{\theta} + l\dot{\theta}^2 + \frac{GM_1\left(y_A\sin\theta + \left(x_A + p\mu\right)\cos\theta - l\right)}{r_1^3} + \frac{GM_2\left(y_A\sin\theta + \left(x_A + p\left(-1+\mu\right)\right)\cos\theta - l\right)m_2}{r_2^3}\Big] \qquad (3.4)$$

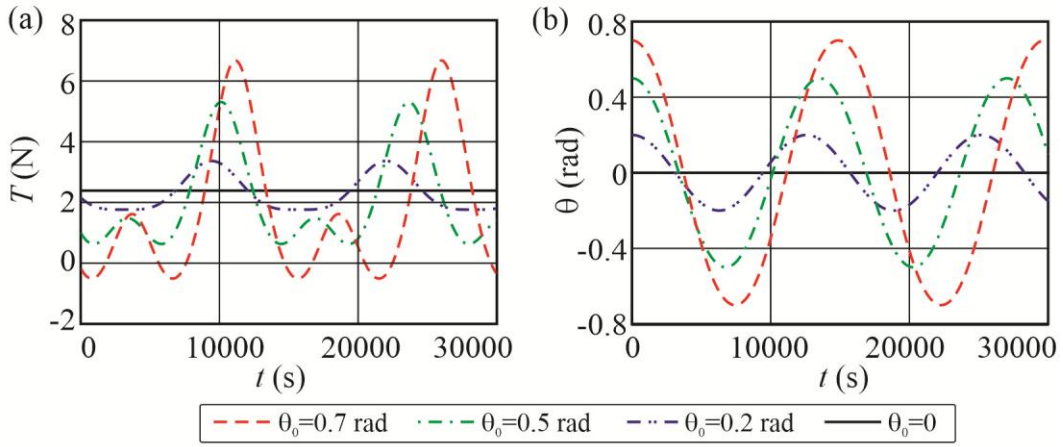

Figure 3.8. a) Tension force and b) deflection angle as a function of time for $l = 5000\,\text{m}$, $y_A = 0$

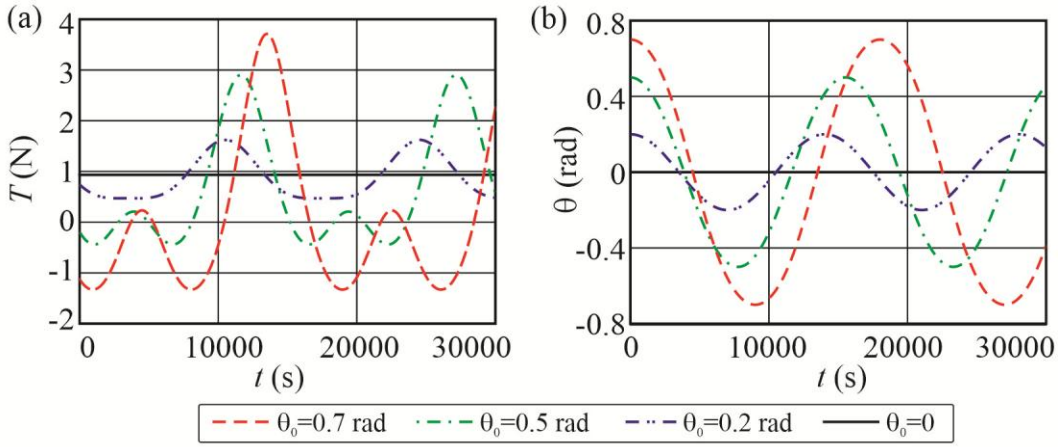

Figure 3.7. a) Tension force and b) deflection angle as a function of time for $l = 4000\,\text{m}$, $y_A = 0$

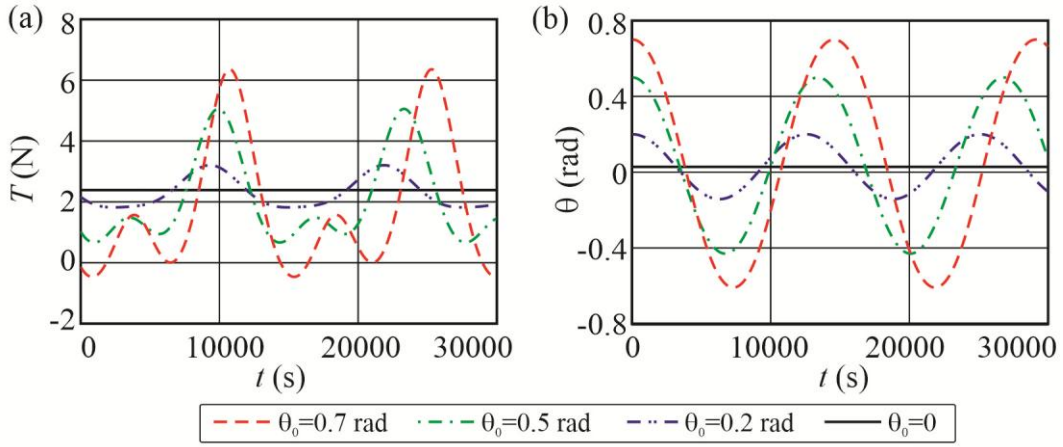

Figure 3.9. a) Tension force and b) deflection angle as a function of time for $l = 5000\,\text{m}$, $y_A = 300$

Tether tension force

$$T = T_U + T_{cf} + T_C \qquad (3.5)$$

- T_U is caused by the influence of potential forces.
- T_{cf} represents the effects of centrifugal force due to inertia.
- T_C represents the effects of Coriolis force.

$$T_U = mn^2\left(l - \left(x_A\cos\theta + y_A\sin\theta\right)\right) + \frac{GmM_1\left(y_A\sin\theta + \left(x_A + p\mu\right)\cos\theta - l\right)}{r_1^3}$$

$$+ \frac{GmM_2\left(y_A\sin\theta + \left(x_A + p\left(-1+\mu\right)\right)\cos\theta - l\right)m_2}{r_2^3}\Bigg]$$

$$T_{cf} = ml\dot{\theta}^2 \qquad (3.6)$$

$$T_C = 2mnl\dot{\theta}$$

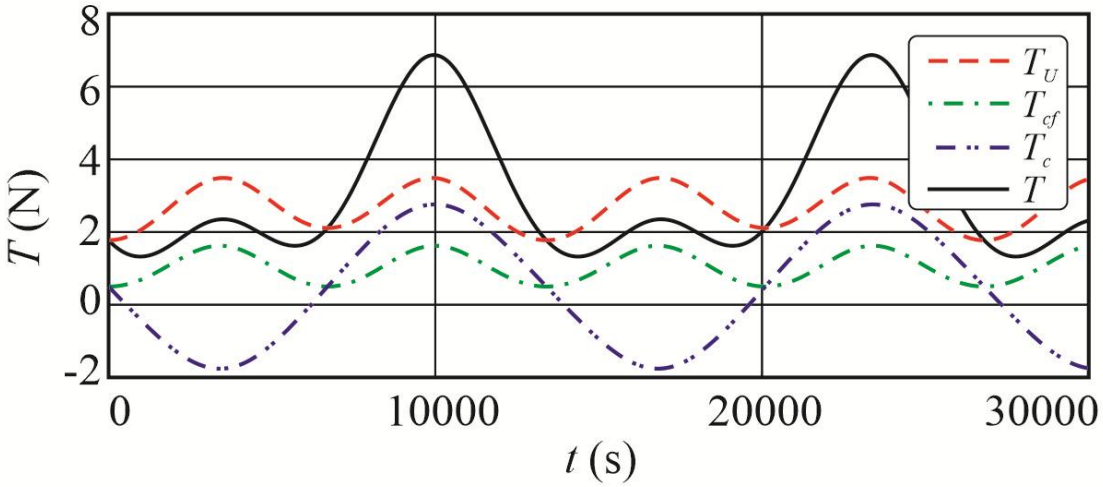

Figure 3.10. Tension force and its components for $l = 5000\,\text{m}$, $y_A = 300\ \text{m}$, $\theta_0 = 0.5\ \text{rad}$

Feedback control for tether stabilization

Feedback control law

$$u = -c_\omega \dot{\theta} \qquad c_\omega > 0 \qquad (3.7)$$

A Lyapunov function

$$V = \frac{\dot{\theta}^2}{2} + \frac{n^2}{l}\left(x_A \cos\theta + y_A \sin\theta\right) - \frac{G}{l^2}\left(\frac{M_1}{r_1} + \frac{M_2}{r_2}\right) - W_s \qquad (3.8)$$

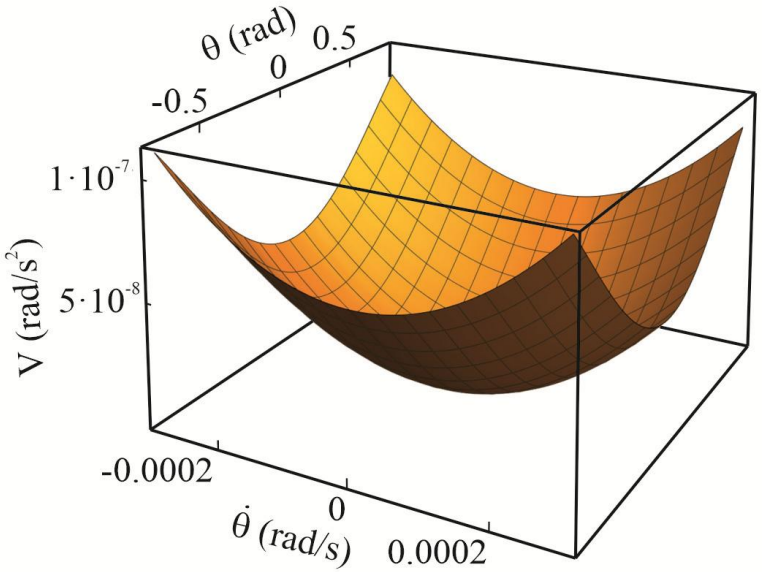

Figure 3.11. The Lyapunov function.

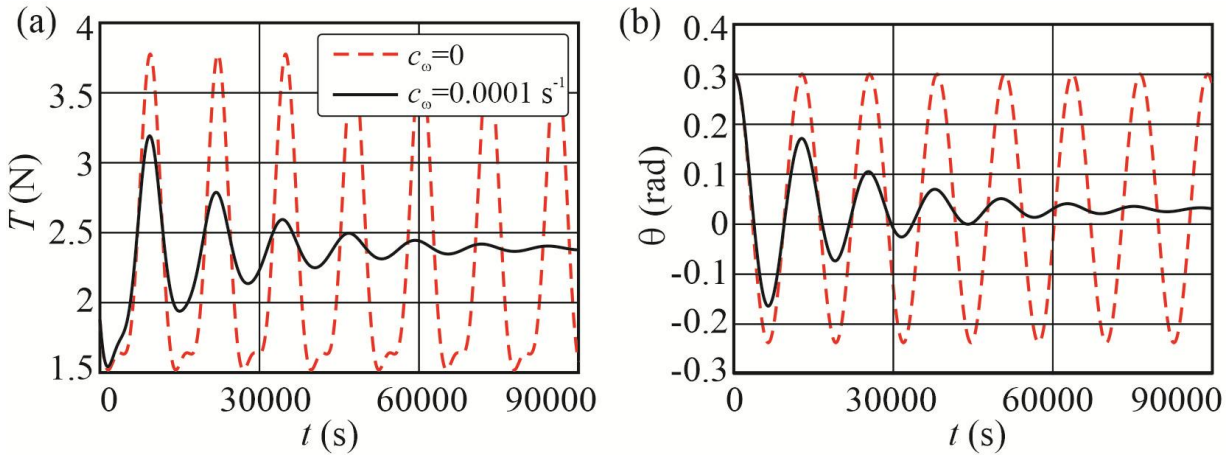

Figure 3.12. a) The tension force and b) the tether deflection angle for the initial point $\theta_0 = 0.3\,\text{rad}$, $\dot{\theta}_0 = 0$ rad/s.

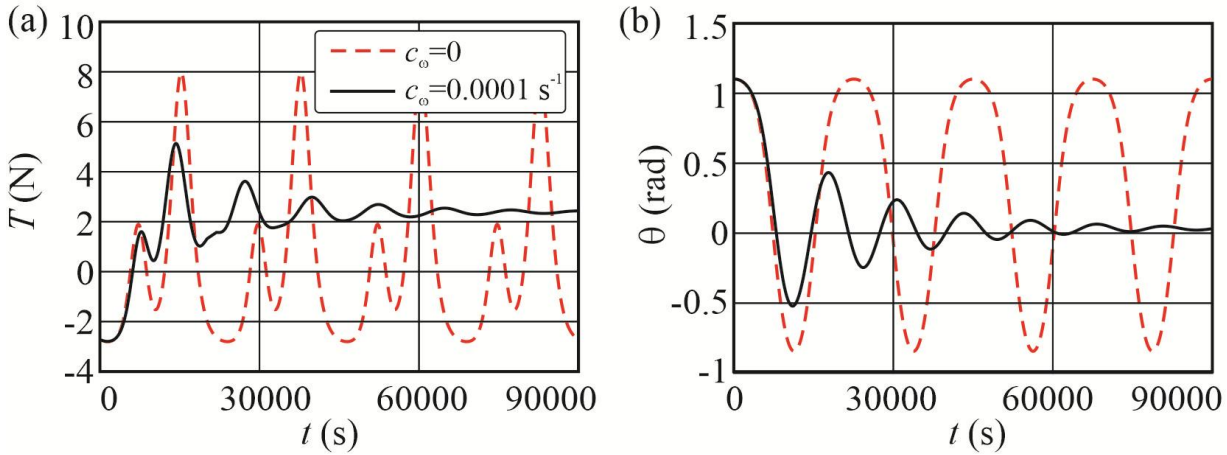

Figure 3.13. a) The tension force and b) the tether deflection angle for the initial point $\theta_0 = 1.1\,\text{rad}$, $\dot{\theta}_0 = 0$ rad/s.

Validation for the anchored tether within an elliptic restricted three-body problem

$$\theta'' + \Phi_\theta = -c_\omega \frac{r^2}{\sqrt{G\left(M_1 + M_2\right) p}} \theta' \qquad (3.9)$$

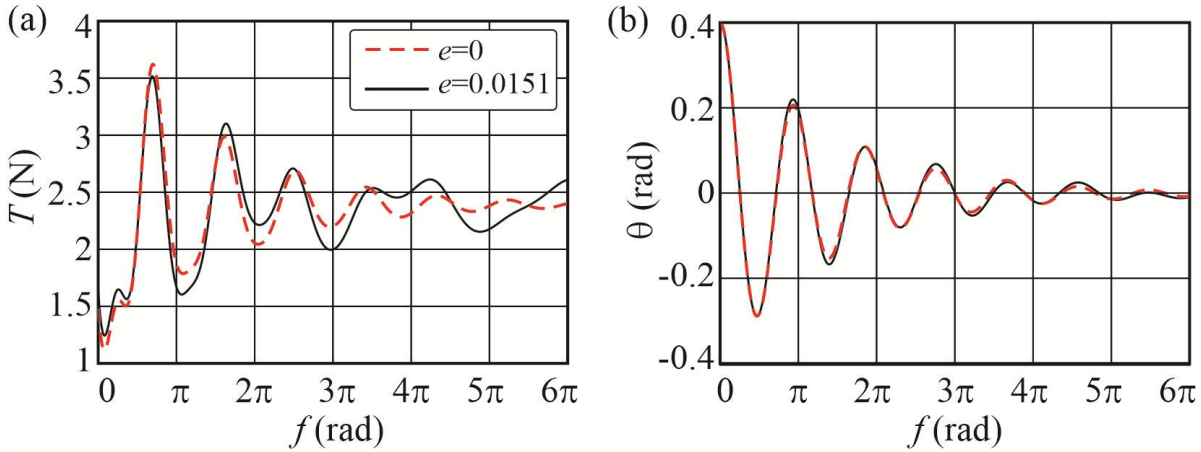

Figure 3.15. a) The tension force and b) the tether deflection angle for the uncontrolled motion ($c_\omega = 0.0001$) of 5000m tether.

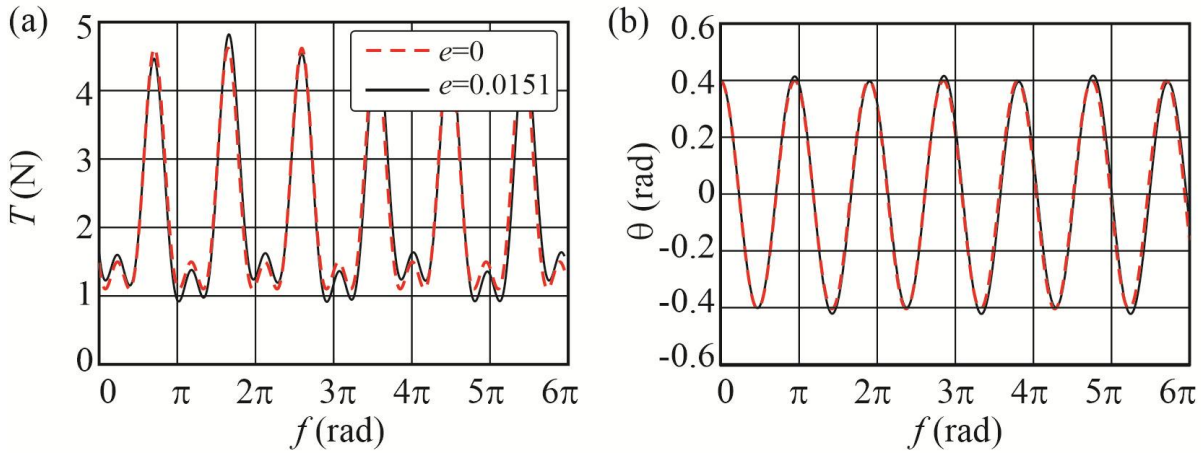

Figure 3.14. a) The tension force and b) the tether deflection angle for the uncontrolled motion ($c_\omega = 0$) of 5000m tether.

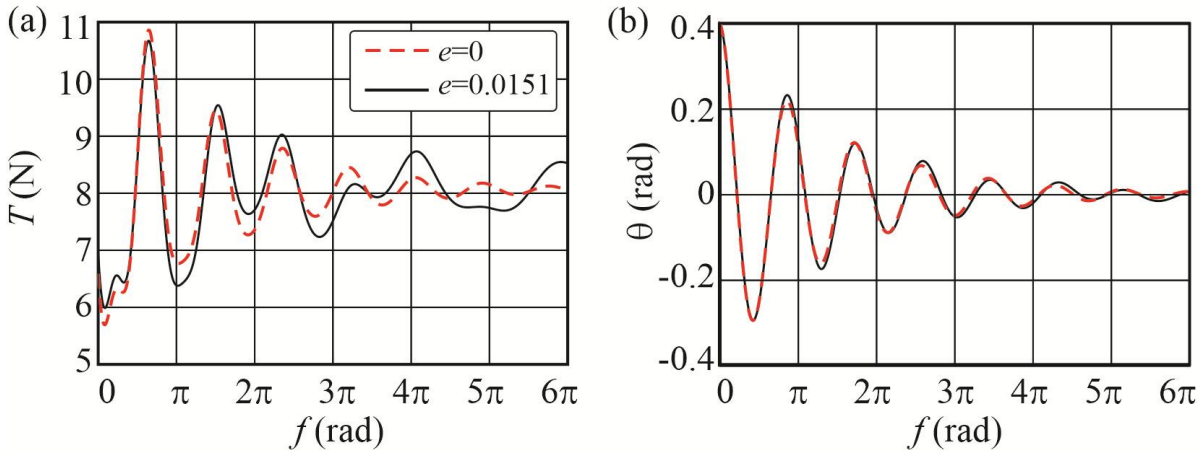

Figure 3.16. a) The tension force and b) the tether deflection angle for the uncontrolled motion ($c_\omega = 0.0001$) of 10000m tether.

3.3. Chaotic oscillations of an anchored pendulum below the L1 libration point

Perturbed and unperturbed motion of a constant length tether

$$\theta'' + \Phi_\theta = 0 \qquad (3.10)$$

$$\Phi_\theta = -\frac{\sin\theta}{\lambda k^2}\left(\bar{x}_A + \frac{(-1+\mu)(\mu+\bar{x}_A)}{\rho_1^3} - \frac{\mu(-1+\mu+\bar{x}_A)}{\rho_2^3}\right) - \frac{2e}{k}(1+\theta')\sin f \qquad (3.11)$$

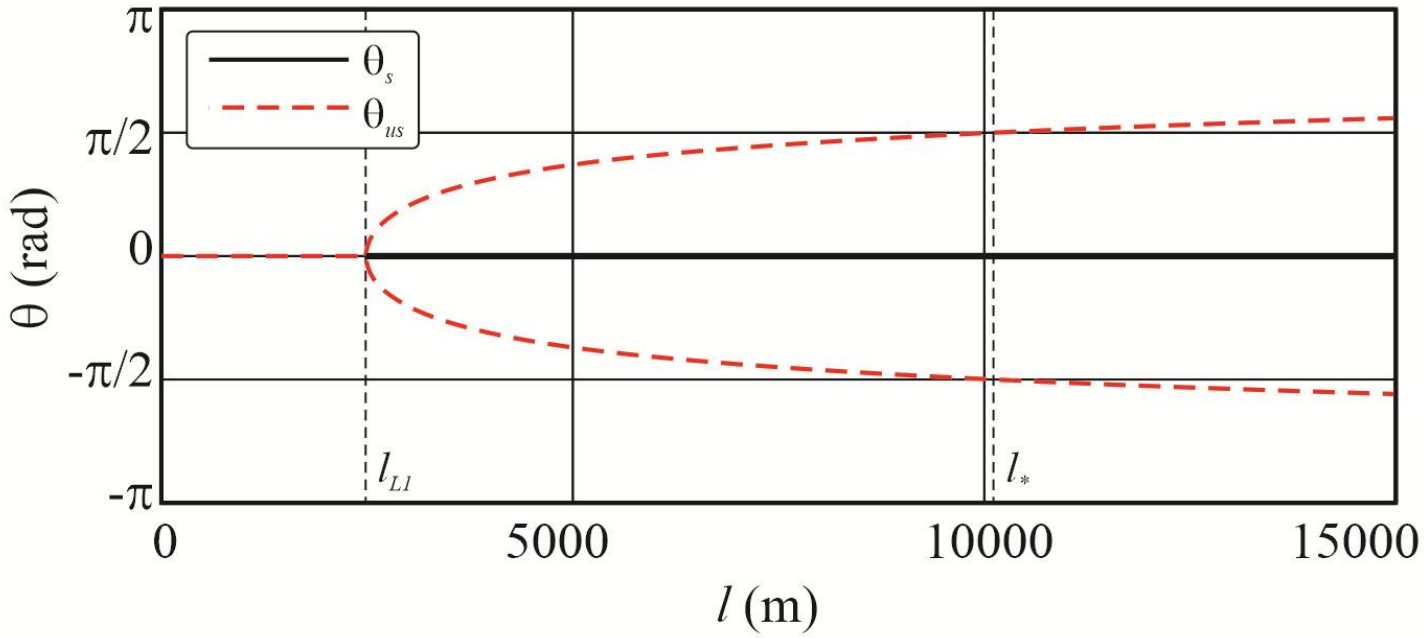

Figure 3.17. Bifurcation diagram for the Mars-Phobos system.

Chaos detection

$$\Phi_{\theta d} = \frac{2e}{1+e\cos f}\left(1+\theta'\right)\sin f \qquad (3.12)$$

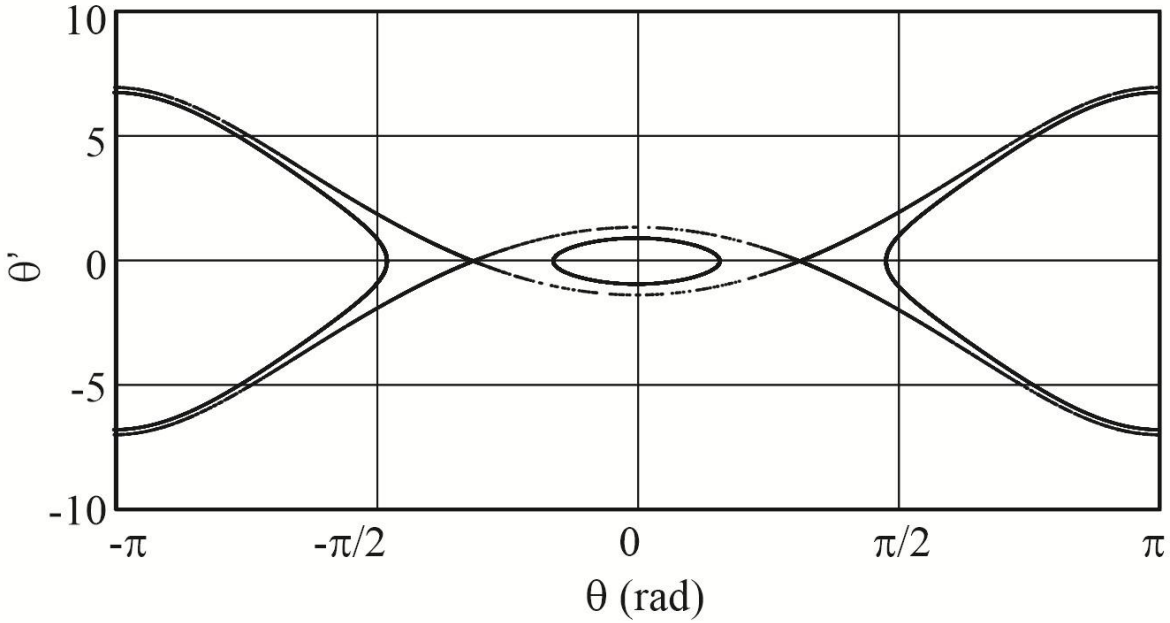

Figure 3.18. Poincare section for the unperturbed case (*e = 0*).

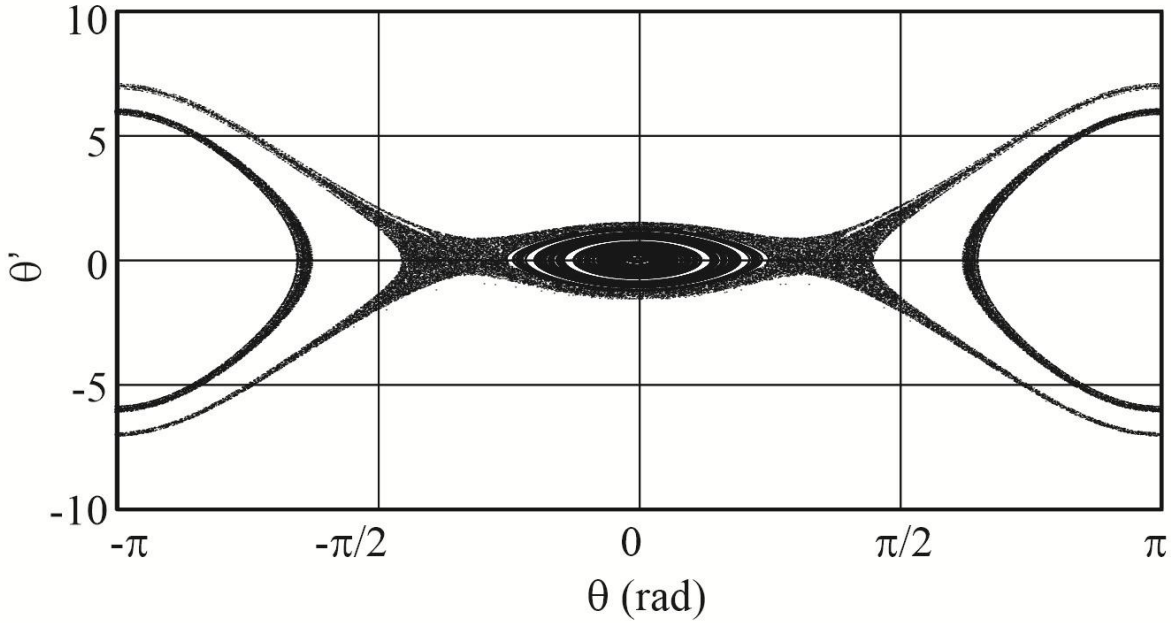

Figure 3.19. Poincare section for the perturbed case (*e = 0.0151*).

Tether length control for chaos suppression. Melnikov function

$$M^{\pm}(f_0) = e\left(I_C^{\pm}\sin f_0 + I_S^{\pm}\cos f_0\right) + k_\theta I_A^{\pm} \qquad (3.13)$$

$$k_\theta^{\pm} > \frac{\sqrt{\left(I_C^{\pm}\right)^2 + \left(I_S^{\pm}\right)^2}}{\left|I_A^{\pm}\right|} = k_*^{\pm} \qquad (3.14)$$

- $k_*^{\pm}$ is the critical value of the control coefficient.

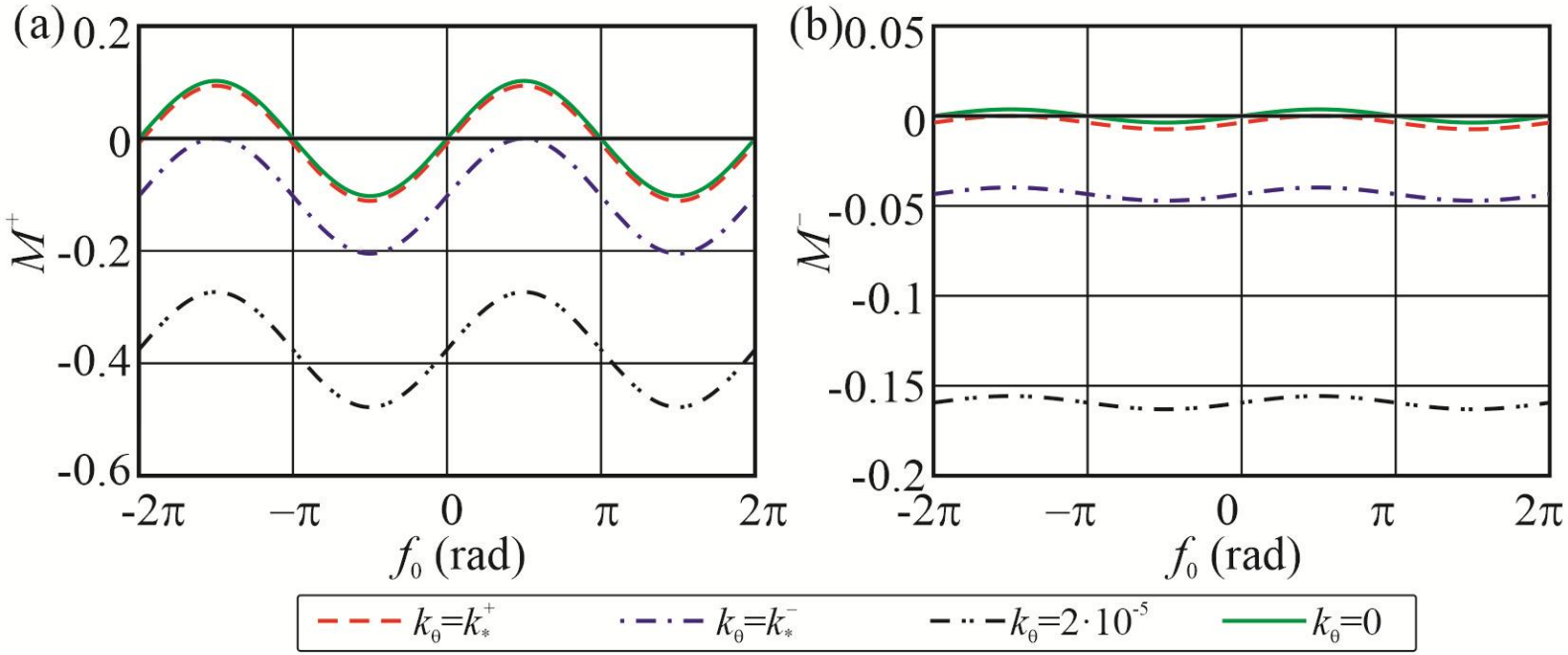

Figure 3.20. The Melnikov function for the a) upper branch of separatrix $M^+(f_0)$, and b) for the lower branch of separatrix $M^-(f_0)$.

Tether length control for chaos suppression. Melnikov function

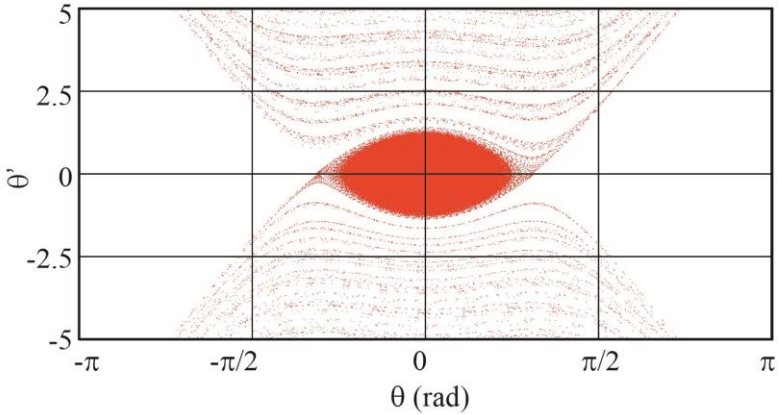

Figure 3.21. Poincare sections for $k_\theta = k_*^- = 0.461\times10^{-6},\ l = 4000\text{m}$

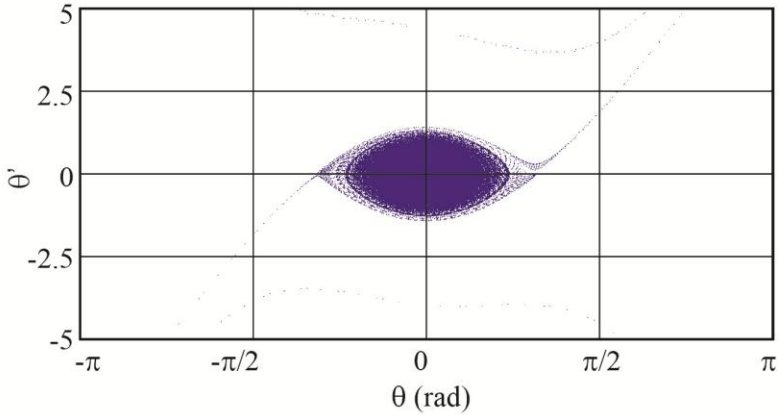

Figure 3.22. Poincare sections for $k_\theta = k_*^+ = 0.545\times10^{-5},\ l = 4000\text{m}$

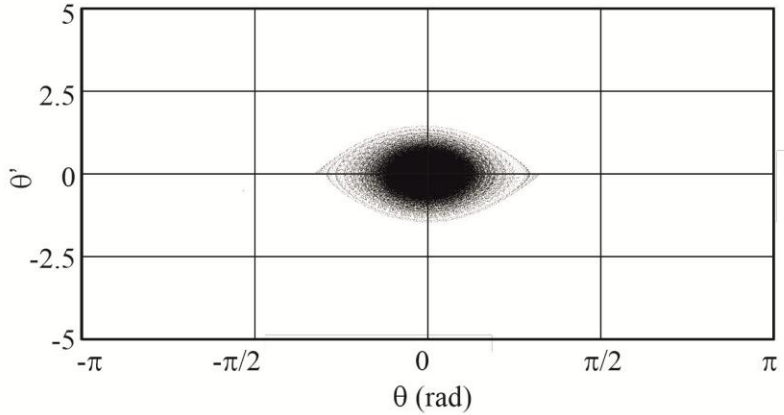

Figure 3.23. Poincare sections for $k_\theta = 2\times10^{-5},\ l = 4000\text{m}$

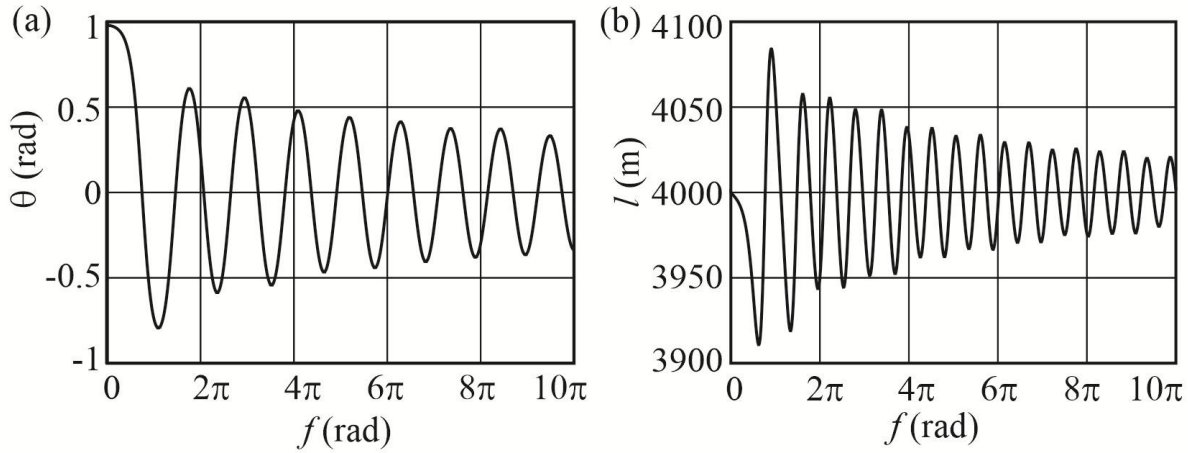

Figure 3.24. The tether length history of true anomaly during chaos suppression for $k_\theta = 2\times10^{-5},\ l = 4000\text{m}$.

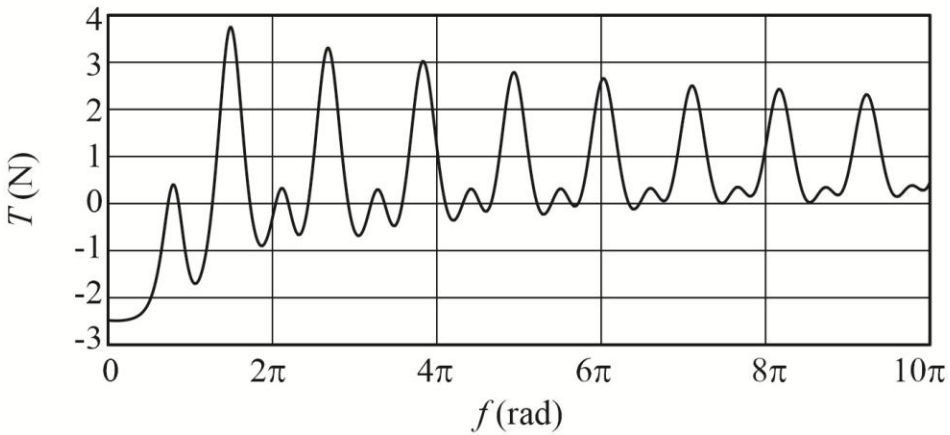

Figure 3.25. Dependence of the tether tension force T on true anomaly during chaos suppression.

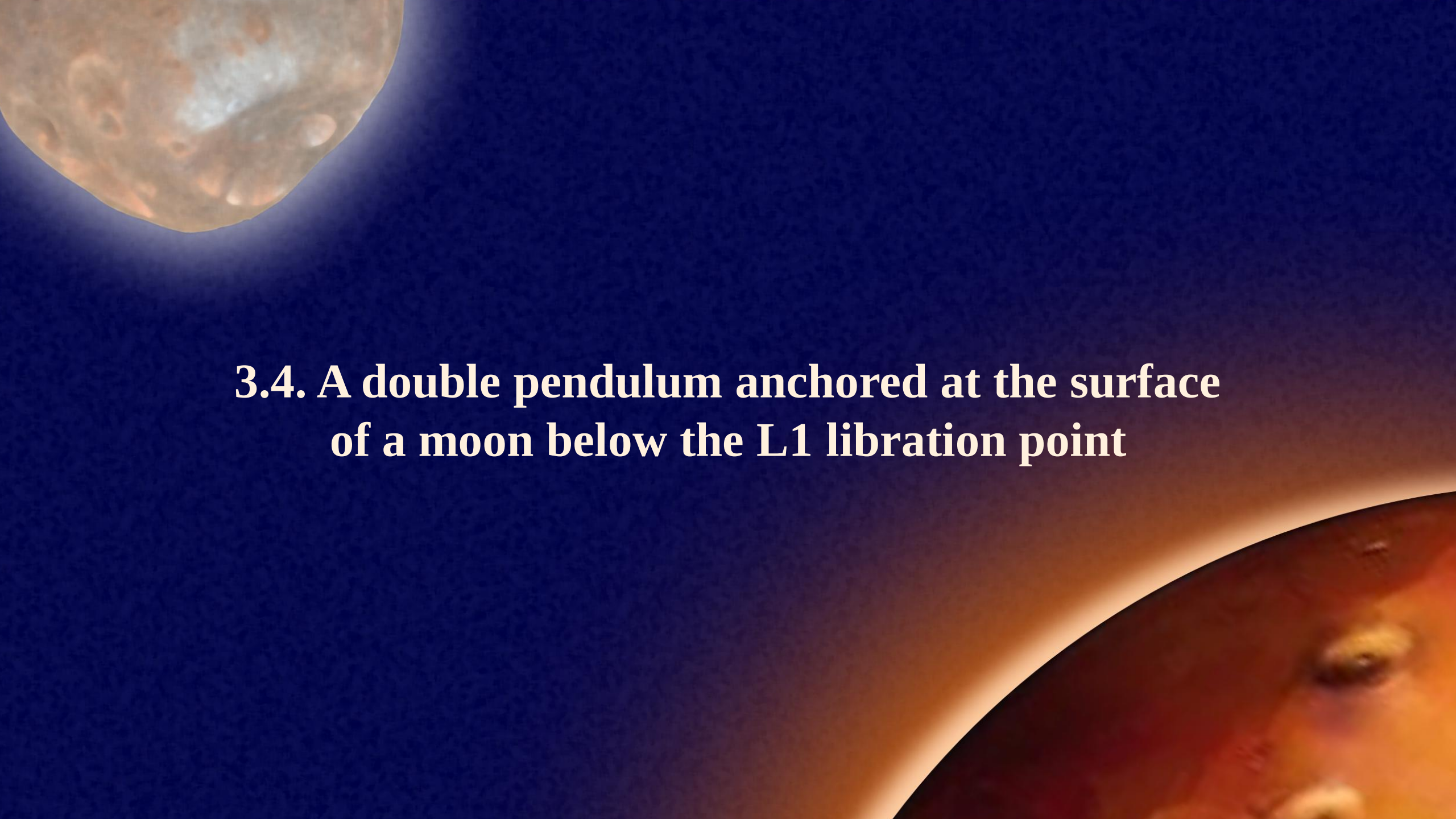

3.4. A double pendulum anchored at the surface of a moon below the L1 libration point

Equation of motion of a double pendulum anchored on the moon

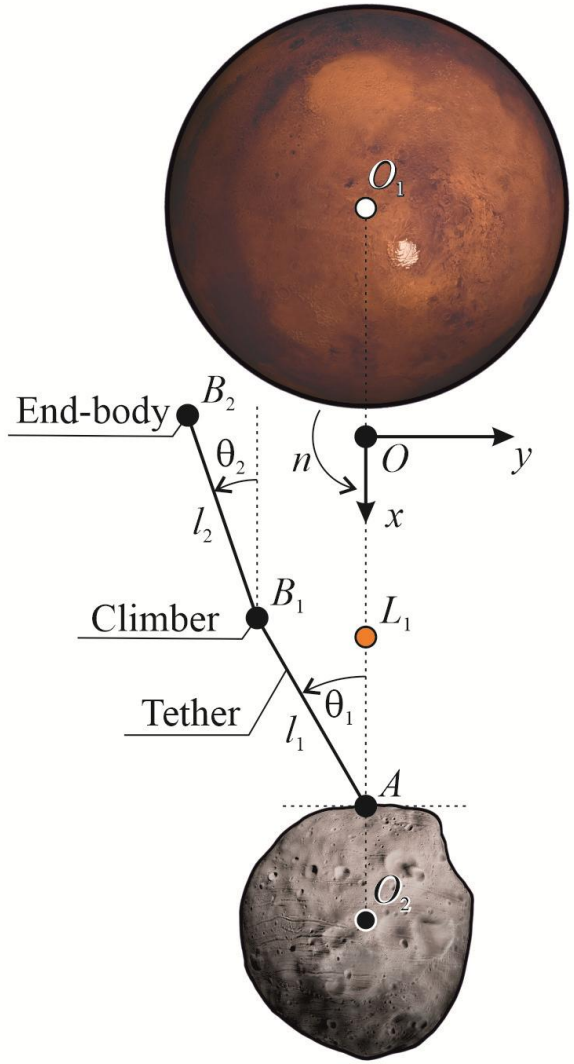

Figure 3.26. Double pendulum
in the circular restricted three-body problem.

$$M_1 > M_2 >> m_2 > m_1 \qquad (3.15)$$

$$l_1\left(\lambda\sigma\dot{\theta}_2\sin\theta_{12}\left(2n+\dot{\theta}_2\right)+(1+\sigma)\ddot{\theta}_1+\lambda\sigma\left(n^2\sin\theta_{12}+\cos\theta_{12}\ddot{\theta}_2\right)\right)-an^2(1+\sigma)\sin\theta_1$$
$$+GM_1\left(\frac{\rho_1\sin\theta_1}{r_{11}^3}+\frac{\sigma\left(\rho_1\sin\theta_1-\lambda l_1\sin\theta_{12}\right)}{r_{21}^3}\right)$$
$$+GM_2\left(\frac{\rho_2\sin\theta_1}{r_{12}^3}+\frac{\sigma\left(\rho_2\sin\theta_1-\lambda l_1\sin\theta_{12}\right)}{r_{22}^3}\right)=0 \qquad (3.16)$$

$$-an^2\sin\theta_2+l_1\left(-\sin\theta_{12}\left(n^2+2n\dot{\theta}_1+\dot{\theta}_1^2\right)+\cos\theta_{12}\ddot{\theta}_1+\lambda\ddot{\theta}_2\right)$$
$$+\frac{GM_1\left(\rho_1\sin\theta_2+\sin\theta_{12}l_1\right)}{r_{21}^3}+\frac{GM_2\left(\rho_2\sin\theta_2+\sin\theta_{12}l_1\right)}{r_{22}^3}=0$$

- $\theta_{12}=\theta_1-\theta_2$

Evolution of the generalized potential energy near zero equilibrium

$$U^* = -\frac{m_1 n^2}{2}\Big[(1+\sigma)a^2 - 2\big((1+\sigma)\cos\theta_1 + \lambda\sigma\cos\theta_2\big)al_1$$
$$+\big(1+\sigma+\lambda^2\sigma+2\lambda\sigma\cos\theta_{12}\big)l_1^2\Big] - G\,m_1\left[\left(\frac{M_1}{r_{11}}+\frac{M_2}{r_{12}}\right)+\sigma\left(\frac{M_1}{r_{21}}+\frac{M_2}{r_{22}}\right)\right] \qquad (3.17)$$

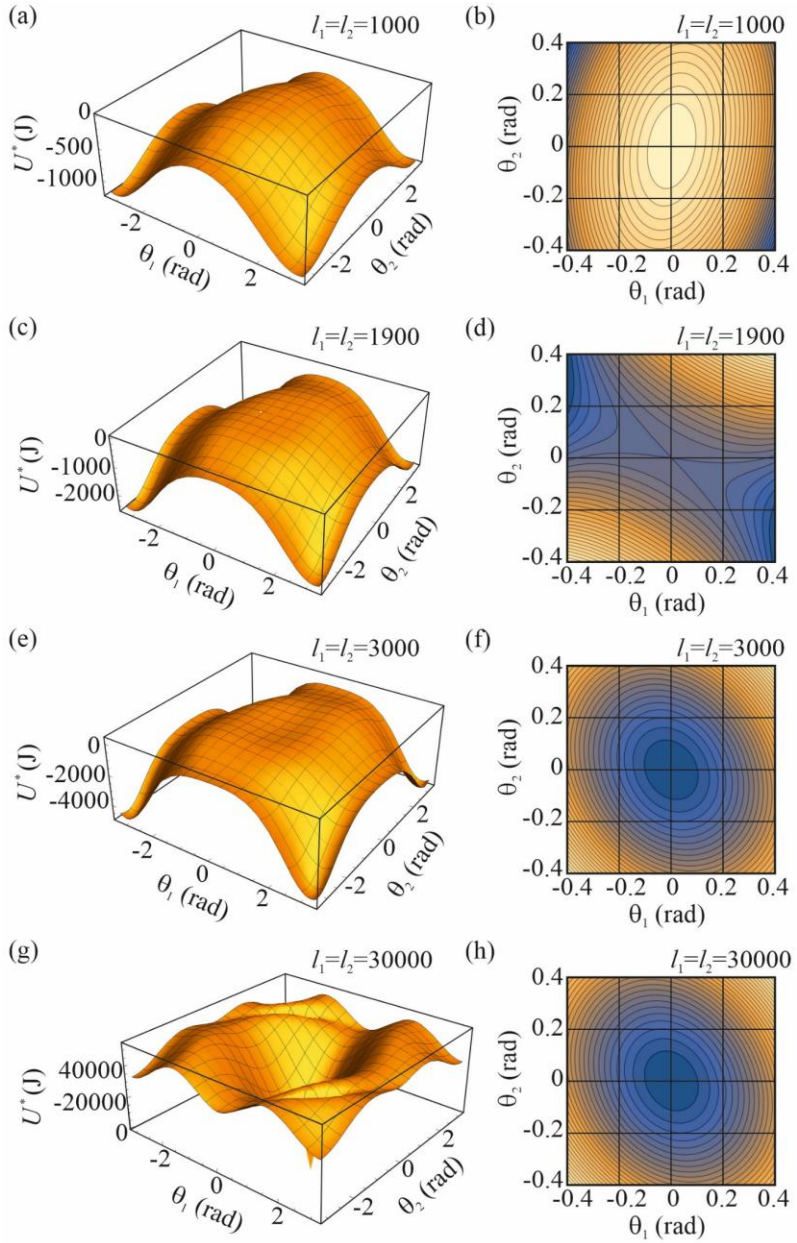

Figure 3.27. Surfaces of the generalized potential energy U^* for various lengths of the pendulum links.

Small motions near zero equilibrium

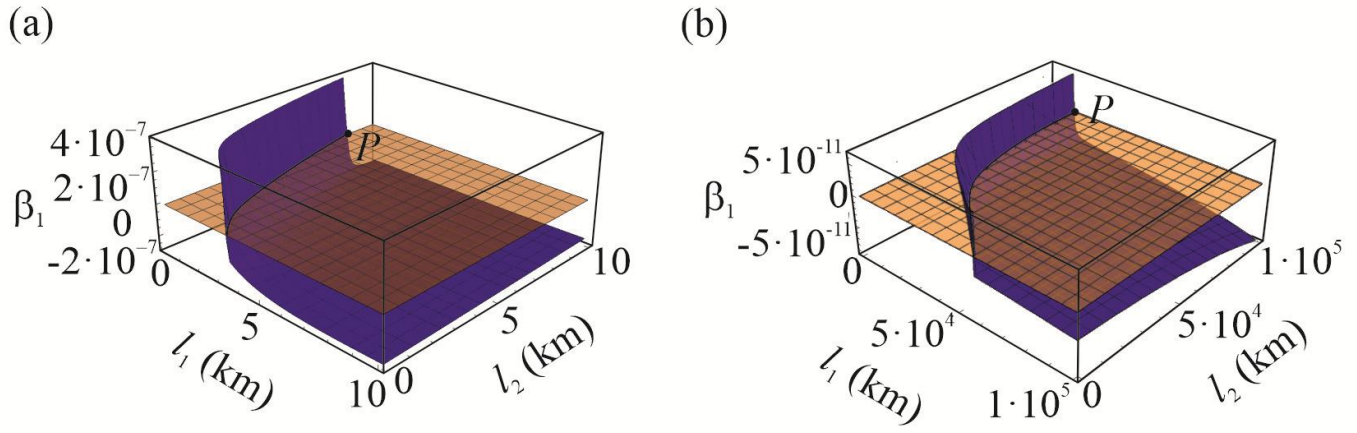

Figure 3.28. Dependence of the square of the natural frequency β_1 on the length of the links l_1, l_2 of the equal mass double pendulum $\sigma = 1$ for the a) Mars-Phobos, b) Earth-Moon systems.

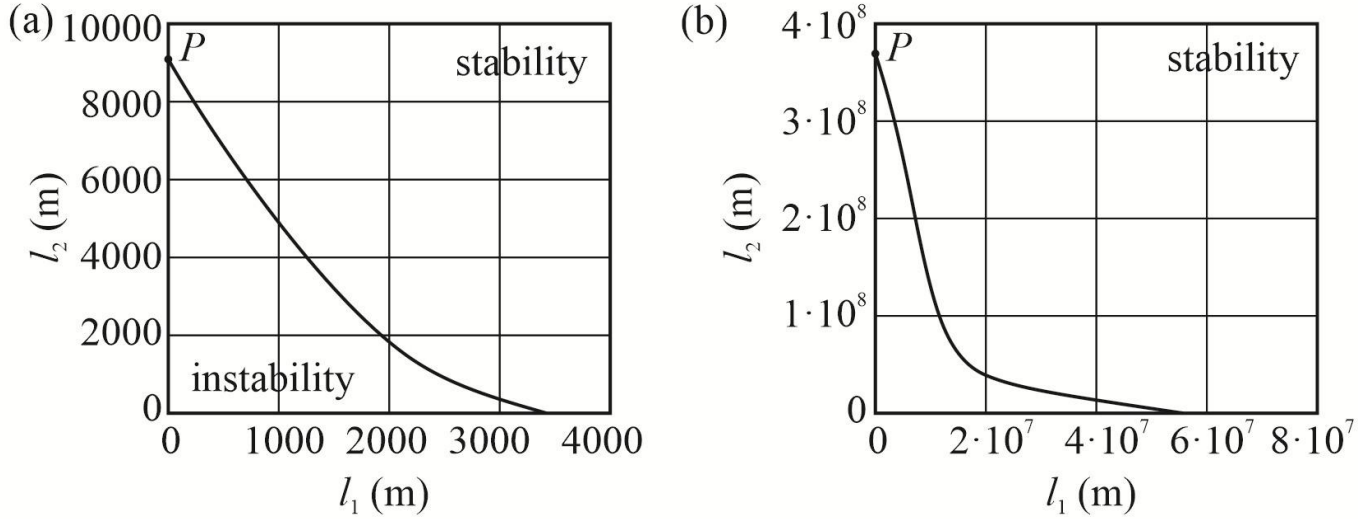

Figure 3.29. The boundary between stable and unstable region for the a) Mars-Phobos, b) Earth-Moon systems.

Impossibility of building a Moon-anchored space elevator

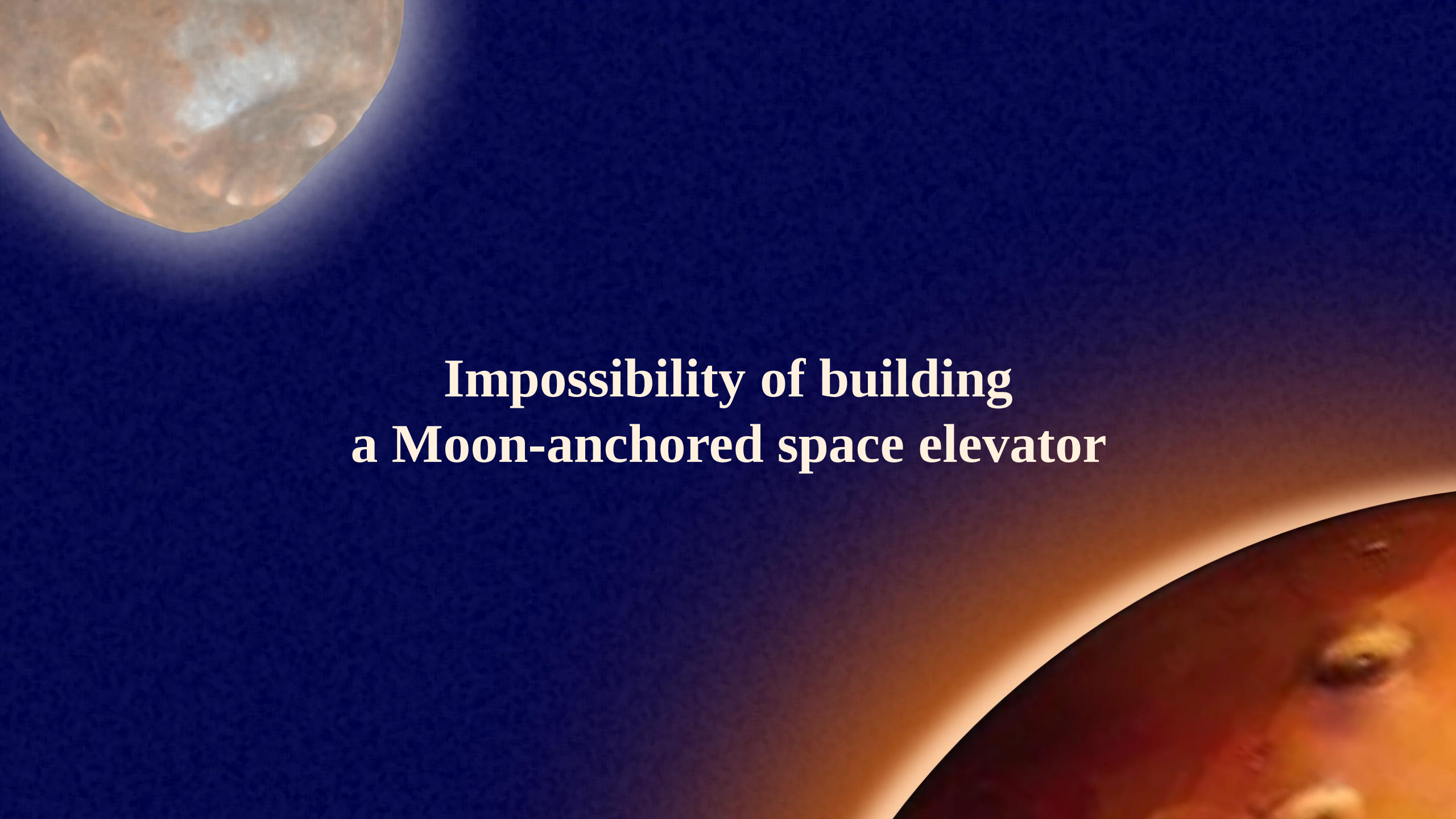

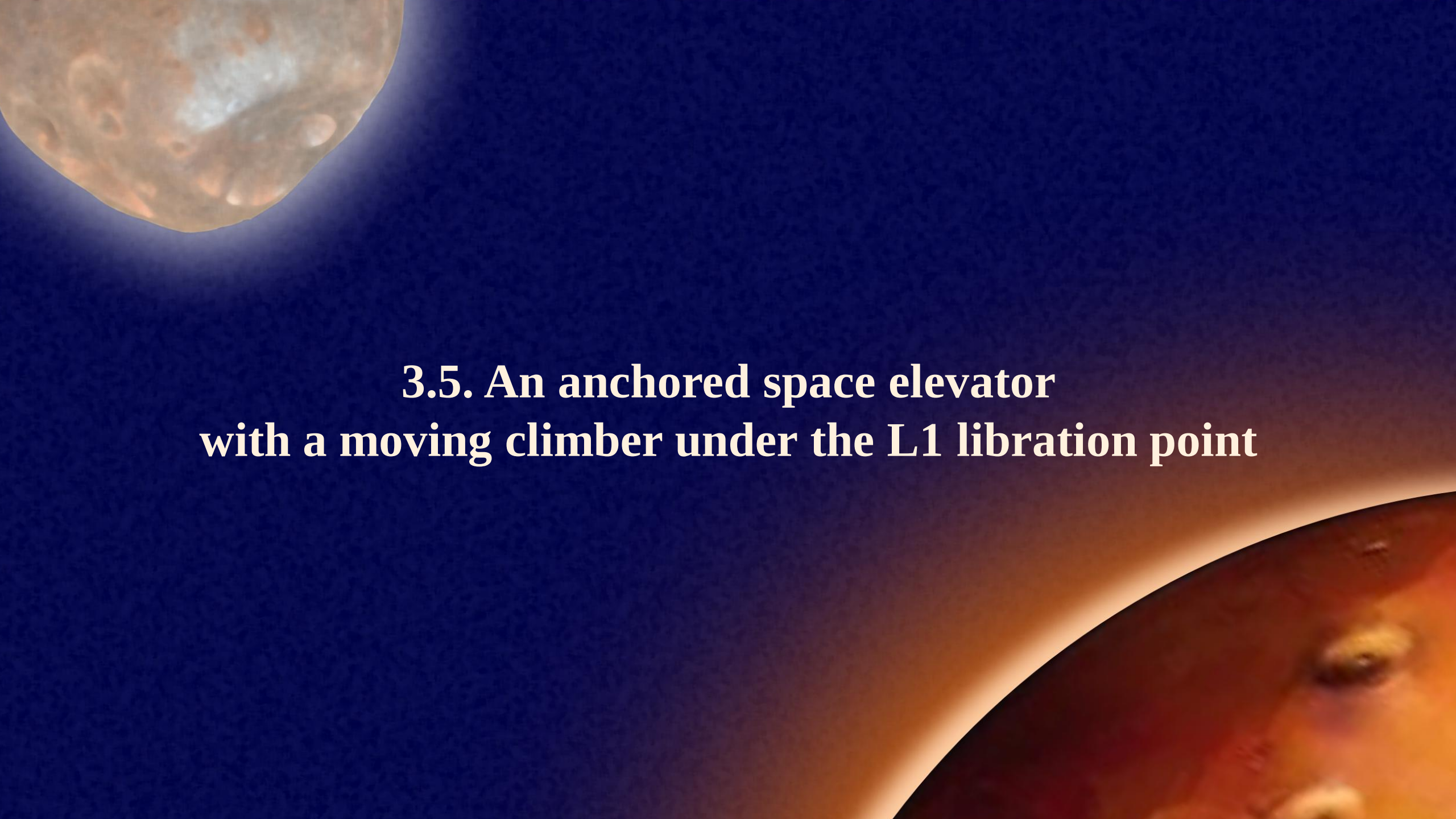

3.5. An anchored space elevator with a moving climber under the L1 libration point

Two possible configurations of a space elevator

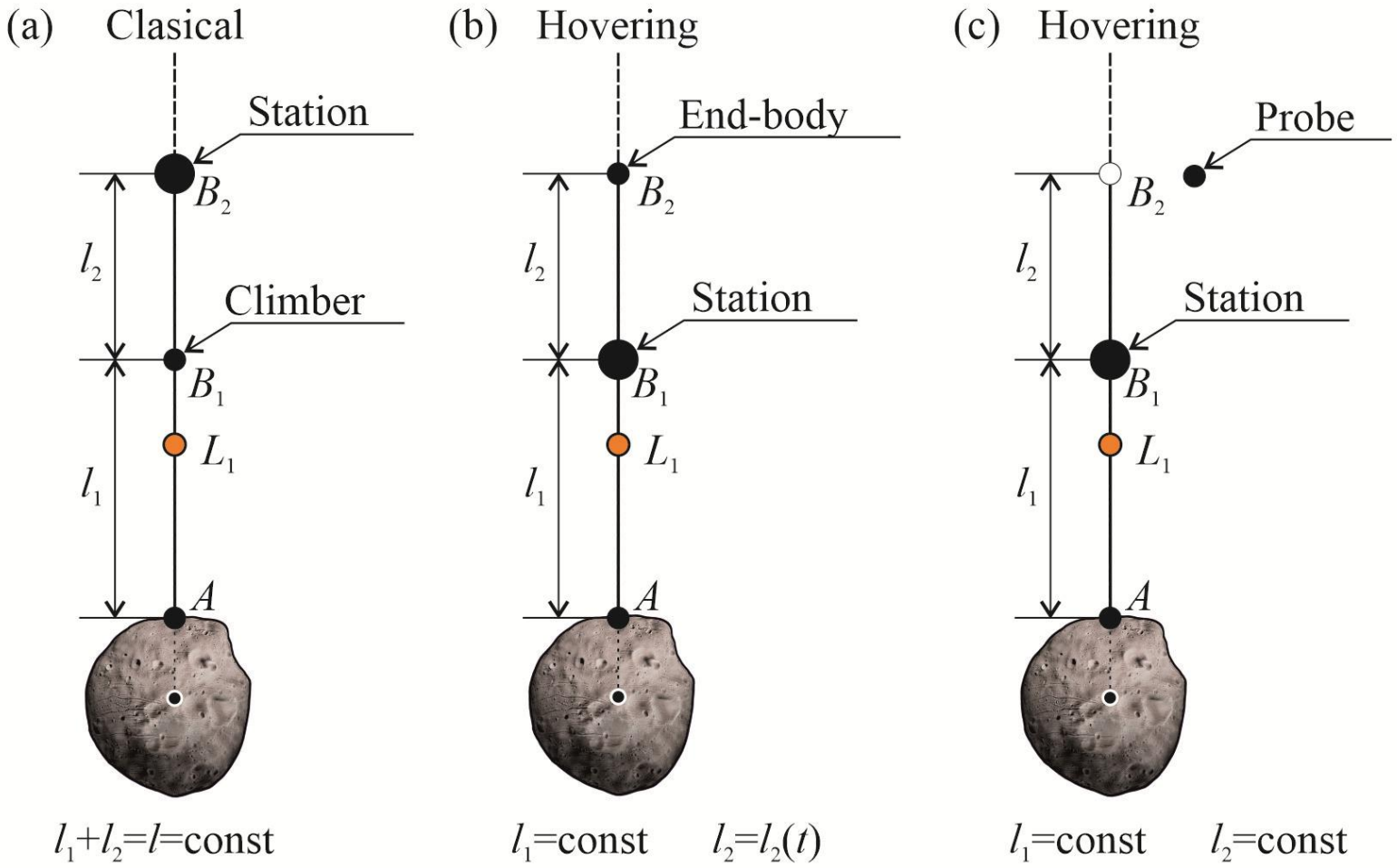

Figure 3.30. Two configurations of space elevator: a) standard, b) and c) hovering.

The classic lunar-anchored space elevator:

$$l = l_1 + l_2 = const \qquad (3.18)$$

A hovering lunar space elevator:

$$l_1 = const,\ l_2 = l_2(t) \qquad (3.19)$$

Numerical simulation of the classical lunar space elevator

$$\theta_1 = 0.1\,\text{rad},\ \theta_2 = -0.05\,\text{rad},\ \dot{\theta}_1 = \dot{\theta}_2 = 0 \qquad (3.20)$$

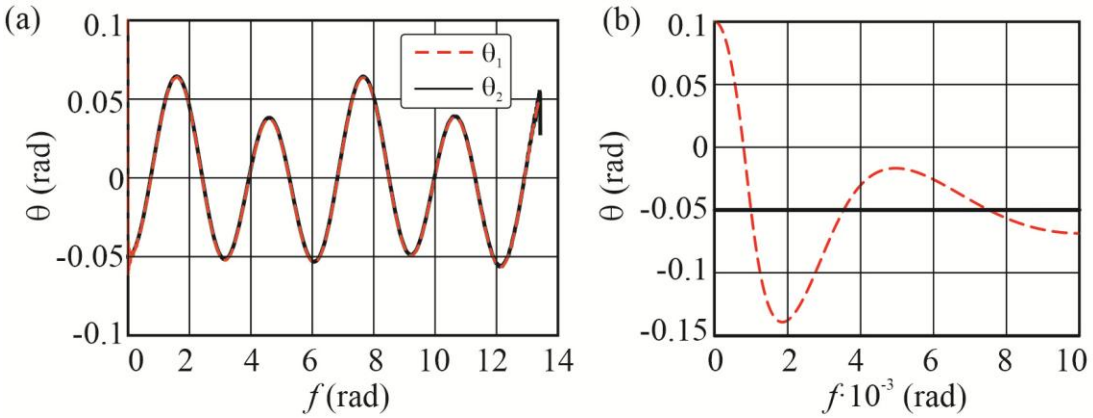

Figure 3.31. The tethers' deflection angles θ_1, θ_2 during the climber's ascent with initial conditions (3.20).

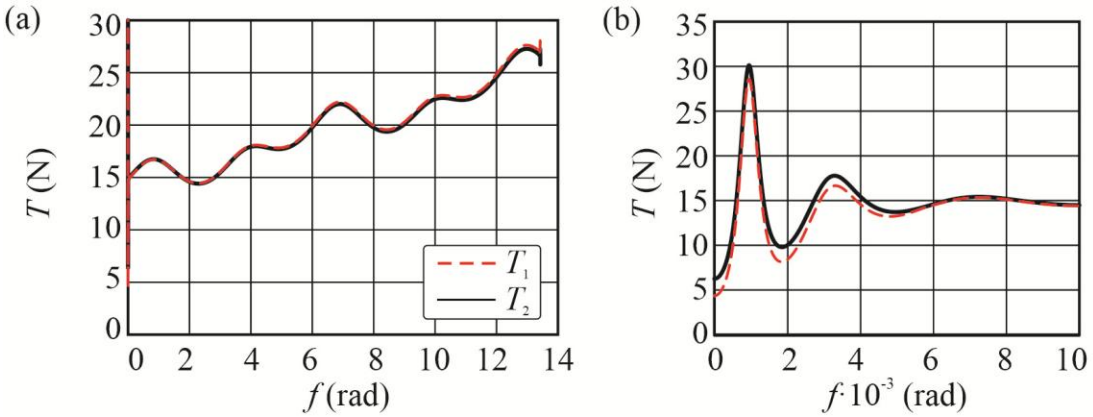

Figure 3.32. The tethers' tension forces T_1, T_2 during the climber's ascent with initial conditions (3.20).

$$\theta_1 = \theta_2 = 0,\ \dot{\theta}_1 = \dot{\theta}_2 = 0 \qquad (3.21)$$

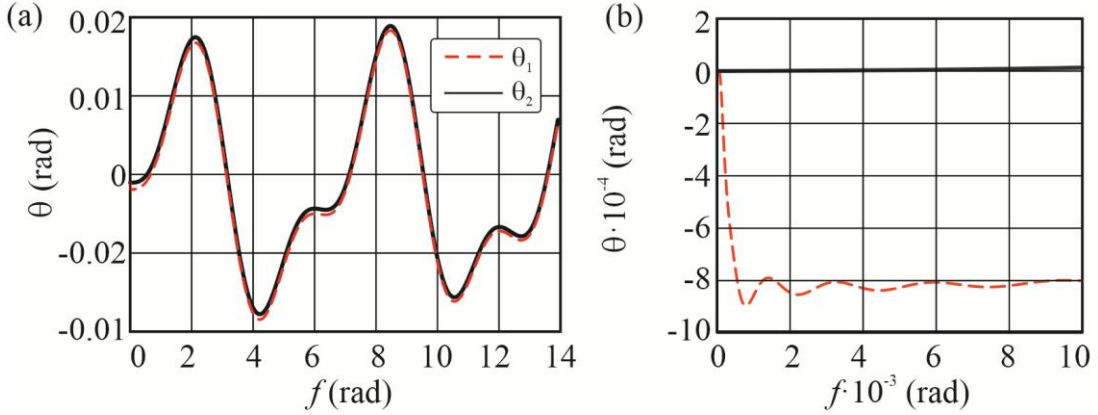

Figure 3.33. The tethers' deflection angles θ_1, θ_2 during the climber's ascent with initial conditions (3.21).

Numerical simulation of the classical lunar space elevator

$$\theta_1 = 0.1\,\text{rad},\ \theta_2 = -0.05\,\text{rad},\ \dot{\theta}_1 = \dot{\theta}_2 = 0 \qquad (3.20)$$

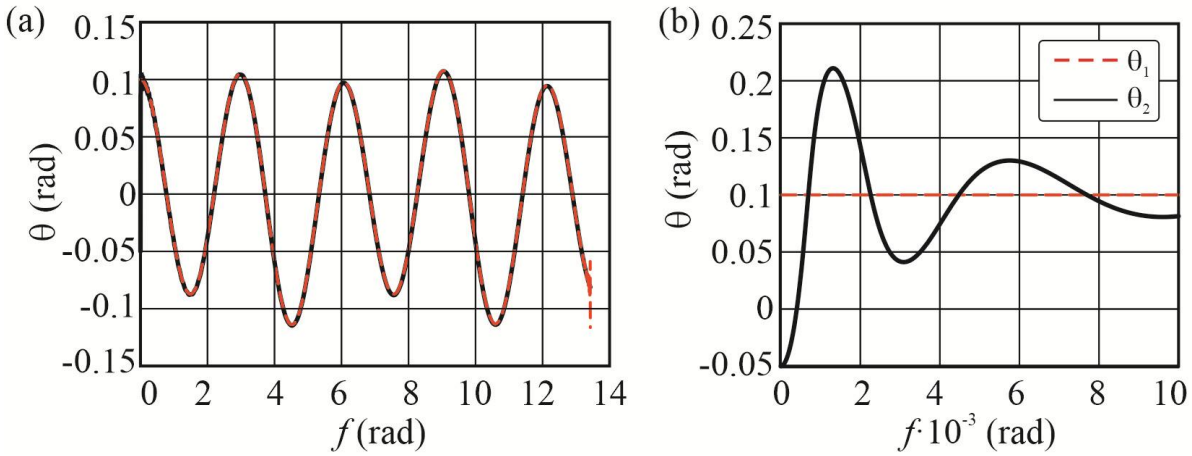

Figure 3.34. The tethers' deflection angles θ_1, θ_2 during the climber's descent with initial conditions (3.20).

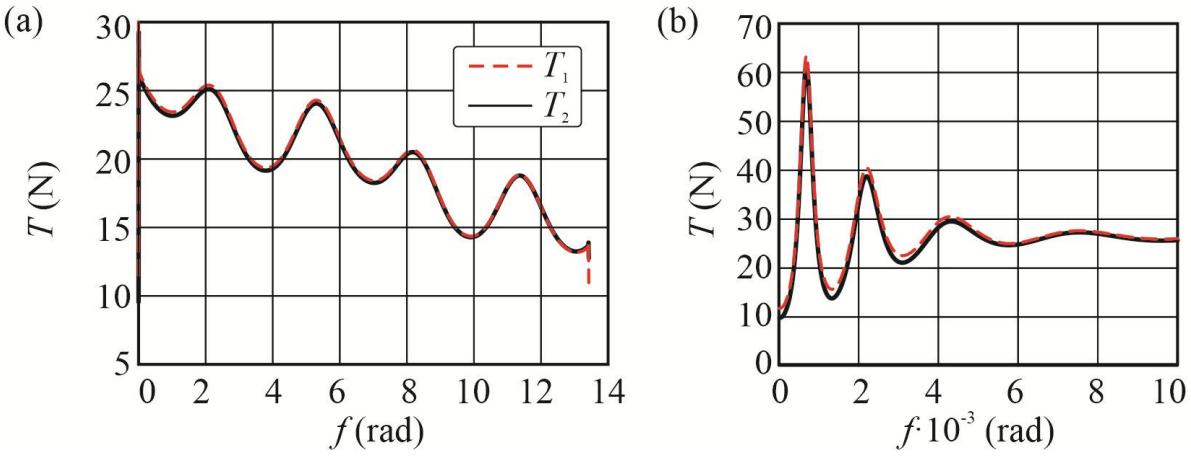

Figure 3.35. The tethers' tension forces T_1, T_2 during the climber's descent with initial conditions (3.20).

Numerical simulation of the hovering lunar space elevator

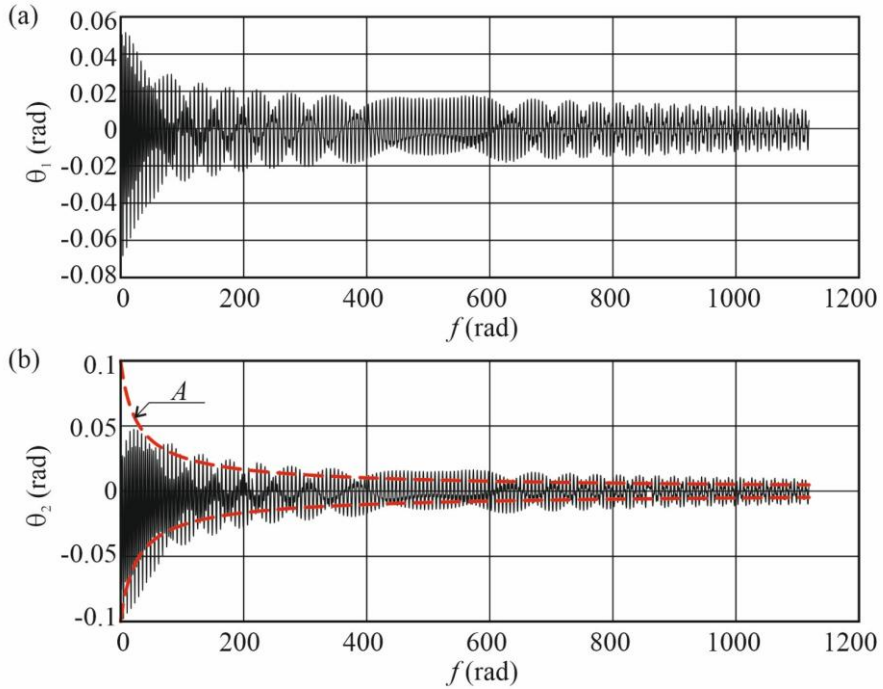

Figure 3.36. The tethers' deflection angles θ_1, θ_2 during the end-mass ascent.

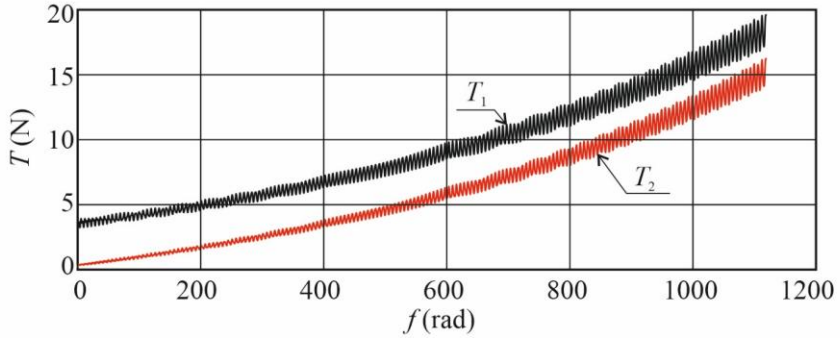

Figure 3.37. The tethers' tension forces T_1, T_2 during the end-mass ascent.

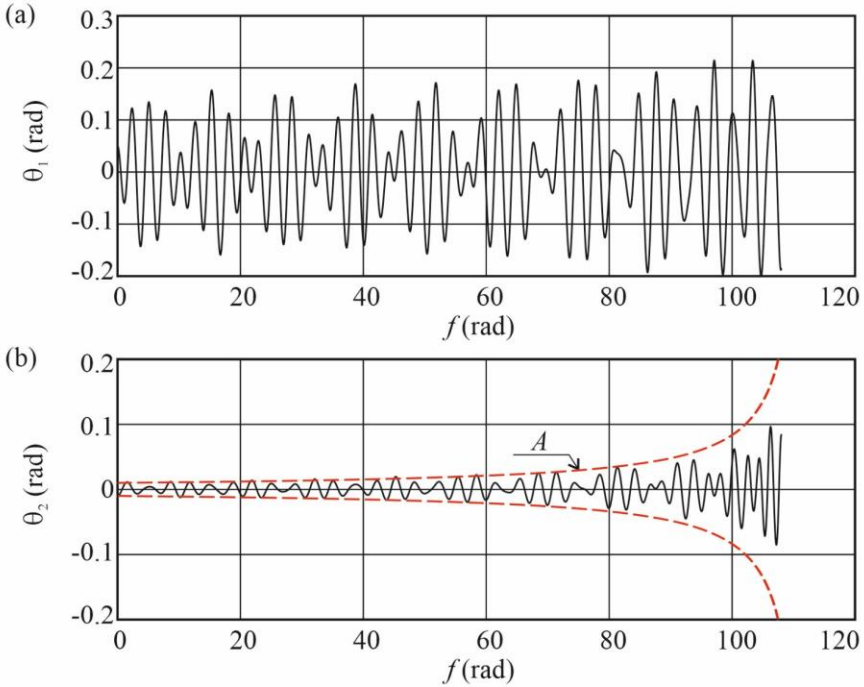

Figure 3.38. The tethers' deflection angles θ_1, θ_2 during the end-mass descent.

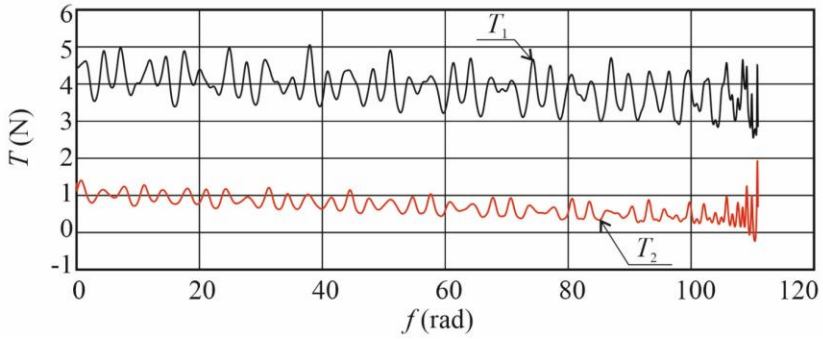

Figure 3.39. The tethers' tension forces T_1, T_2 during the end-mass descent.

Numerical simulation of the hovering lunar space elevator

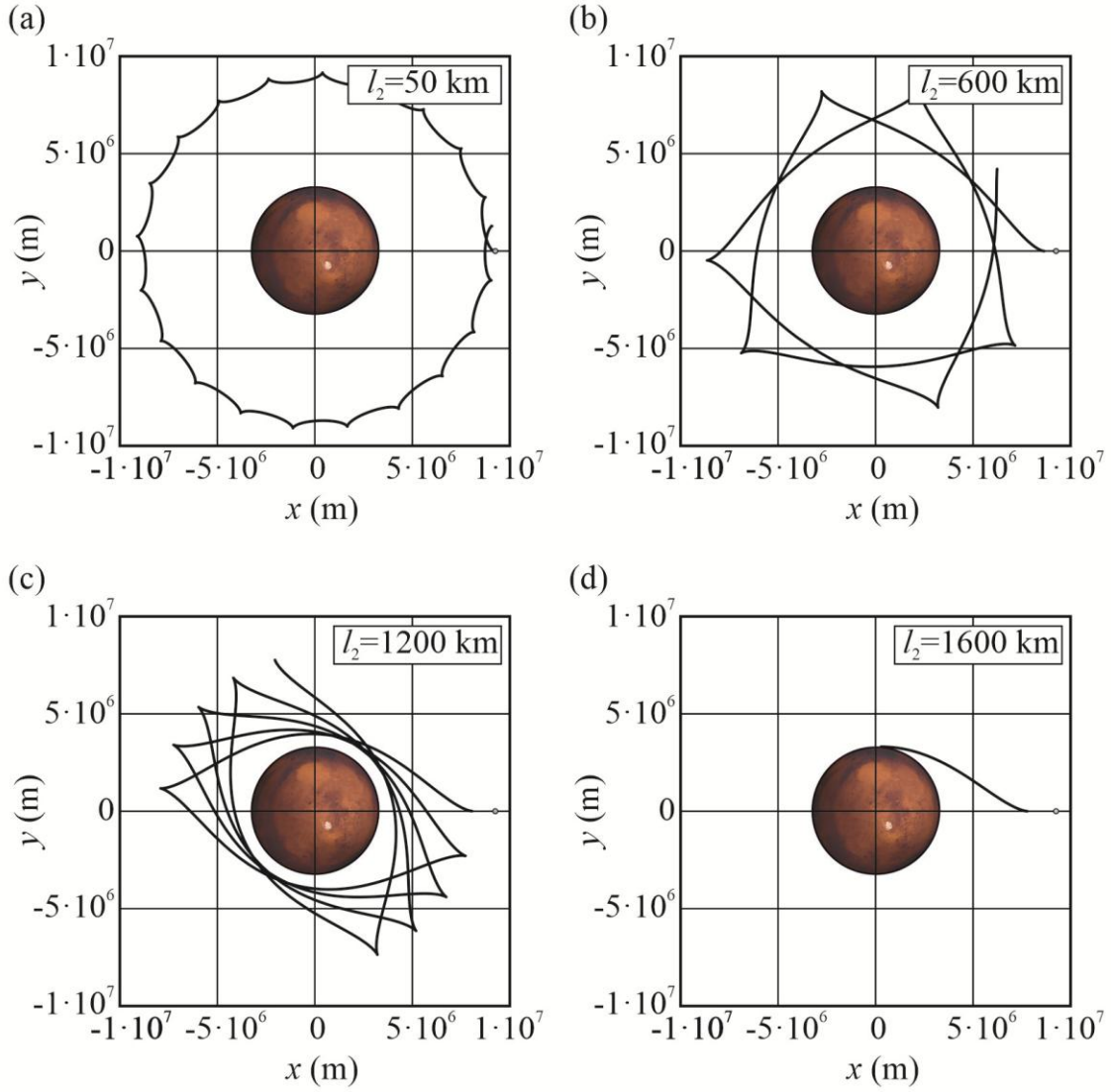

Figure 3.40.Trajectories of the probe's motion in the rotating Oxy coordinate system after separation from the tether at different altitudes.

Chapter 4

A Splitting of Libration Points by an Artificial Electrostatic Field

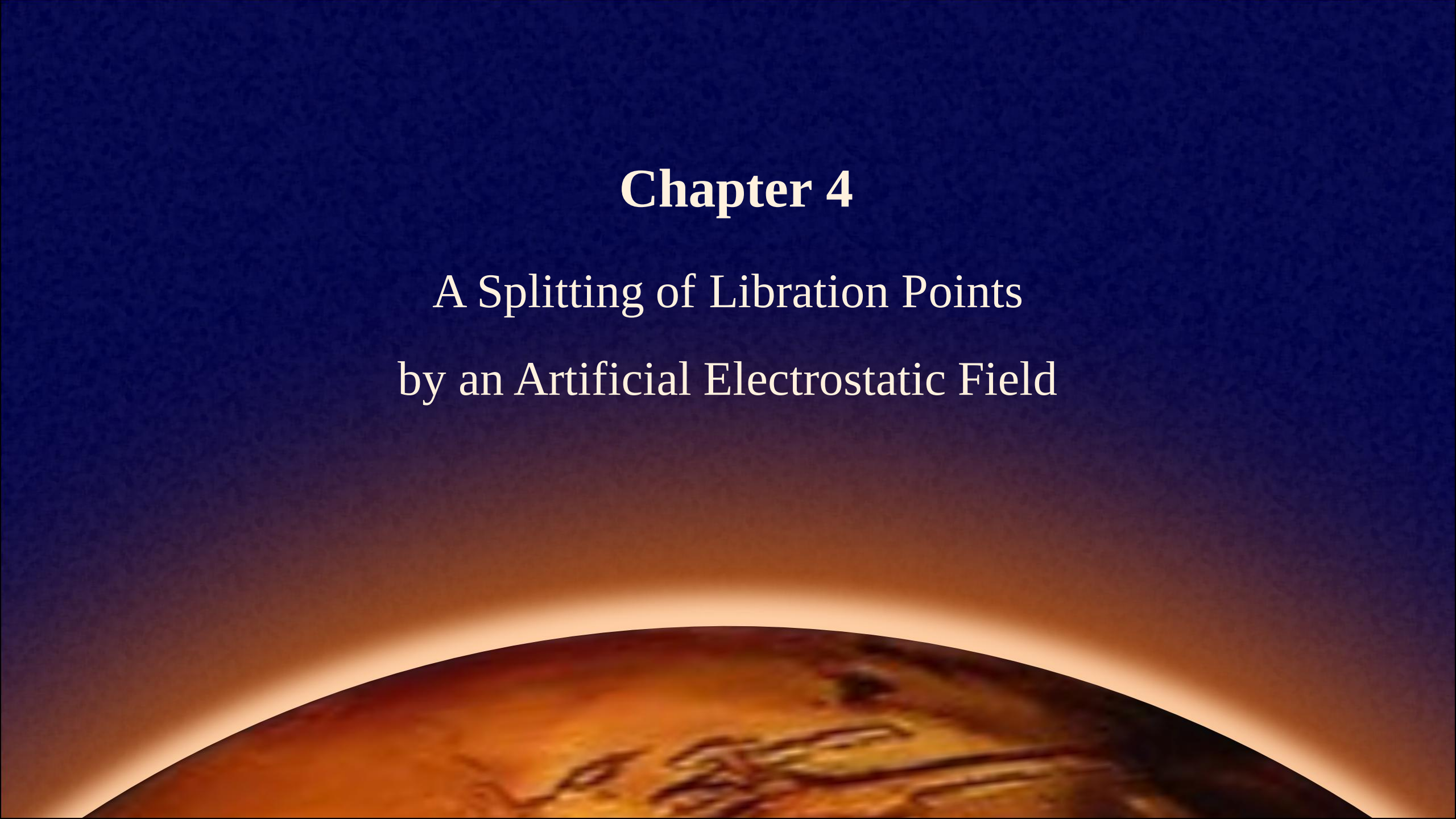

4.1. A splitting of collinear libration points in circular restricted three-body problem by an artificial electrostatic field

Equations of motion of a space tether system at quasi-satellite orbit

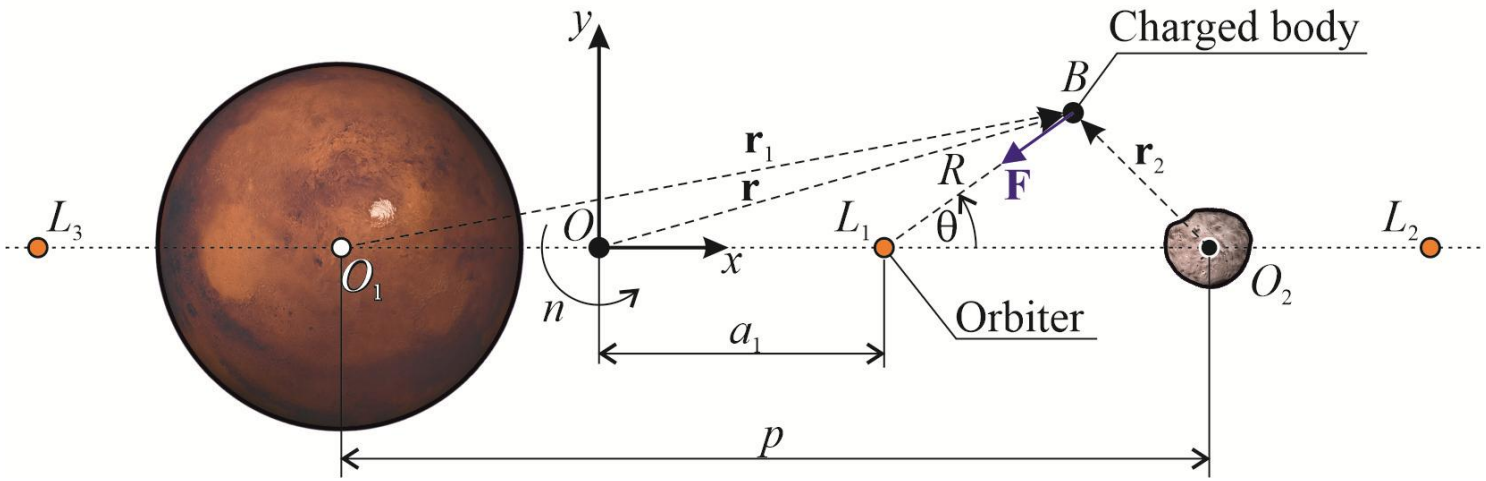

Figure 4.1. The mechanical system.

$$x'' - 2y' = \frac{\partial U}{\partial x}$$
$$y'' + 2x' = \frac{\partial U}{\partial y} \qquad (4.1)$$

- $U(x,y) = \frac{1}{2}(x^2 + y^2) + \frac{1-\mu}{\rho_1} + \frac{\mu}{\rho_2} - k\frac{\bar{\Phi}}{\rho}$ (4.2)
- $J(x,y) = (x^2 + y^2) + \frac{2(1-\mu)}{\rho_1} + \frac{2\mu}{\rho_2} - 2k\frac{\bar{\Phi}}{\rho} - (x'^2 + y'^2)$ (4.3)

- $\tau = nt$
- $\bar{\Phi} = \frac{\Phi}{mp^3n^2} < 0$
- $\Phi = k_C q_o q_b$
- the prime denotes the derivative with respect to the new independent variable

Equations of motion of a space tether system at quasi-satellite orbit

$$x' = y' = 0$$
$$x'' = y'' = 0 \qquad (4.4)$$

$$L_{i-}: \quad 0 = x - \frac{1-\mu}{(\mu+x)^2} + \frac{\mu}{(x-1+\mu)^2} - \frac{\bar{\Phi}}{(x-\bar{a})^2}\,\mathrm{sign}(\bar{a})$$
$$L_{i+}: \quad 0 = x - \frac{1-\mu}{(\mu+x)^2} + \frac{\mu}{(x-1+\mu)^2} + \frac{\bar{\Phi}}{(x-\bar{a})^2}\,\mathrm{sign}(\bar{a}) \qquad (4.5)$$

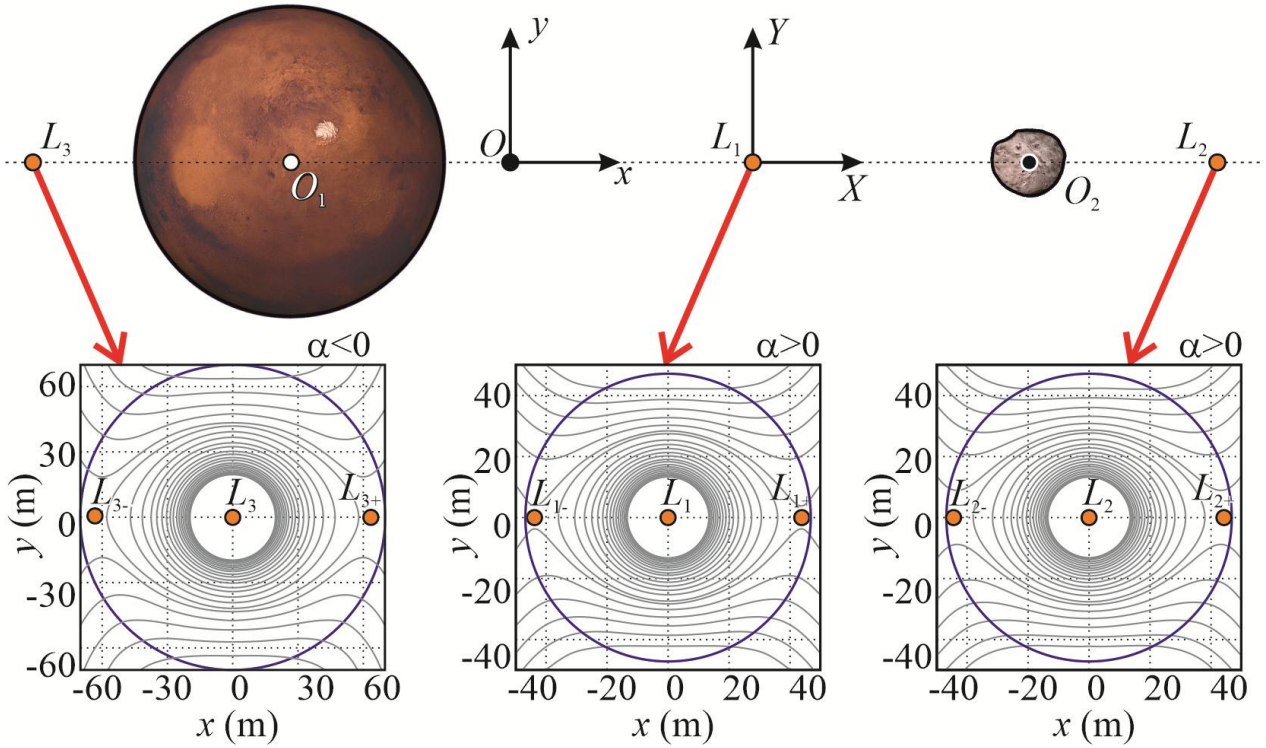

Figure 4.2. Splitting the collinear libration points.

Libration Points Stability

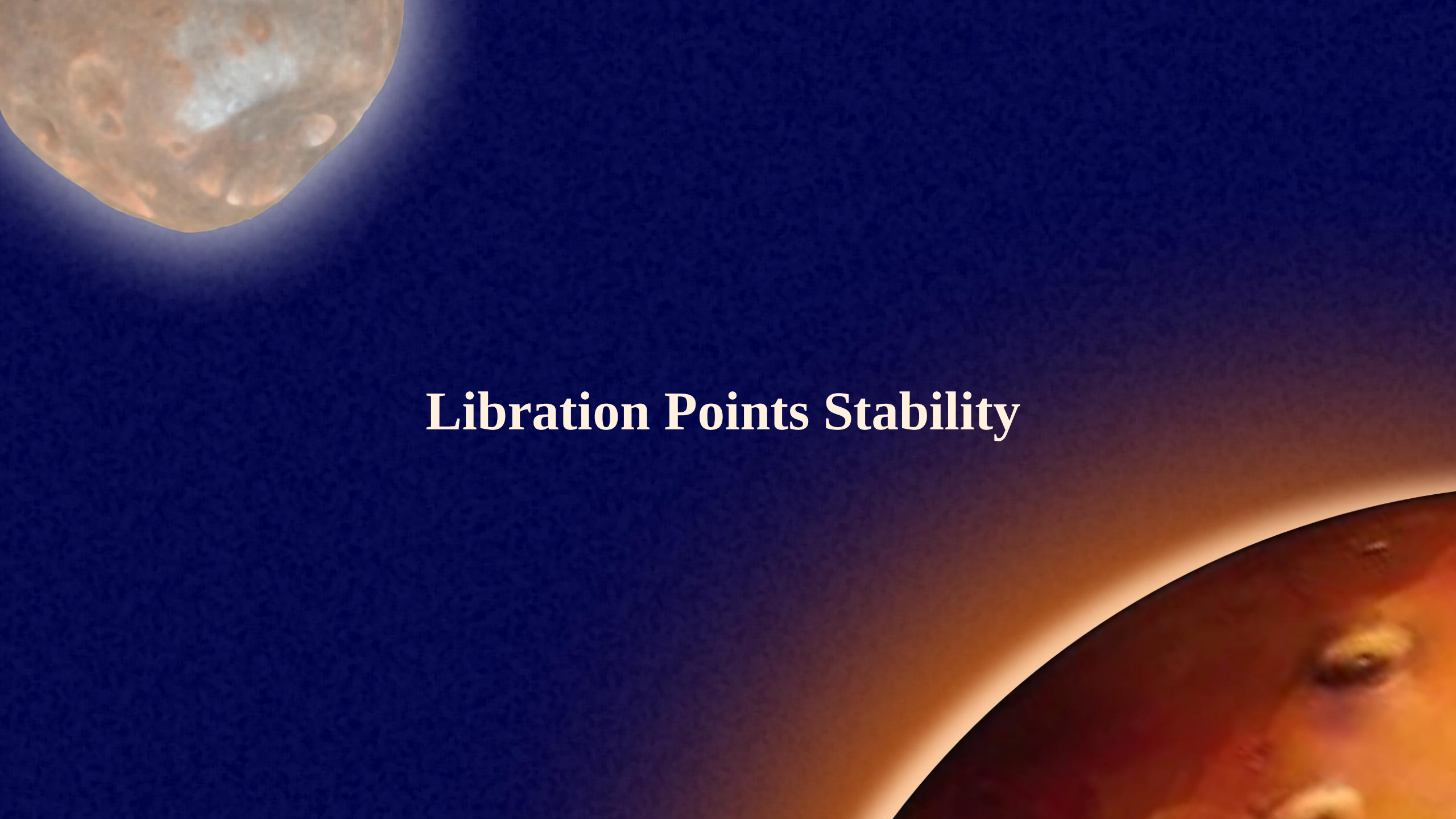

Numerical study of the electrostatic charge level influence on the trajectory of a charged body

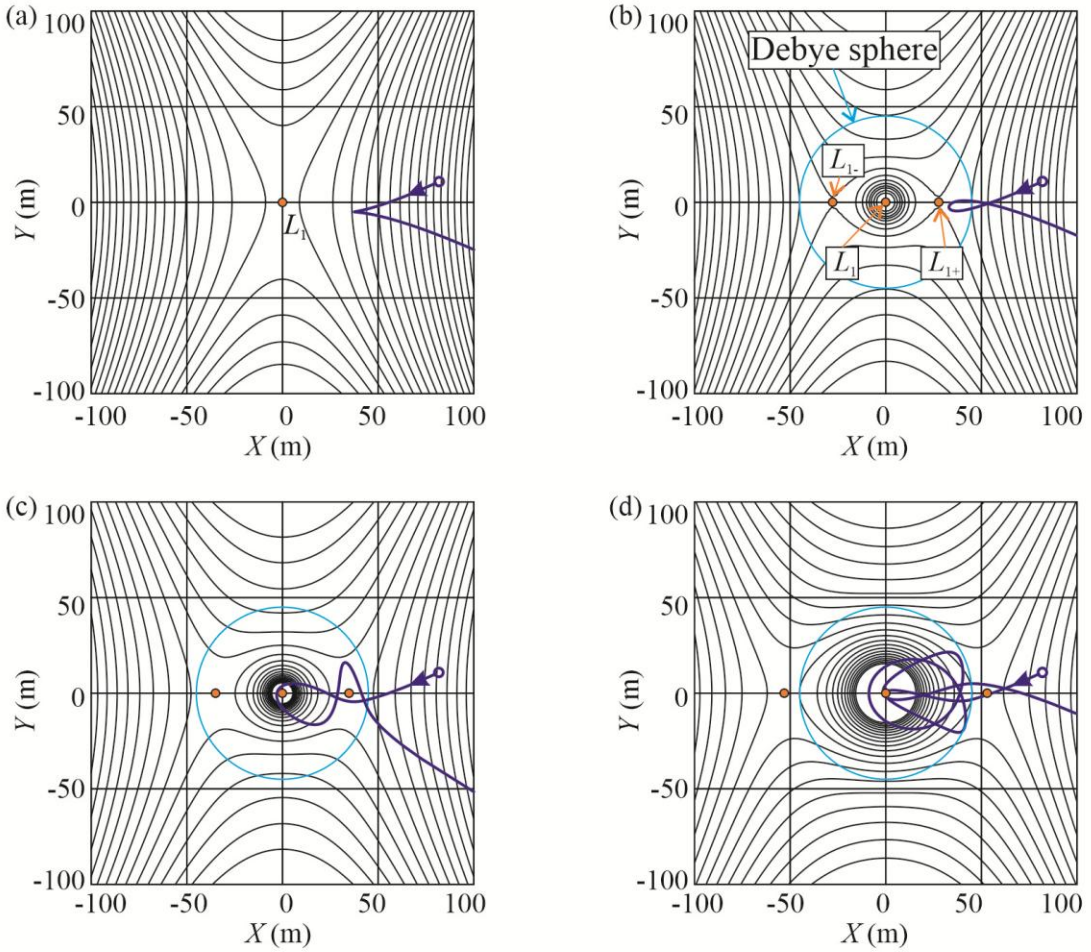

Figure 4.3. Trajectories of a charged capsule near the L_1 libration point at different charge levels:

a) $\Phi = 0$ b) $\Phi = -0.1\ \mathrm{N \cdot m^2}$ $\Phi = -0.2\ \mathrm{N \cdot m^2}$ $\Phi = -0.7\ \mathrm{N \cdot m^2}$

4.2. Prospects of Phobos sample return mission using electrostatic container

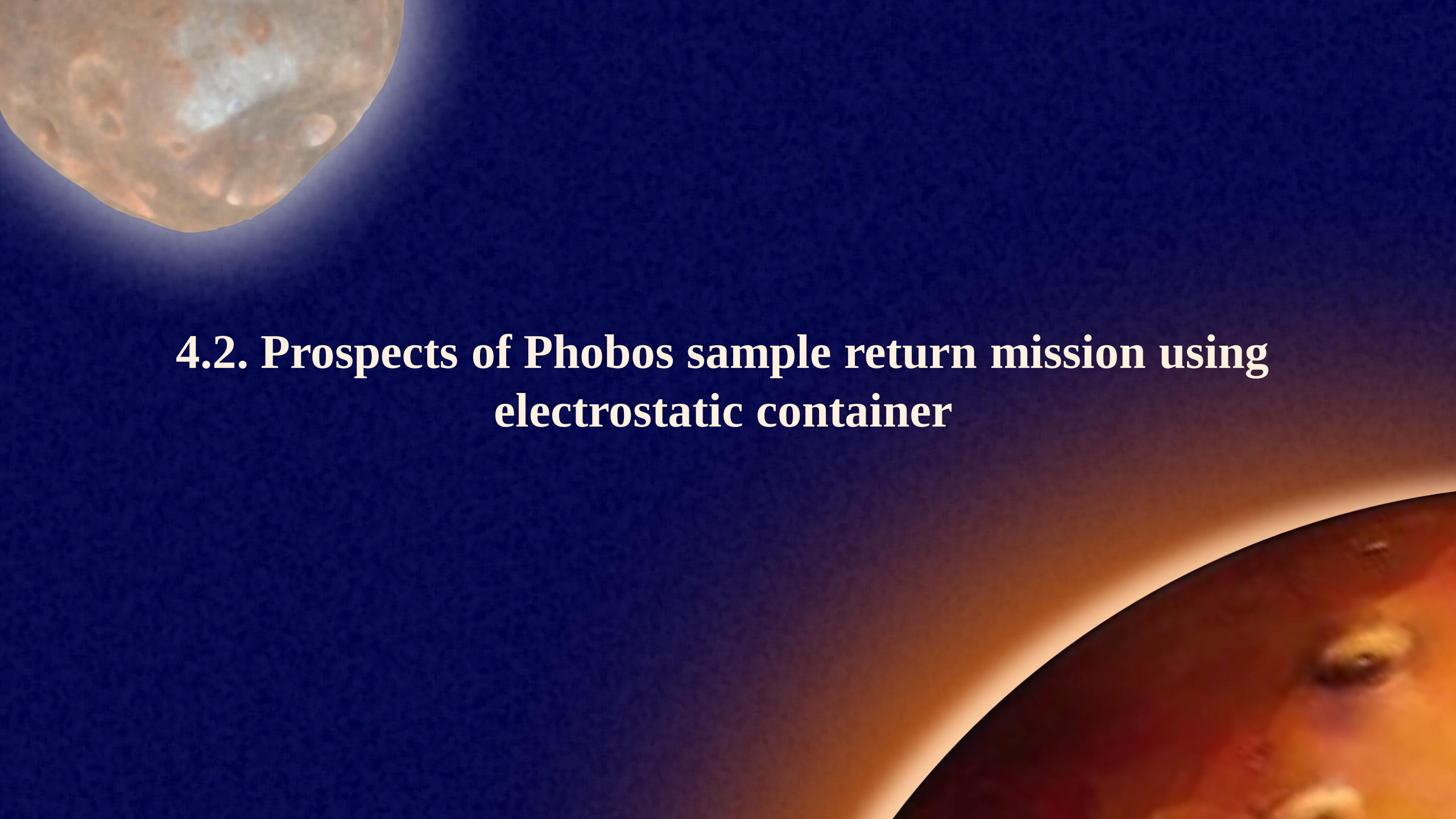

Problem formulation

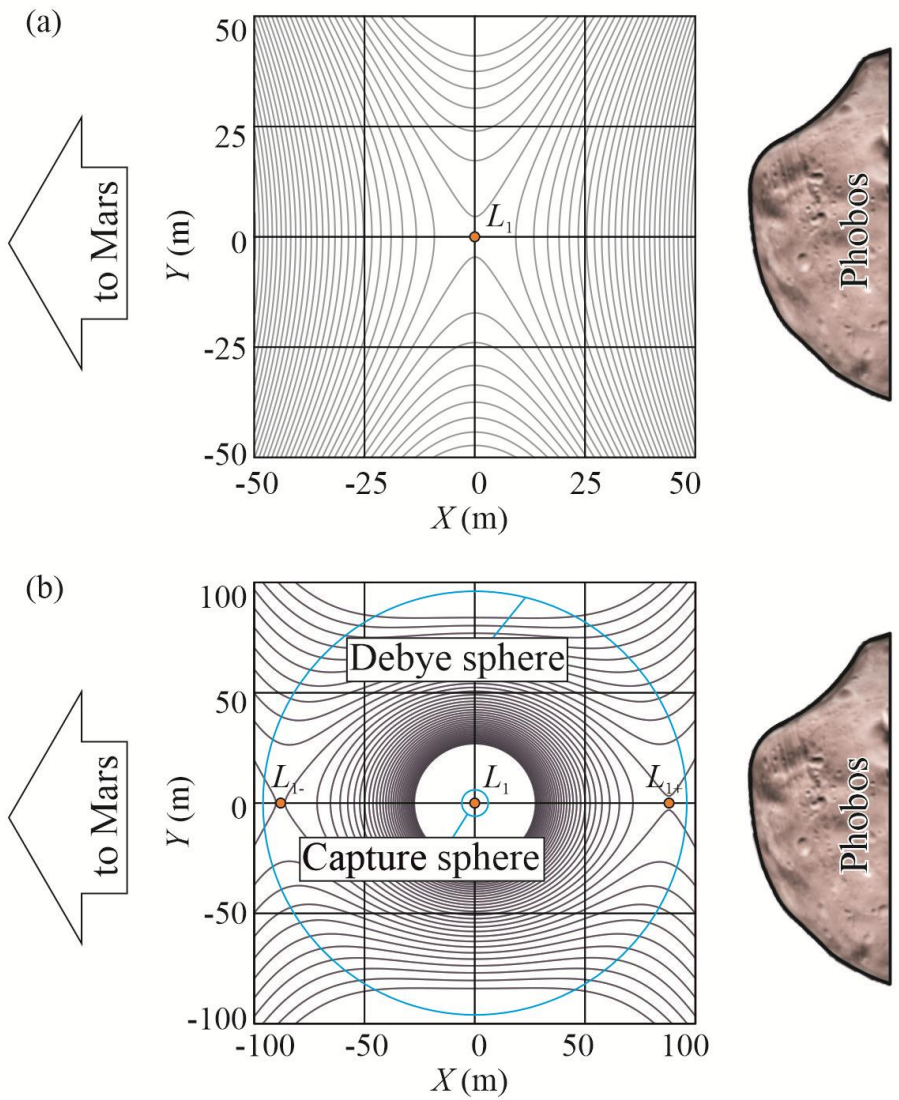

Figure 4.4. Splitting of the unstable Mars–Phobos L_1 libration point.

Restricted three-body problem with E-field influence

$$\left(\frac{\partial W_*}{\partial X}\right)_{Y=0} = 0$$

$$W_*(X,Y) = G\left(\frac{M_1}{\sqrt{(X+a_1+p\mu)^2+Y^2}} + \frac{M_2}{\sqrt{(X+a_1-p(1-\mu))^2+Y^2}}\right) - \frac{k\Phi}{m\sqrt{X^2+Y^2}} + \frac{n^2((X+a_1)^2+Y^2)}{2} \qquad (4.6)$$

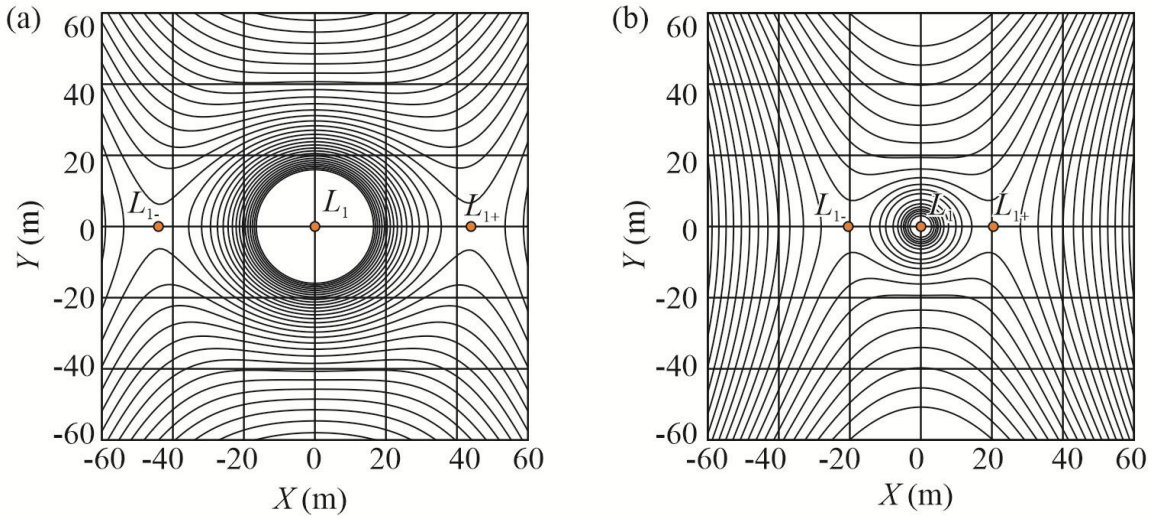

Figure 4.5. Contour plot of the effective potential in the vicinity of the L_1 point for a) $\Phi = -0.4\ \mathrm{N\cdot m^2}$ b) $\Phi = -0.04\ \mathrm{N\cdot m^2}$

Determination of the container's trajectory

$$\dot{X} = -X' \quad \dot{Y} = -Y' \quad \ddot{X} = X'' \quad \ddot{Y} = Y'' \qquad (4.7)$$

$$X'' = \frac{\partial W_E}{\partial X} + n^2(X + a_1) - 2nY'$$

$$Y'' = \frac{\partial W_E}{\partial Y} + n^2 Y + 2nX' \qquad (4.8)$$

$$J_E^* = \frac{2GM_1}{\sqrt{(X_L + a_1 - p(1-\mu))^2 + Y_L^2}} + \frac{2GM_2}{\sqrt{(X_L + a_1 + p\mu)^2 + Y_L^2}} +$$

$$n^2((X_L + a_1)^2 + Y_L^2) - \frac{2\Phi}{m\sqrt{X_L^2 + Y_L^2}}$$

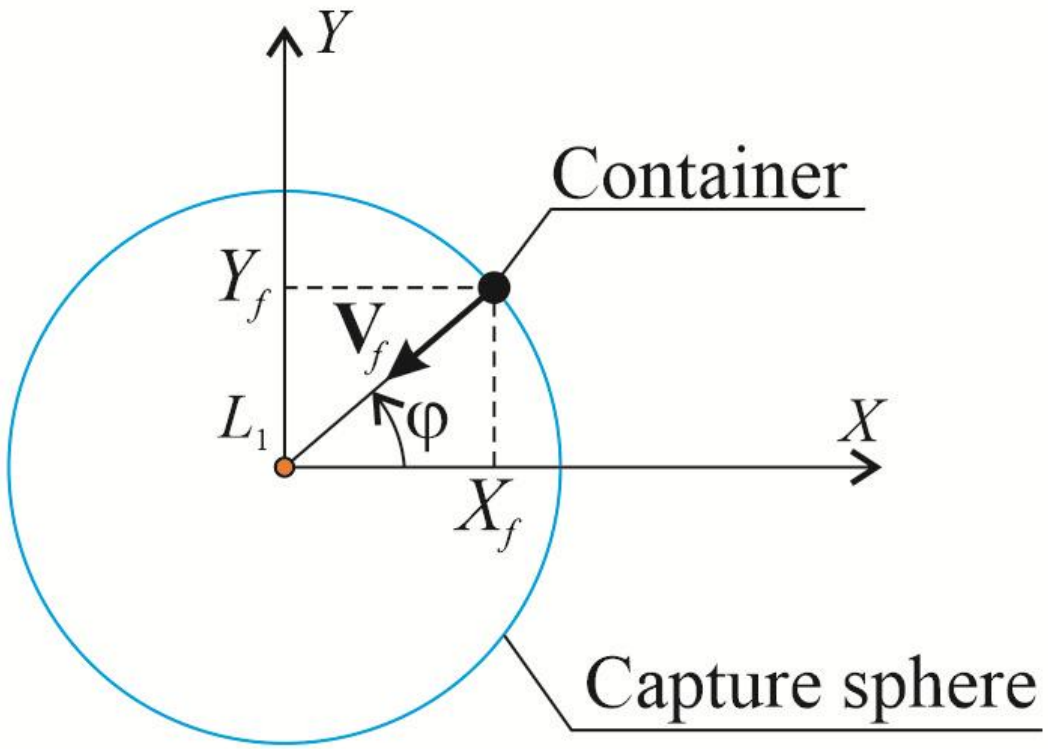

Figure 4.6. The Capture Sphere.

Determination of the container's trajectory

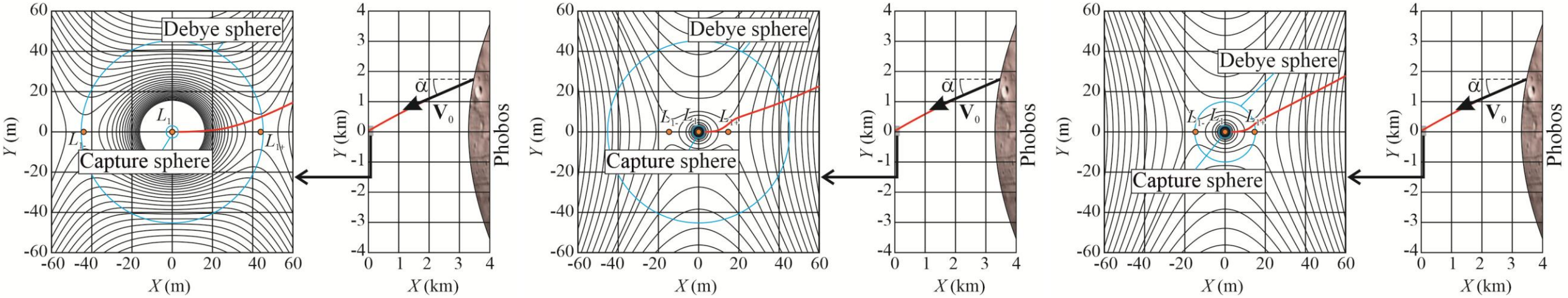

Figure 4.7. The container trajectory for different parameters and initial conditionals.

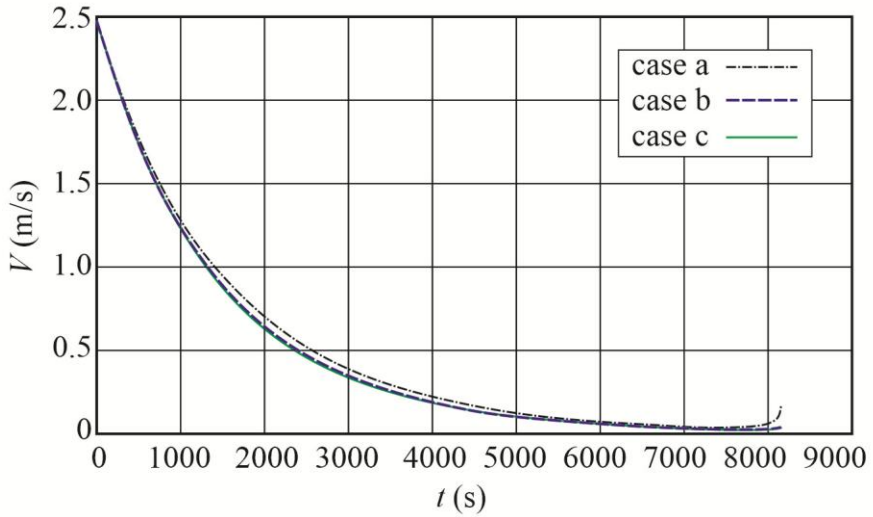

Figure 4.8. The container trajectory for different parameters and initial conditionals.

4.3. Capture trajectories into vicinity of collinear libration points by variable electrostatic field

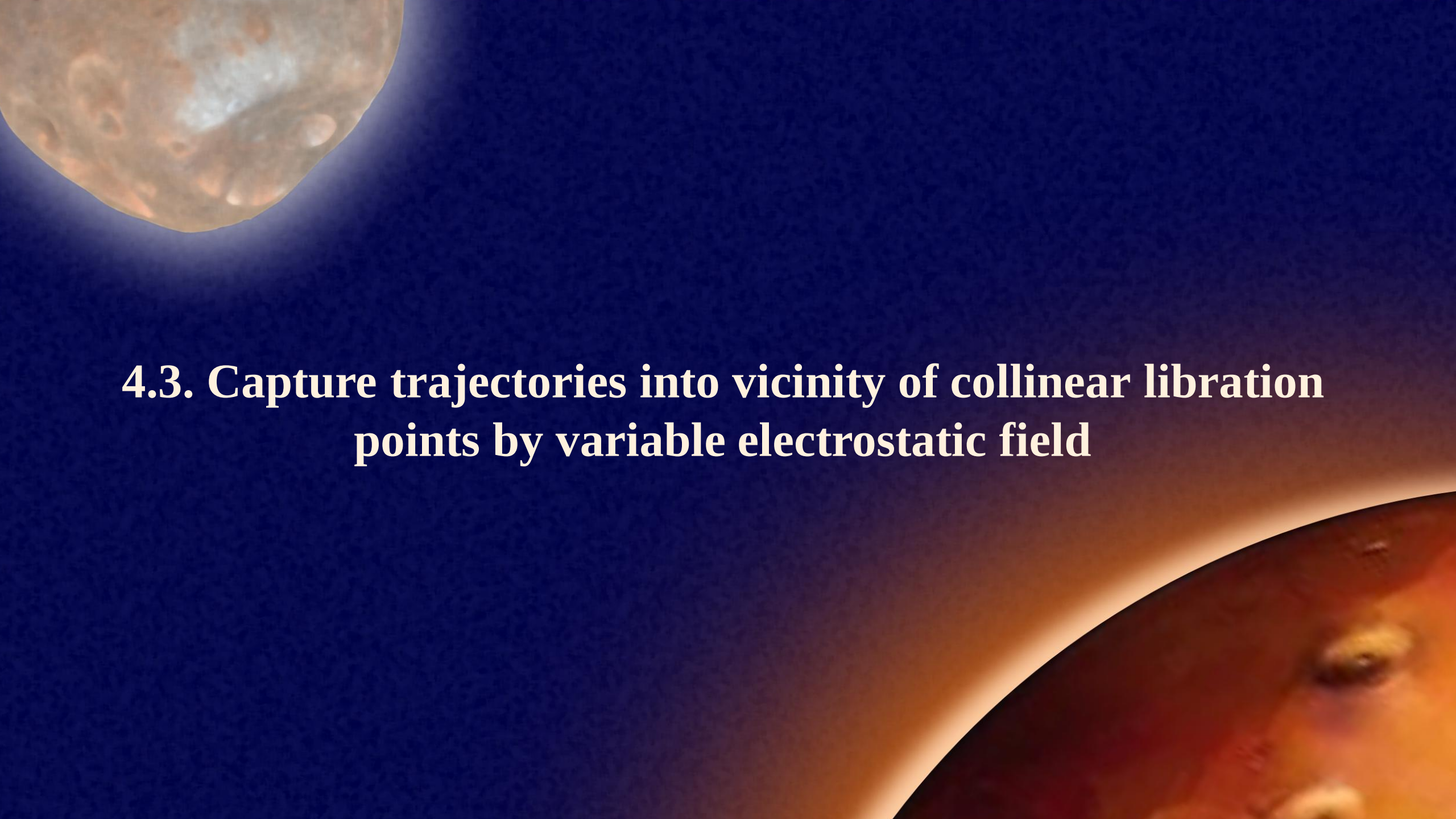

$$\ddot{R} = \frac{\partial W(R,\theta)}{\partial R} + R\left(n+\dot{\theta}\right)^2$$
$$\ddot{\theta} = \frac{\partial W(R,\theta)}{\partial \theta} - 2\frac{\dot{R}}{R}\left(n+\dot{\theta}\right) \qquad (4.9)$$

- $W(R,\theta) = G\left(\frac{M_1}{r_1} + \frac{M_2}{r_2}\right) - \frac{\Phi}{mR} + \frac{1}{2}(nr)^2$ (4.10)

The orbiter charge control law

$$q_o = q_{o0}\left(1+\varepsilon\frac{\dot{R}}{Rn}\right) \qquad (4.11)$$

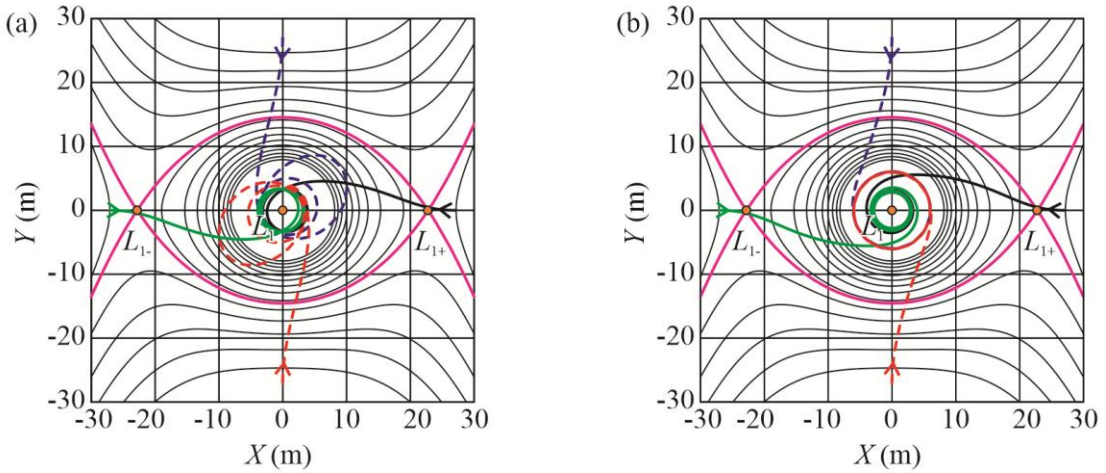

Figure 4.9. Trajectories of a charged body near the L_1 libration point for a) $\varepsilon = 0.01$ b) $\varepsilon = 0.1$.

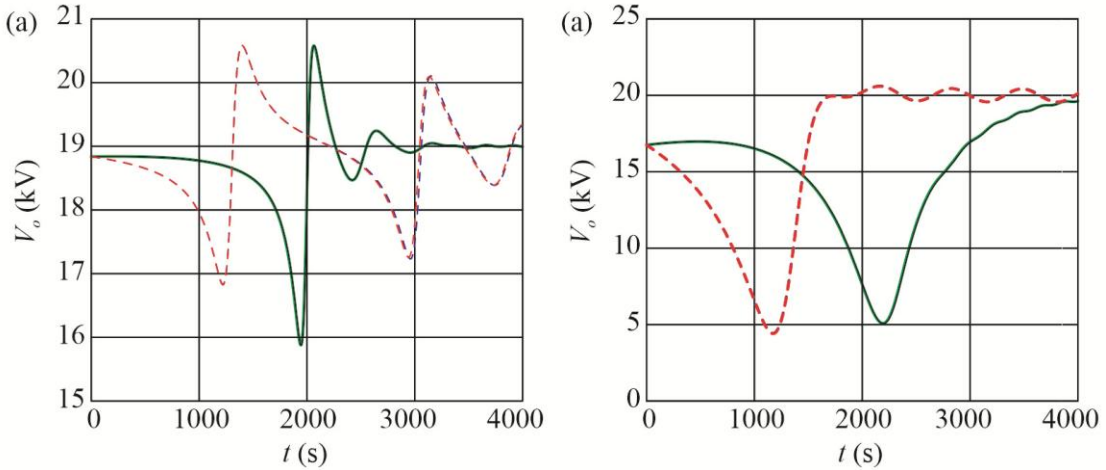

Figure 4.10. The orbiter voltages for the four controlled trajectories of the charged body for a) $\varepsilon = 0.01$ b) $\varepsilon = 0.1$.

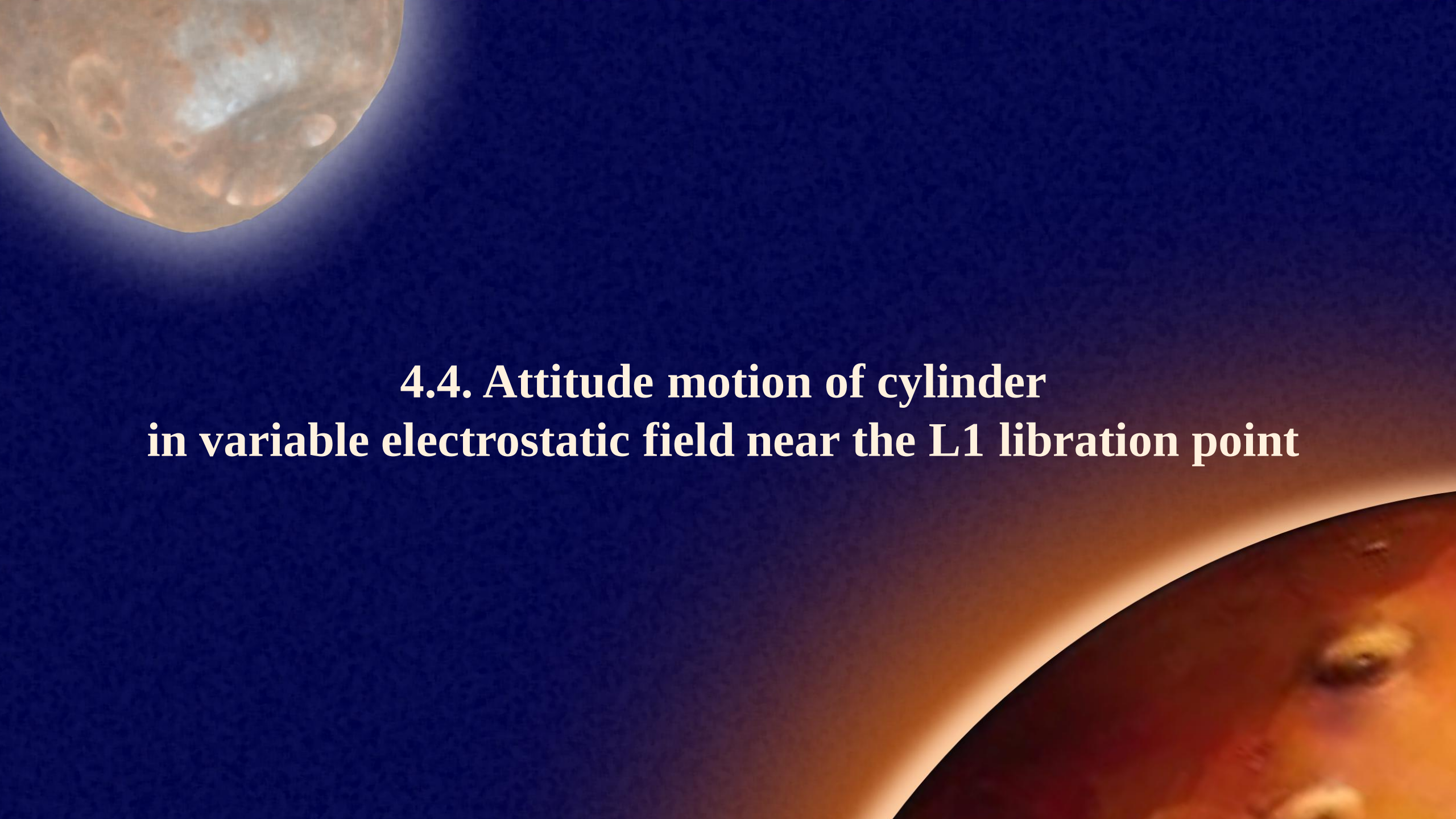

4.4. Attitude motion of cylinder in variable electrostatic field near the L1 libration point

Assumptions and reference frames

$$J_x, J_y, J_z = J_x \quad (4.12) \qquad h \ll R \quad (4.13)$$

- h is the height of the cylinder
- R is the distance between the libration point and the body's center of mass

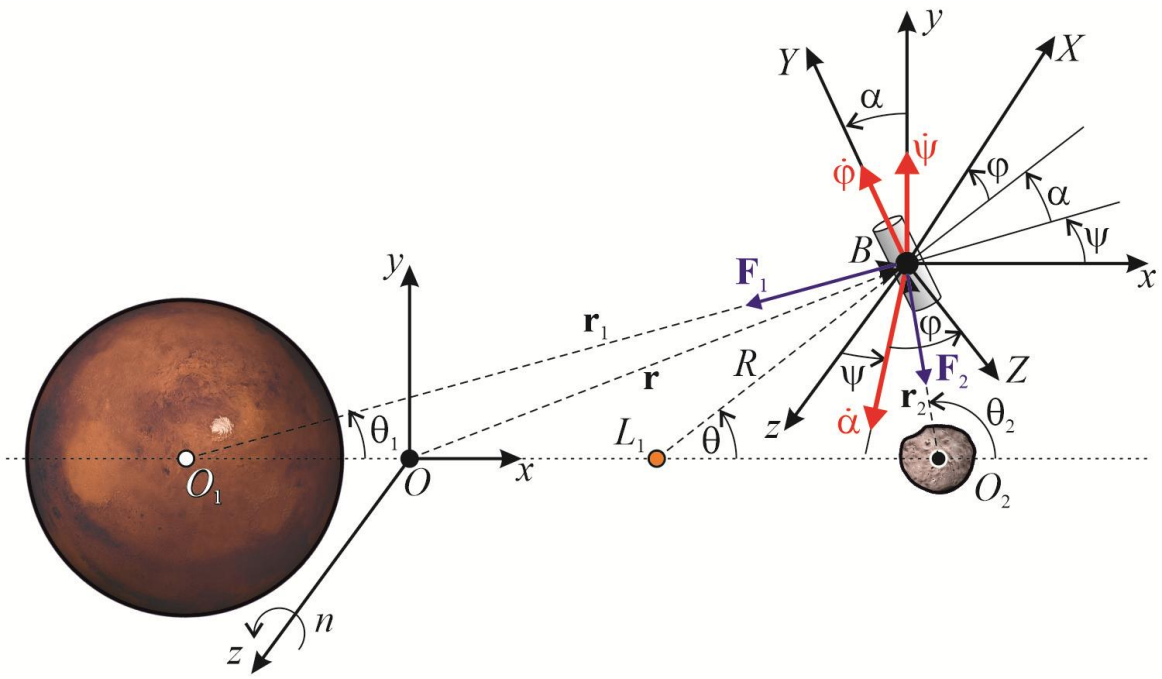

Figure 4.11. Reference frames and Euler angles.

Equations of planar motion for the center of mass of a charged body

$$\ddot{R} = \frac{\partial U}{\partial R} + R(n+\dot{\theta})^2 - \frac{F_Q}{m}, \qquad \ddot{\theta} = \frac{\partial U}{\partial \theta} - 2\frac{\dot{R}}{R}(n+\dot{\theta}) \tag{4.14}$$

- $$F_Q = -\frac{7lR_oV_{o0}(1+\varepsilon\frac{\dot{R}}{nR})(RV_b + R_oV_{o0}(1+\varepsilon\frac{\dot{R}}{nR}))}{4k_CR^3} \tag{4.15}$$

- $$U = G(\frac{M_1}{r_1} + \frac{M_2}{r_2}) + \frac{1}{2}(nr)^2 \tag{4.16}$$

Equations of attitude motion for a charged cylindrical body

$$J_x\ddot{\psi} = (J_x - J_y)\left[\frac{3GM_1}{r_1^5}(c_1 + R\cos\theta)(c_1\cos\psi + R(\cos\theta\cos\psi - \cot\alpha\sin\theta))\sin\psi + \right.$$
$$\frac{3GM_2}{r_2^5}(-c_2 + R\cos\theta)(-c_2\cos\psi + R(\cos\theta\cos\psi - \cot\alpha\sin\theta))\sin\psi -$$
$$\left. n^2\sin\psi\cos\psi\right] + \dot{\alpha}(J_y\Omega - 2J_x\dot{\psi}\cos\alpha)\csc\alpha - \frac{k_Q\cos\theta\csc\alpha\sin\psi}{R^2}$$

$$J_x\ddot{\alpha} = (J_x - J_y)\left[-\frac{3GM_1}{r_1^5}(c_1\sin\alpha\cos\psi + R(-\sin\theta\cos\alpha + \cos\theta\sin\alpha\cos\psi))\cdot\right.$$
$$(c_1\cos\alpha\cos\psi + R(\cos\theta\cos\alpha\cos\psi + \sin\theta\sin\alpha)) -$$
$$\frac{3GM_2}{r_2^5}(-c_2\sin\alpha\cos\psi + R(-\sin\theta\cos\alpha + \cos\theta\sin\alpha\cos\psi))\cdot$$
$$\left.(-c_2\cos\alpha\cos\psi + R(\cos\alpha\cos\theta\cos\psi + \sin\alpha\sin\theta)) - n^2\sin\alpha\cos\alpha(\sin\psi)^2\right] +$$
$$\dot{\psi}(J_x\dot{\psi}\cos\alpha - J_y\Omega)\sin\alpha + \frac{k_Q(\cos\alpha\cos\theta\cos\psi + \sin\alpha\sin\theta)}{R^2} \tag{4.17}$$

Numerical simulation of the motion of a charged cylindrical body

Point A: $R_0 = 45\,\text{m}, \quad \dot{R}_0 = -0.002\,\text{m/s}, \quad \theta_0 = 0, \quad \dot{\theta}_0 = 0$ (4.18)

Point B: $R_0 = 25\,\text{m}, \quad \dot{R}_0 = -0.002\,\text{m/s}, \quad \theta_0 = \pi/2, \quad \dot{\theta}_0 = 0$ (4.19)

$\psi_0 = 0, \quad \dot{\psi}_0 = 0, \quad \alpha_0 = \pi/2, \quad \dot{\alpha}_0 = 1\,\text{rad/s}, \quad \varphi_0 = 0, \quad \dot{\varphi}_0 = \Omega = 1\,\text{rad/s}$ (4.20)

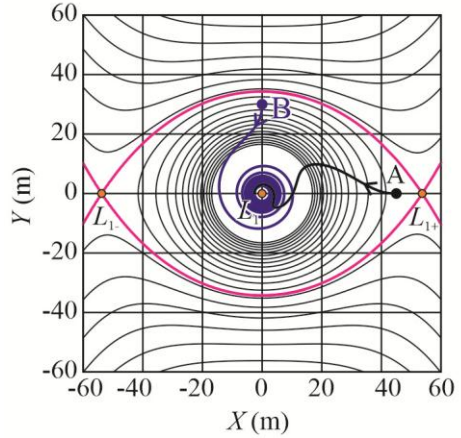

Figure 4.12. Trajectories of a charged body near the L1 libration point for initial conditions (4.18), (4.19).

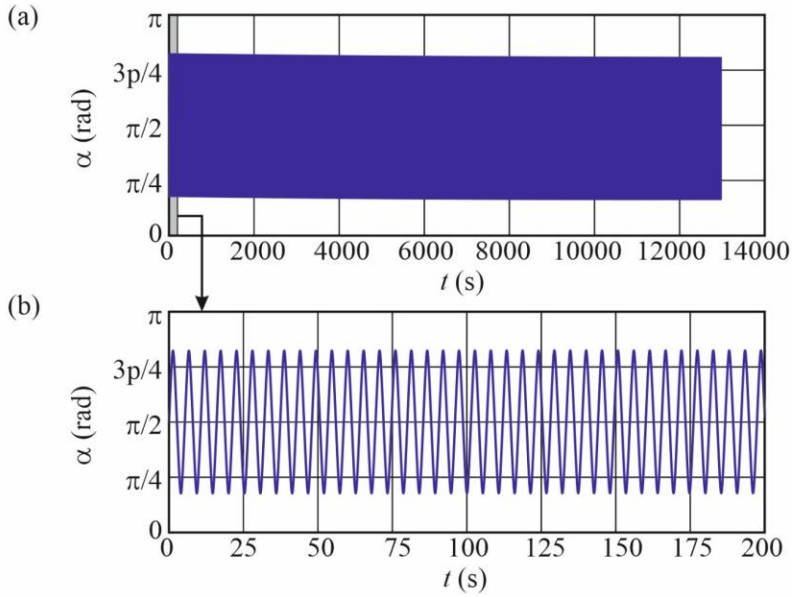

Figure 4.13. Time history of the nutation angle for initial condition (4.18).

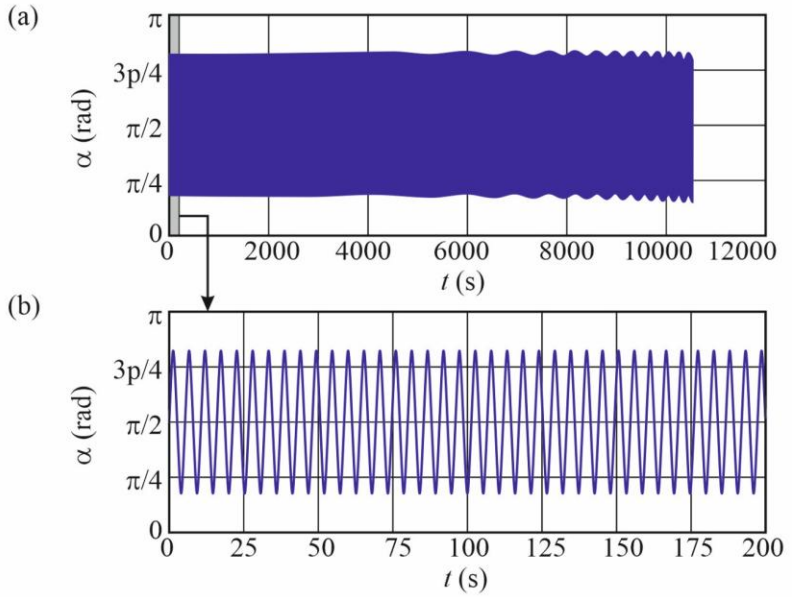

Figure 4.14. Time history of the nutation angle for initial condition (4.19).

Numerical simulation of the motion of a charged cylindrical body

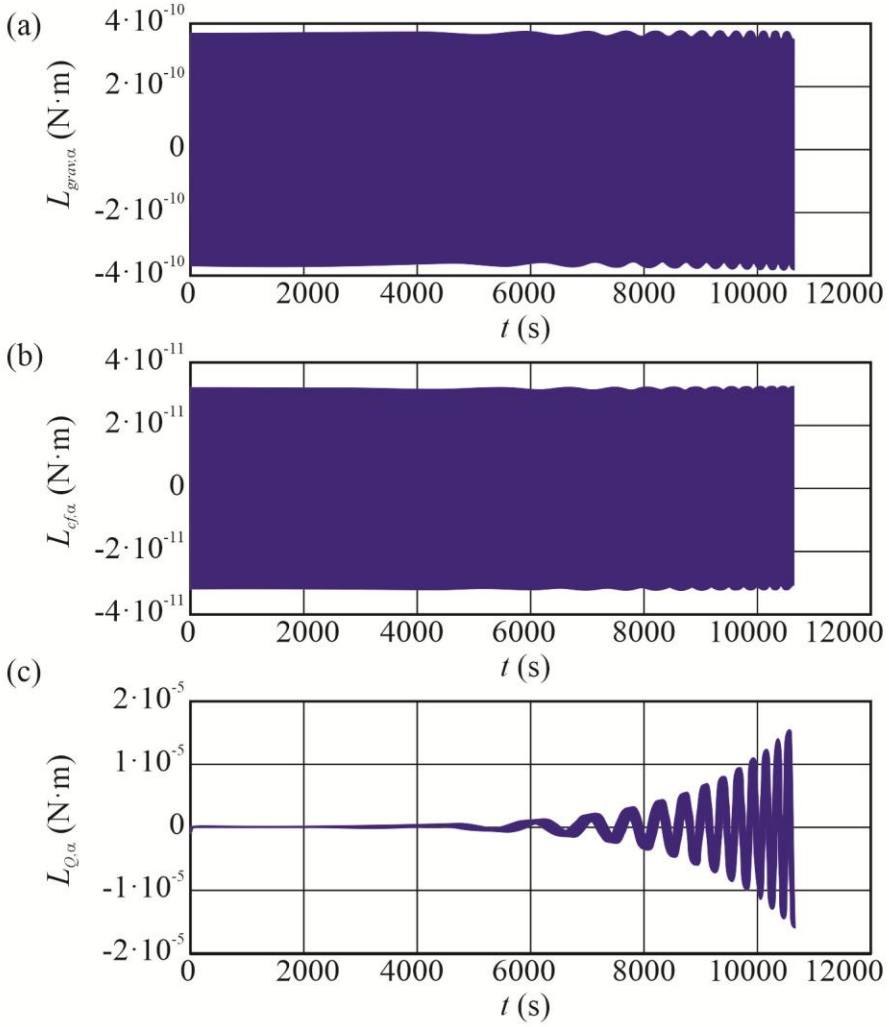

Figure 4.15. Time history of the projections of a) gravitational, b) centrifugal, and c) electrostatic torques for the initial conditions (4.19), (4.20).

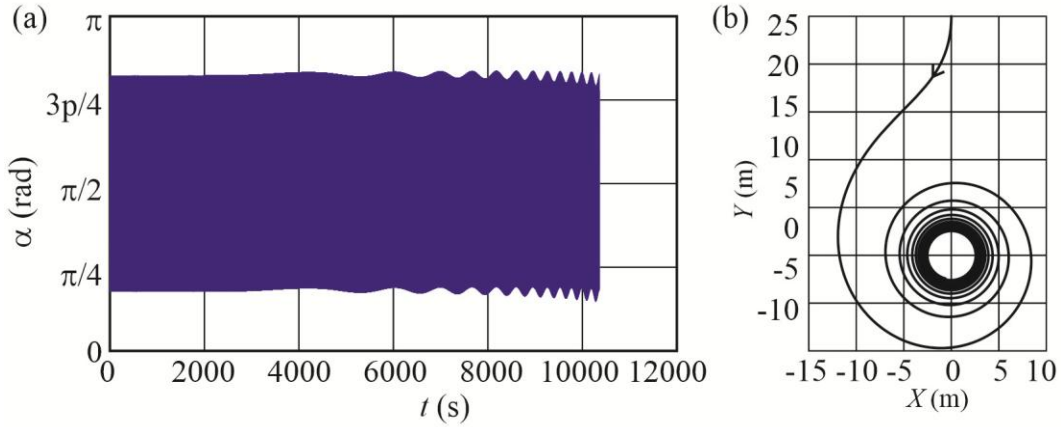

Figure 4.16. Time history of a) the nutation angle and b) the body trajectory for initial condition (4.19) and $V_b = 30\,\text{kV}$.

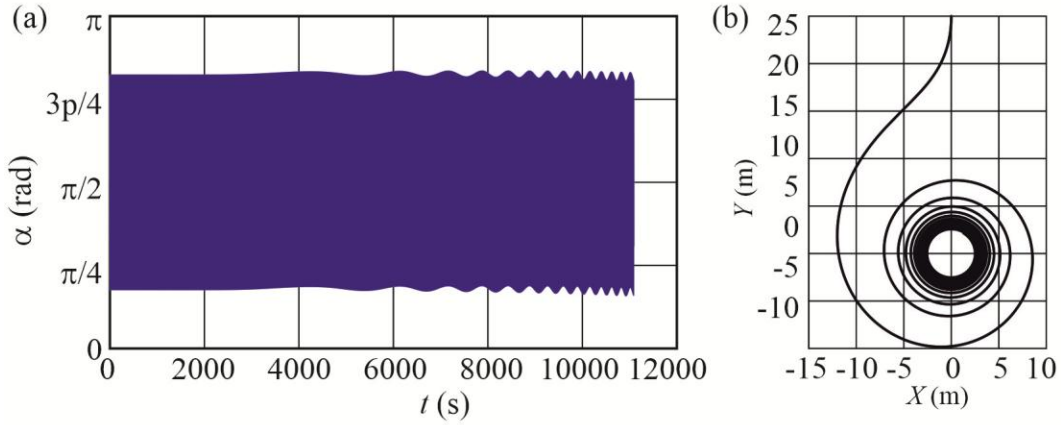

Figure 4.17. Time history of a) the nutation angle and b) the body trajectory for initial condition (4.19) and $V_b = 75\,\text{kV}$.

Numerical simulation of the motion of a charged cylindrical body

$$\psi_0 = 0, \quad \dot{\psi}_0 = 0, \quad \alpha_0 = \pi/2, \quad \dot{\alpha}_0 = 0 \text{ rad/s}, \quad \varphi_0 = 0, \quad \dot{\varphi}_0 = \Omega = 1 \text{ rad/s} \quad (4.21)$$

$$\psi_0 = 0, \quad \dot{\psi}_0 = 0, \quad \alpha_0 = \pi/2, \quad \dot{\alpha}_0 = 2 \text{ rad/s}, \quad \varphi_0 = 0, \quad \dot{\varphi}_0 = \Omega = 1 \text{ rad/s} \quad (4.22)$$

$$\psi_0 = 0, \quad \dot{\psi}_0 = 0, \quad \alpha_0 = \pi/2, \quad \dot{\alpha}_0 = 1 \text{ rad/s}, \quad \varphi_0 = 0, \quad \dot{\varphi}_0 = \Omega = 10 \text{ rad/s} \quad (4.23)$$

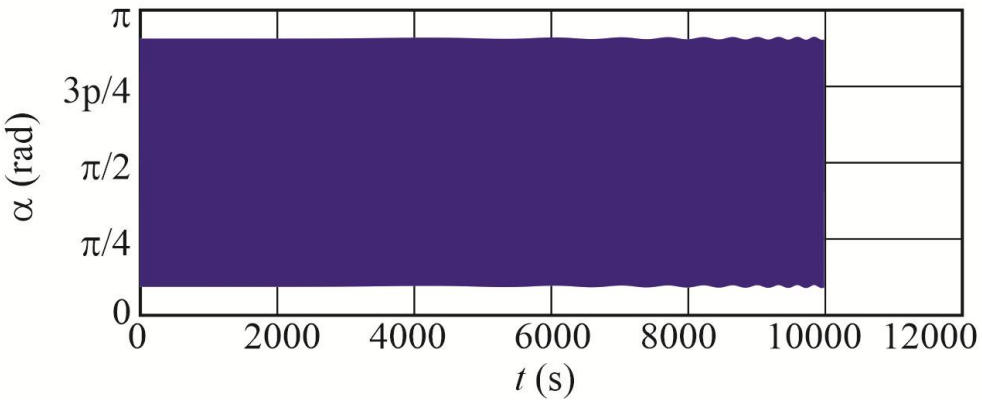

Figure 4.19. Time history of the nutation angle for initial condition (4.22).

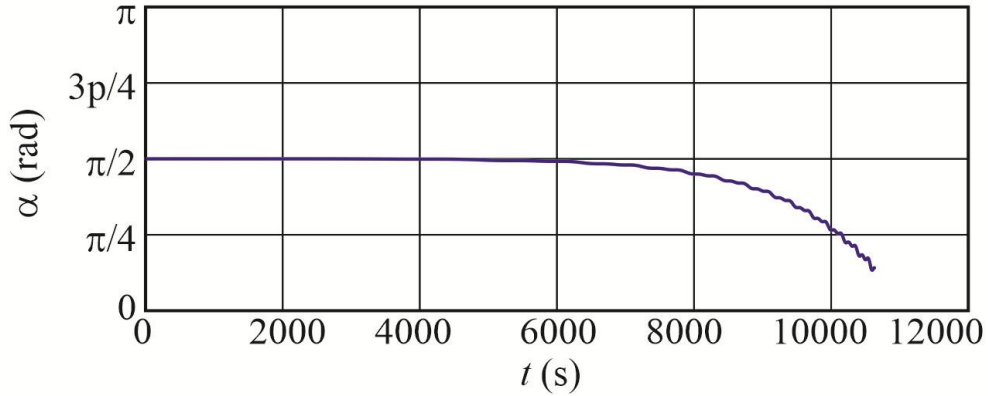

Figure 4.18. Time history of the nutation angle for initial condition (4.21).

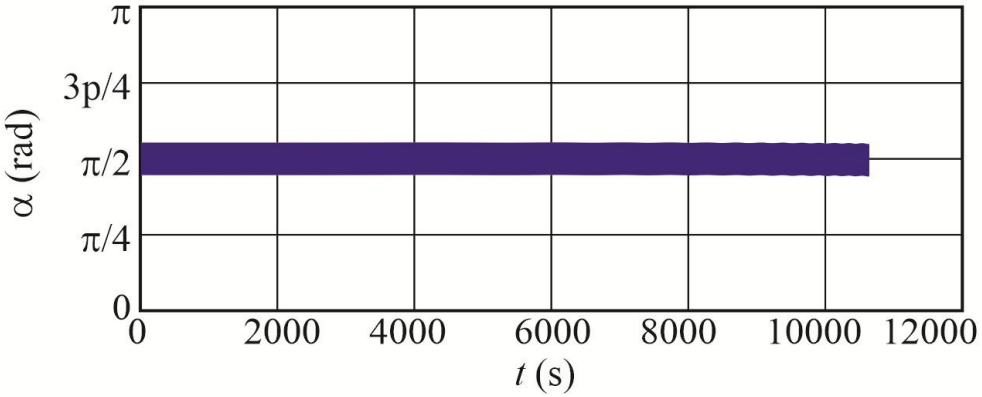

Figure 4.20. Time history of the nutation angle for initial condition (4.23).

Chapter 5

Contactless Gravitational Transportation

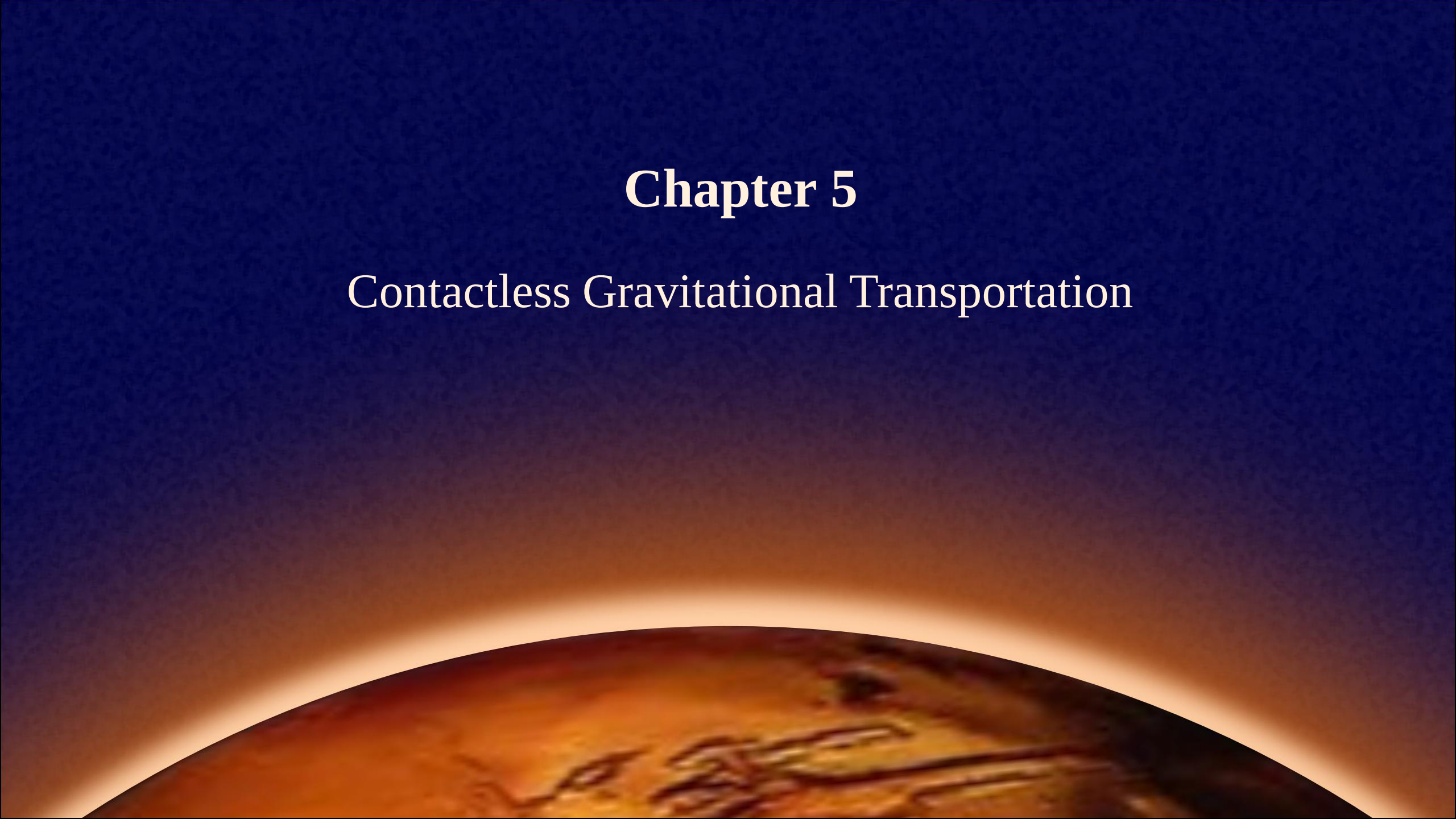

5.1. Scheme of contactless transportation of space debris by a heavy collector

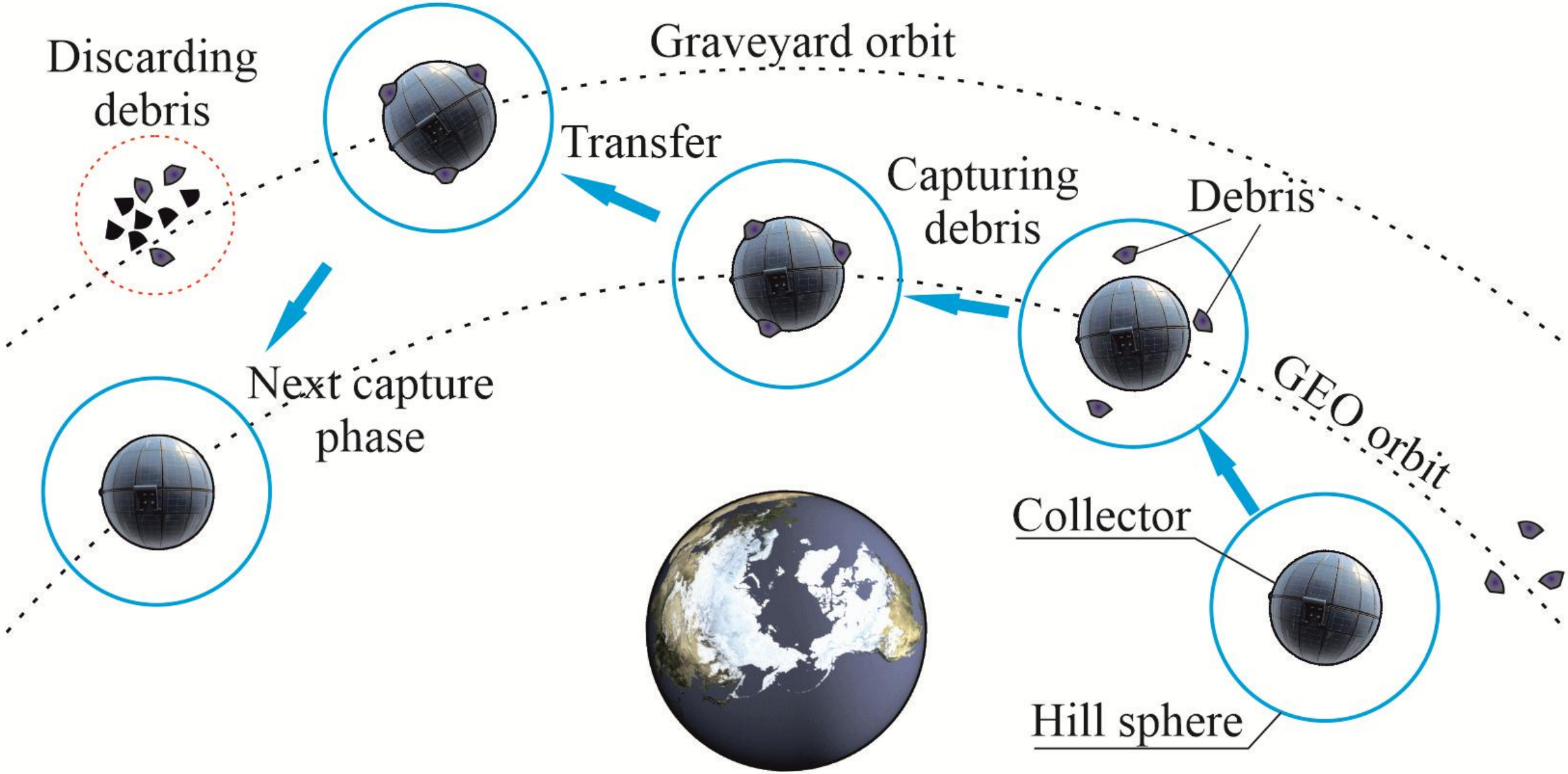

Figure 5.1. The scheme of the considered space debris removal method.

Basic idea and preliminary estimates

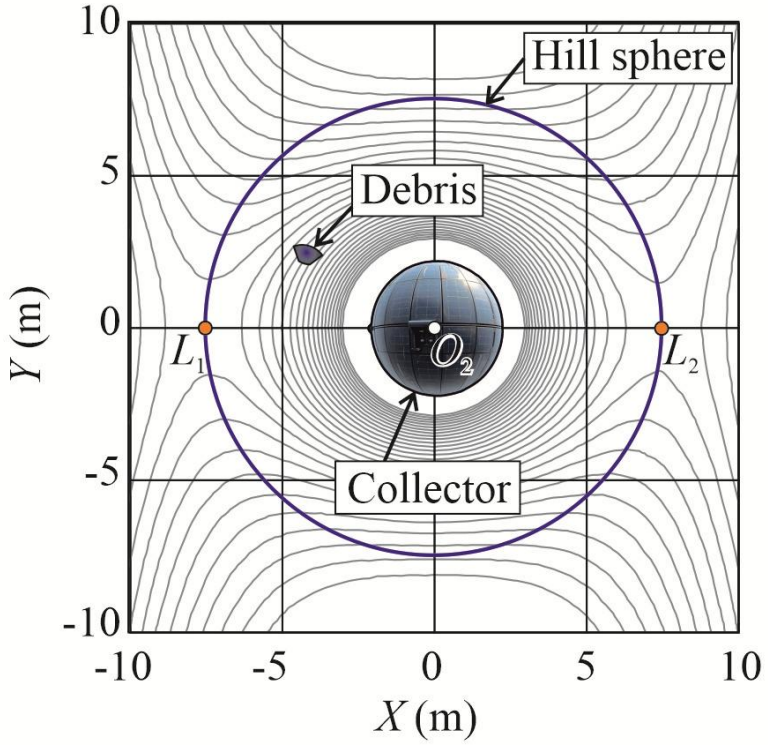

Figure 5.2. The Hill sphere for $M_2 = 10^5$ kg

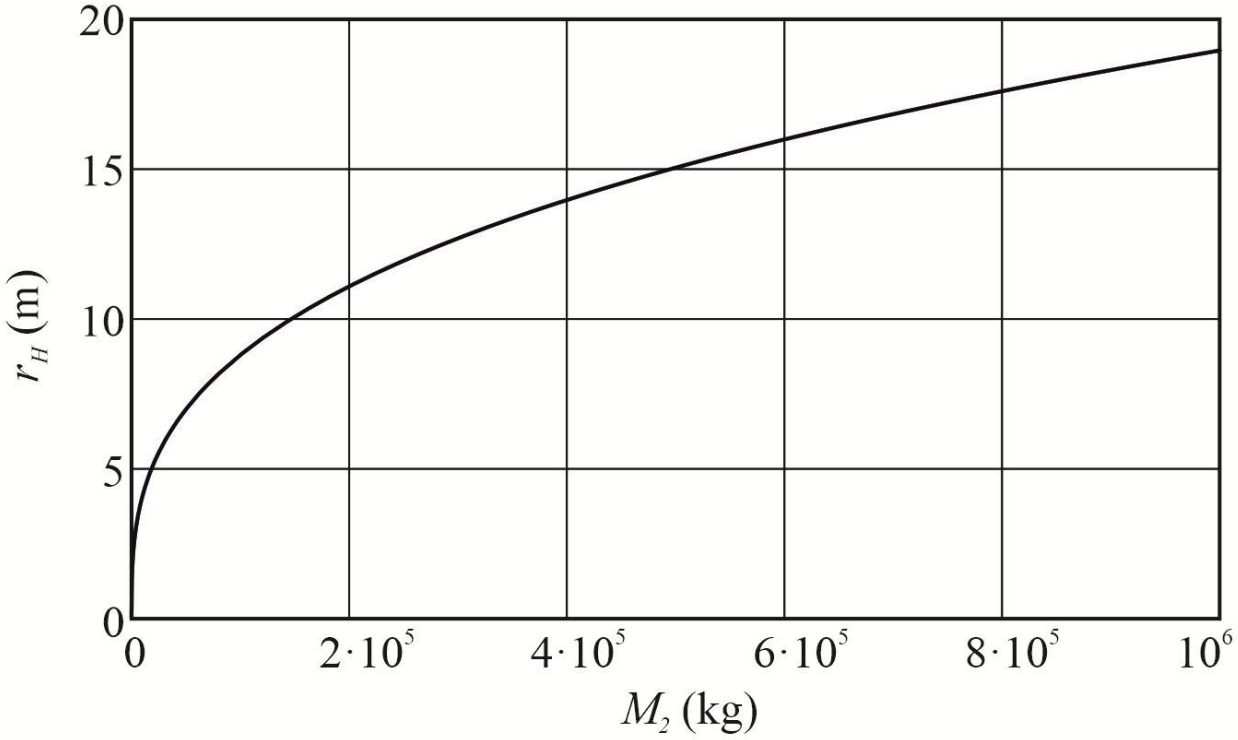

Figure 5.3. Dependence of the radius of the Hill sphere on the mass of the collector.

Basic idea and preliminary estimates

Figure 5.4. The Local-Vertical-Local-Horizontal frame and polar coordinates.

The position of space debris in polar coordinates

$$r_x = (1-\mu)\,p + \rho\cos\varphi$$
$$r_y = \rho\sin\varphi \qquad (5.1)$$

Jacobi integral

$$J = p^2(1-\mu)^2 n^2 - 2p(\mu-1)n^2\rho\cos\varphi + 2G\left(\frac{m_2}{\rho} + \frac{m_1}{\sqrt{p^2+2p\rho\cos\varphi+\rho^2}}\right) + \rho^2\left(n^2-\dot{\varphi}^2\right) - \dot{\rho}^2 \qquad (5.2)$$

Equations of motion of space debris in the gravitational field of the Earth and the collector

$$\ddot{\rho} = p(1-\mu)n^2\cos\varphi - \frac{GM_2}{\rho^2} - \frac{GM_1(p\cos\varphi+\rho)}{\sqrt{p^2+2p\rho\cos\varphi+\rho^2}} + \rho(n+\dot{\varphi})^2$$

$$\ddot{\varphi}\rho = p(\mu-1)n^2\sin\varphi + \frac{GM_1 p\sin\varphi}{\sqrt{p^2+2p\rho\cos\varphi+\rho^2}} - 2\dot{\rho}(n+\dot{\varphi}) \qquad (5.3)$$

$$\rho_0 = 7\ m,\ \ \dot{\rho}_0 = 0,\ \varphi_0 = 0,\ \dot{\varphi}_0 = 0,\ t \in [0, 2T] \qquad (5.4)$$

$$\rho_0 = 5\ m,\ \ \dot{\rho}_0 = 0,\ \varphi_0 = 0,\ \dot{\varphi}_0 = 0.0001\text{rad/s},\ t \in [0, 2T] \qquad (5.5)$$

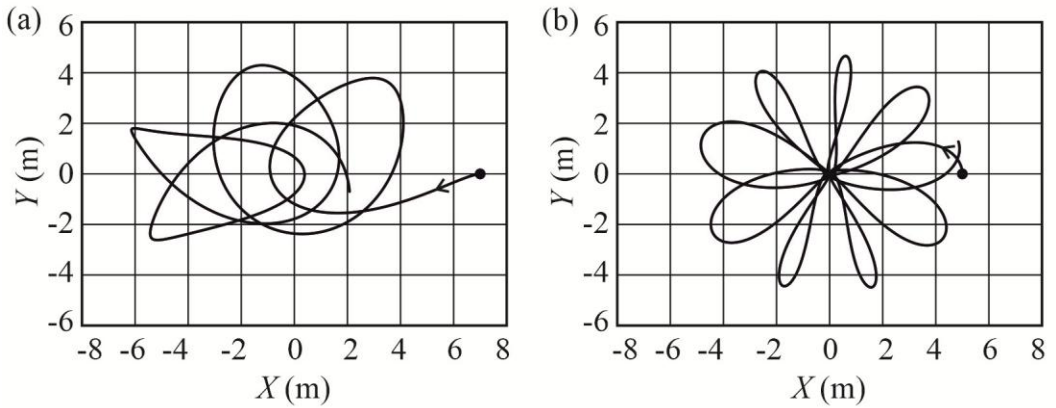

Figure 5.5.
Trajectories of space debris relative to the collector for initial conditions a) (5.4) and b) (5.5).

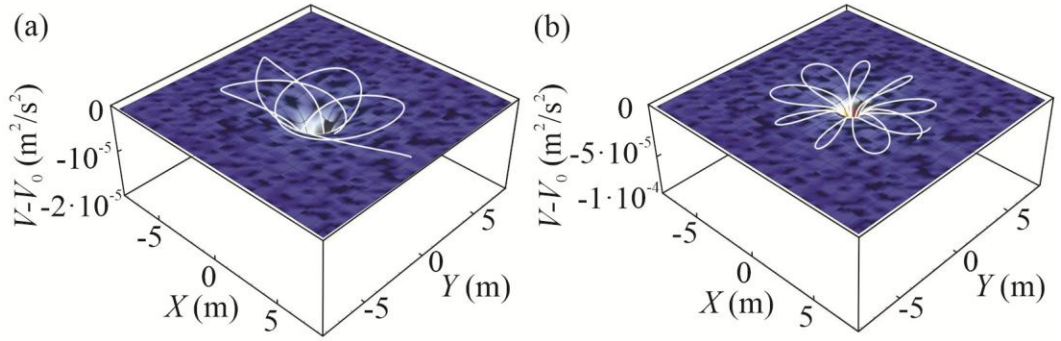

Figure 5.6.
Trajectories of space debris relative to the collector for initial conditions a) (5.4) and b) (5.5).

The space debris motion accounting the gravitational field of the Moon

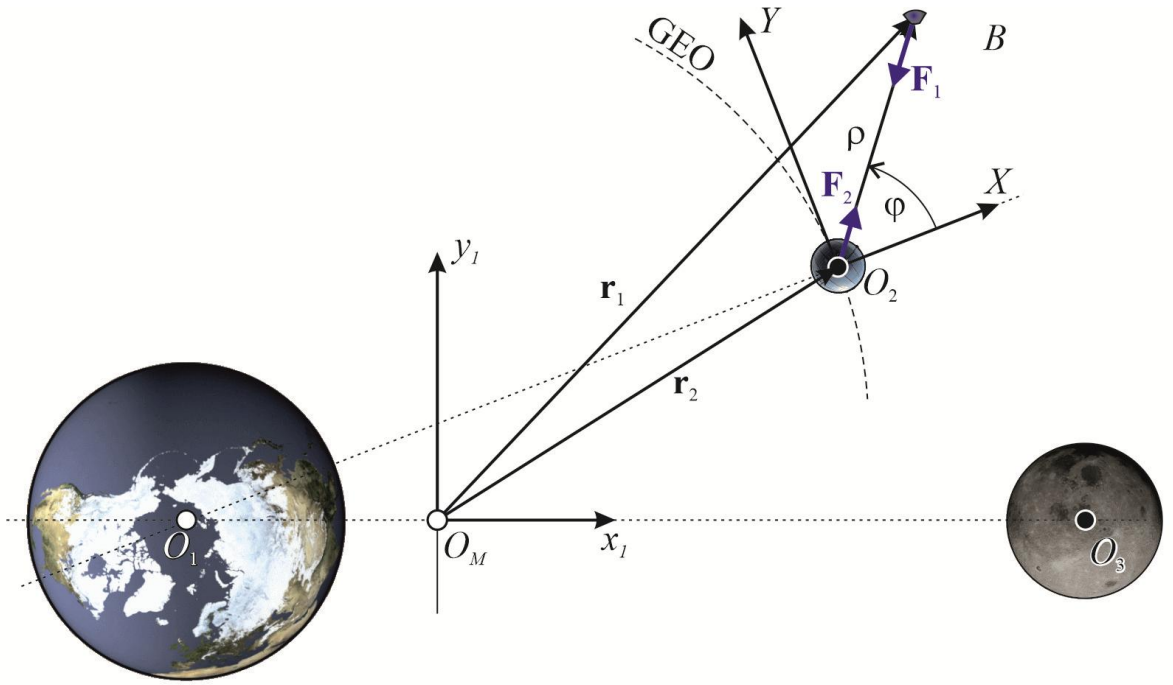

Figure 5.7. The Earth-Moon frame $O_M x_1 y_1$

$$x_1 = \frac{\partial W_{M1}}{\partial x_1} + n_m^2 x_1 + 2n_m \dot{y}_1 + a_{1x} \qquad x_2 = \frac{\partial W_{M2}}{\partial x_2} + n_m^2 x_2 + 2n_m \dot{y}_2 + a_{2x} \tag{5.6}$$

$$\ddot{y}_1 = \frac{\partial W_{M1}}{\partial y_1} + n_M^2 y_1 - 2n_M \dot{x}_1 + a_{1y} \qquad \ddot{y}_2 = \frac{\partial W_{M2}}{\partial y_2} + n_M^2 y_2 - 2n_M \dot{x}_2 + a_{2y} \tag{5.7}$$

$$W_i\left(x_i, y_i\right) = \frac{GM_1}{\sqrt{\left(x_i + p_M \mu_M\right)^2 + y_i^2}} + \delta \frac{GM_3}{\sqrt{\left(x_i - p_M\left(1-\mu_M\right)\right)^2 + y_i^2}} \tag{5.8}$$

5.2. Dynamic maneuvers of the heavy collector

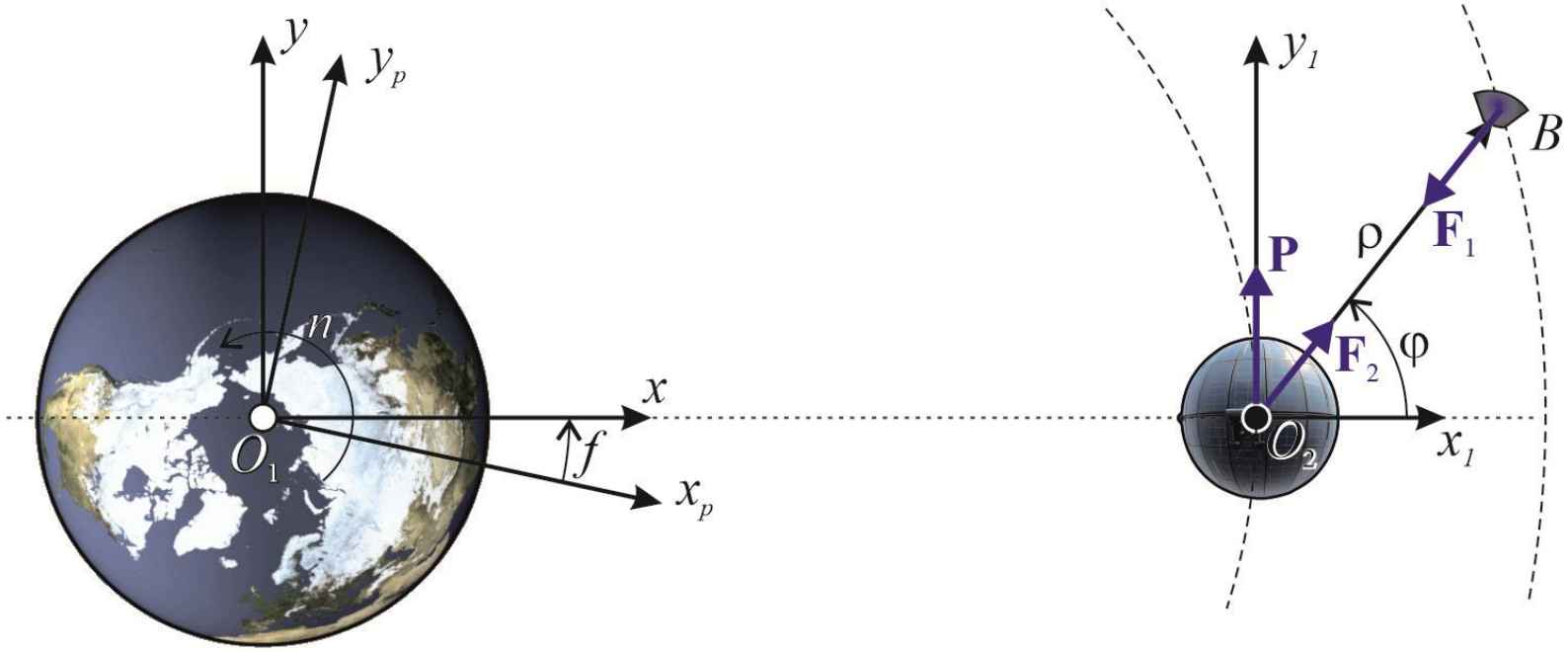

Figure 5.8. The local-vertical-local-horizontal reference frame.

$$\ddot{\rho} = -\frac{P}{m_1}\sin\varphi - \frac{G\left(M_2 + m\right)}{\rho^2} + \rho\left(3n^2\cos^2\varphi + 2n\dot{\varphi} + \dot{\varphi}^2\right)$$

$$\ddot{\varphi} = -\frac{3}{2}n^2\sin 2\varphi - 2\frac{n+\dot{\varphi}}{\rho}\dot{\rho} - \frac{P}{M_2\rho}\cos\varphi \qquad (5.10)$$

$$\dot{n} = \frac{P}{M_2 + m}\frac{1}{r}$$

5.3. The capture and towing of the debris by the collector

Initial conditions:

$$\rho_0 = 7.6\,\text{m} \qquad \varphi_0 = 0$$
$$\dot{\rho}_0 = 0 \qquad \dot{\varphi}_0 = 0 \qquad (5.11)$$

The debris velocity after impact:

$$V_{n1} = -kV_{n0} \qquad (5.12)$$

- $V_{n0} = \dot{\rho}_0$ normal projection of the velocities just before impact.
- $V_{n1} = \dot{\rho}_1$ normal projection of the velocities right after impact.
- $k \in (0,1)$ is the coefficient of restitution, which is defined as the ratio of the velocity of the debris after impact to its velocity before impact.

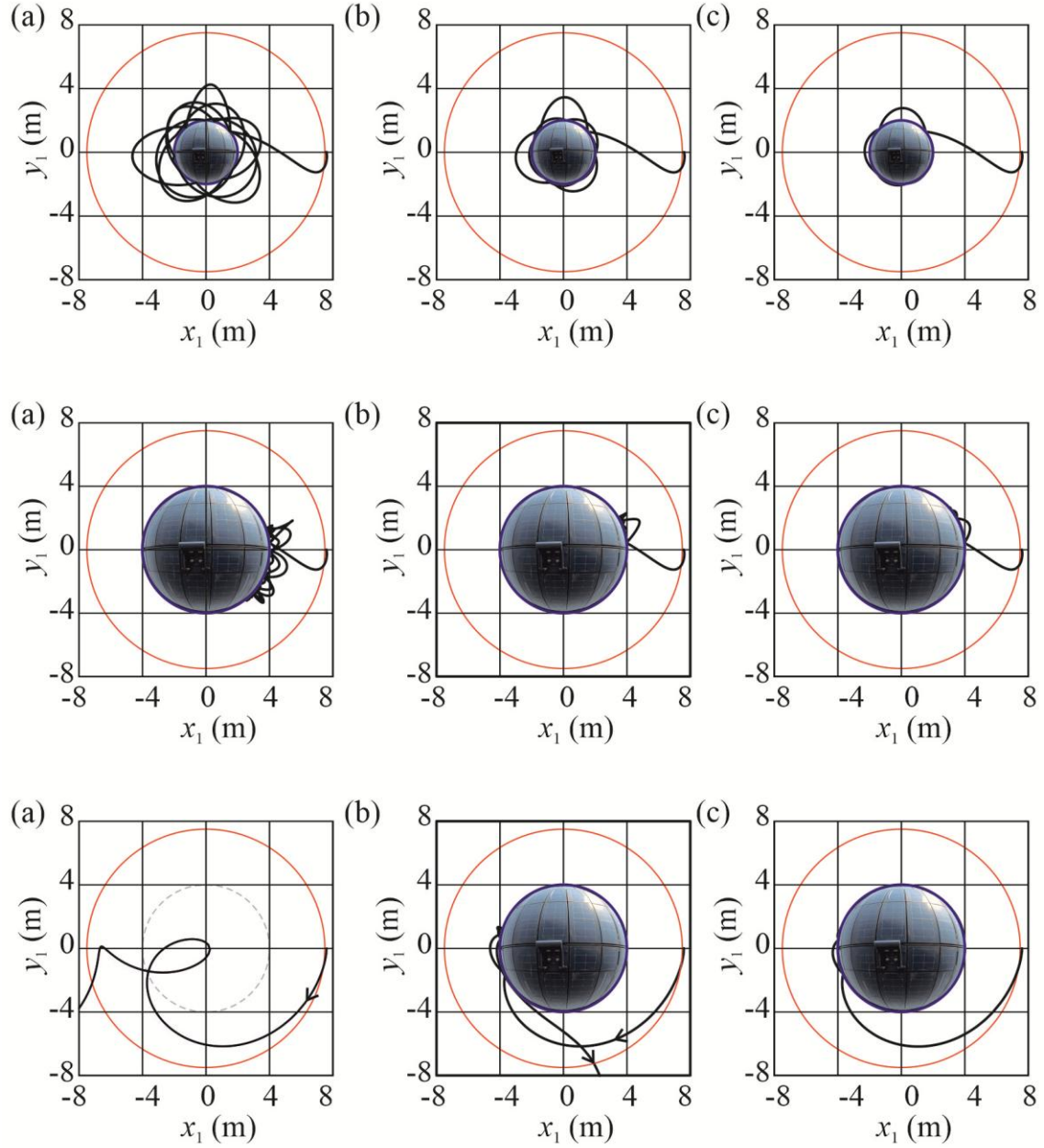

Figure 5.9. Trajectories of space debris motion from initial points (5.11) for different values of the trust force, the restitution coefficient and size.

5.4. Discarding collected debris in the disposal orbit

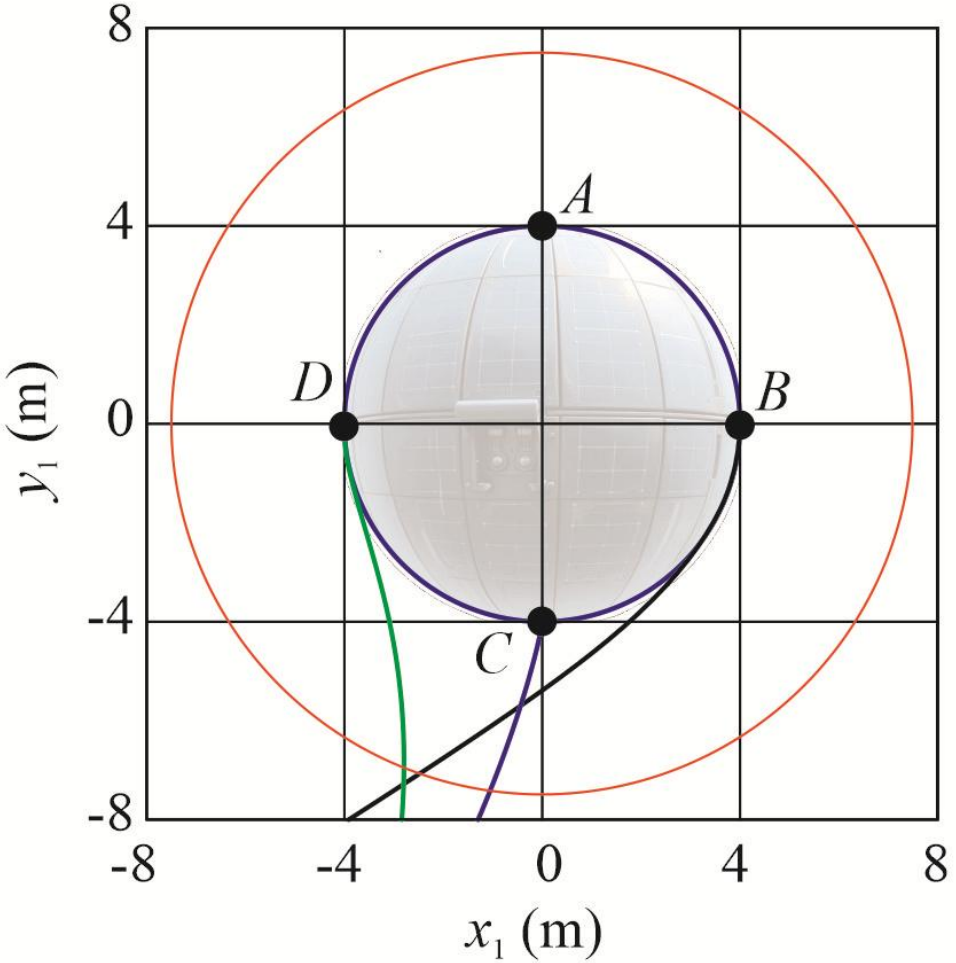

Figure 5.10. The space debris discarding by accelerating the collector ($P = 0.045$ N).

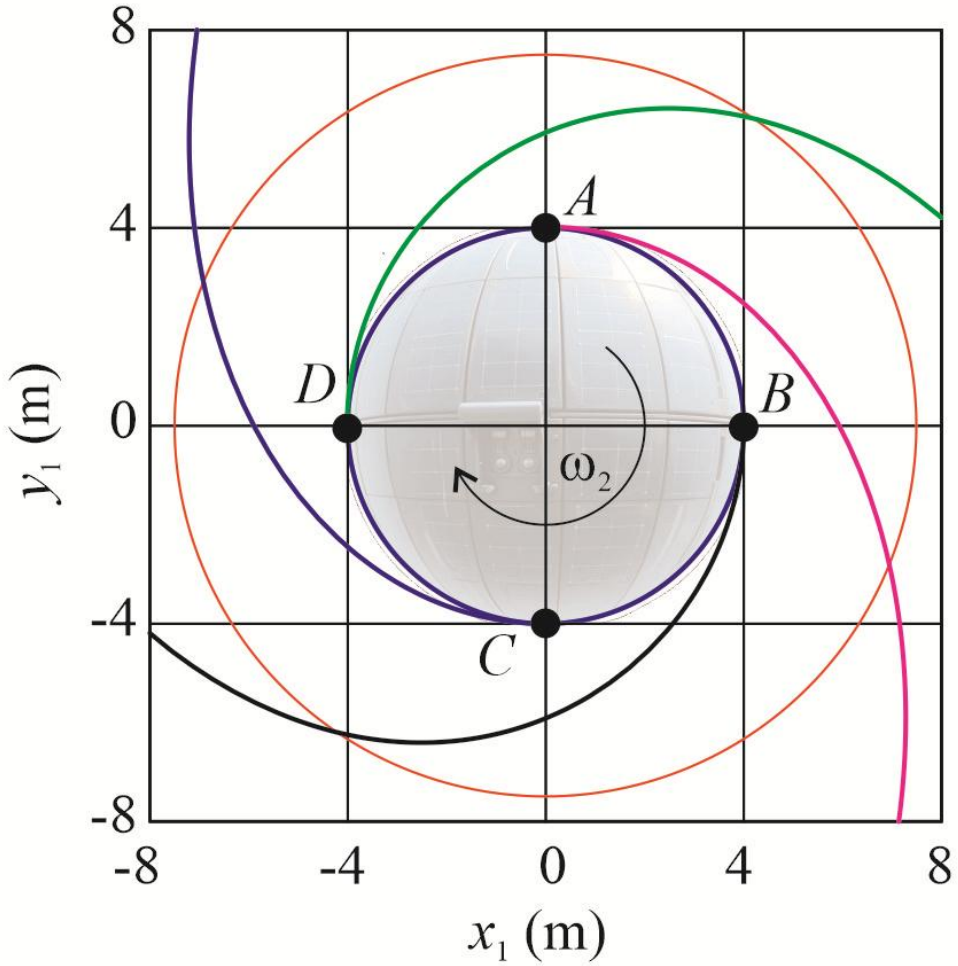

Figure 5.11. The space debris discarding by accelerating the collector ($P = 0$ N, $\omega_2 = -0.0005$ *rad* / *s*).

Chapter 6

Two-Impulse Moon-Planet Transfer:

A New Scenario

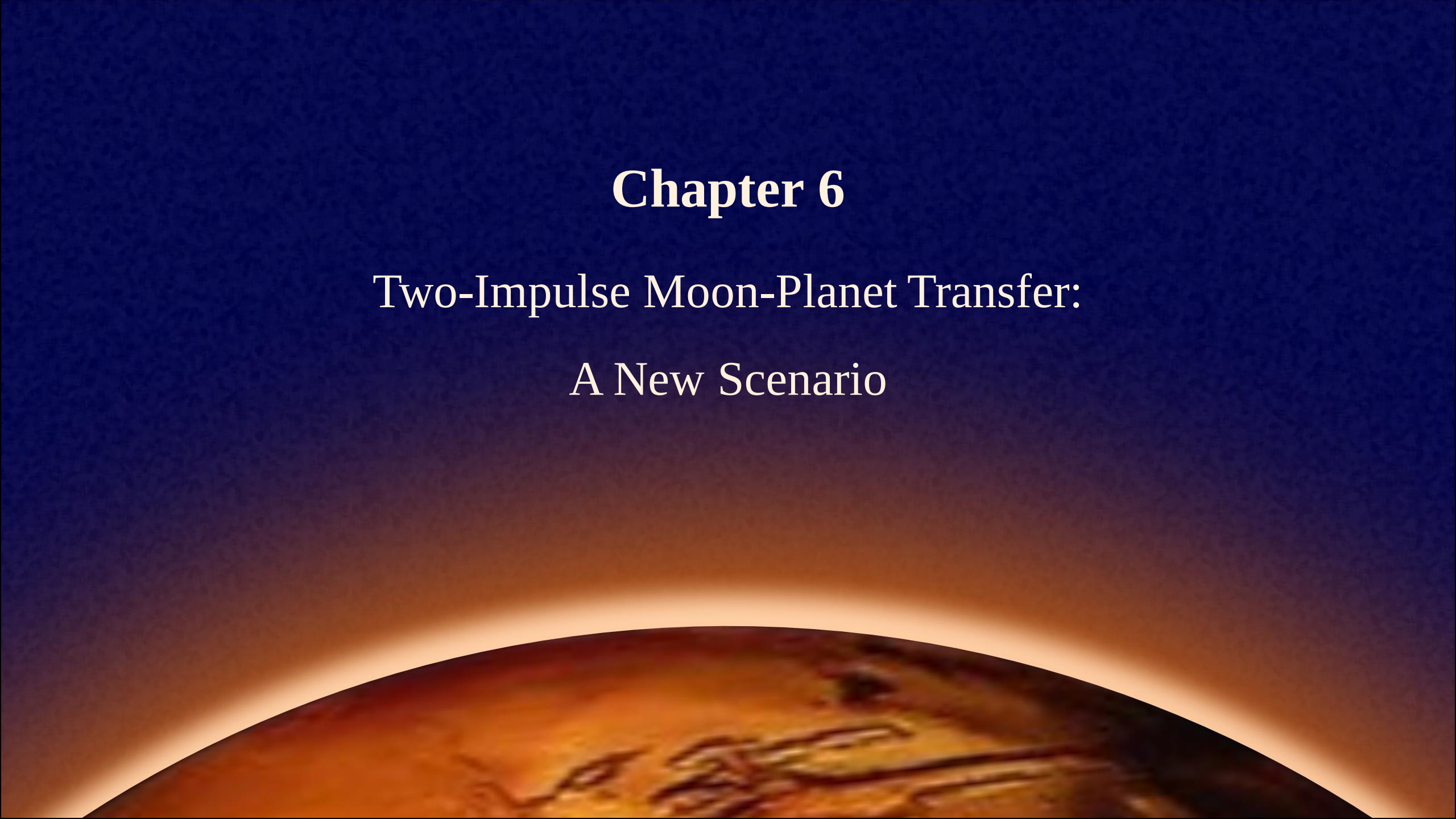

6.1. Scheme of two-impulse Moon-Planet transfer

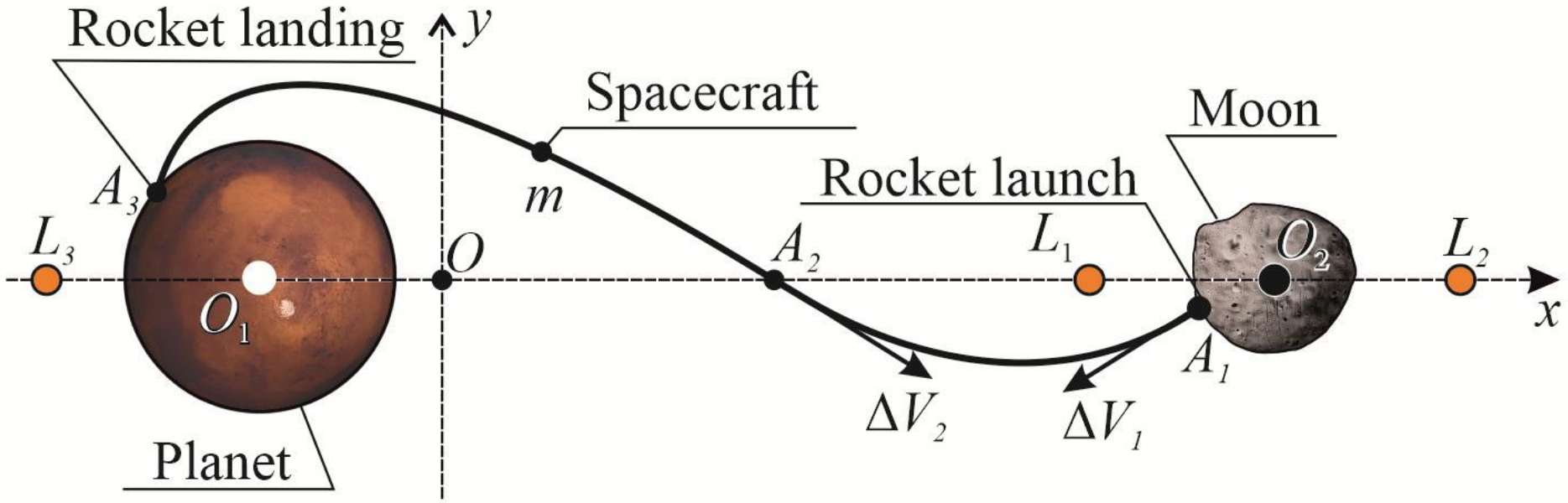

Figure 6.1. The two-impulse Moon-Planet transfer in the frame Oxy.

$$\ddot{x} - \dot{f}^2 x - 2\dot{f}\,\dot{y} - \ddot{f}\,y = \frac{\partial U}{\partial x}$$

$$\ddot{y} - \dot{f}^2 y + 2\dot{f}\,\dot{x} + \ddot{f}\,x = \frac{\partial U}{\partial y} \qquad (6.1)$$

$$\ddot{f} = -\frac{2c^2 e \sin f}{p\,r^3}$$

- $U(x,y) = G\left(\frac{M_1}{r_1} + \frac{M_2}{r_2}\right)$
- $r_1 = \sqrt{(x+\mu r)^2 + y^2}$
- $r_2 = \sqrt{(x-(1-\mu)r)^2 + y^2}$
- $c = \sqrt{G(M_1 + M_2)\,p}$

1. Rest at unstable libration points

$$x_{A_2} = x_{L_1} \qquad x_{A_2} = x_{L_2} \qquad x_{A_2} = x_{L_3} \tag{6.2}$$

where x_{L_i} is the coordinate of the *i*-th libration point in *Oxy*

2. Motion around the planet including landing trajectories on the planet that intersect its surface

$$x_{L_3} < x_{A_2} < x_{L_1} \tag{6.3}$$

3. Motion around the moon

$$x_{L_1} < x_{A_2} < x_{L_2} \tag{6.4}$$

4. Motion around the planet and the moon along the outer trajectory

$$x_{A_2} > x_{L_2} \wedge x_{A_2} < x_{L_3} \tag{6.5}$$

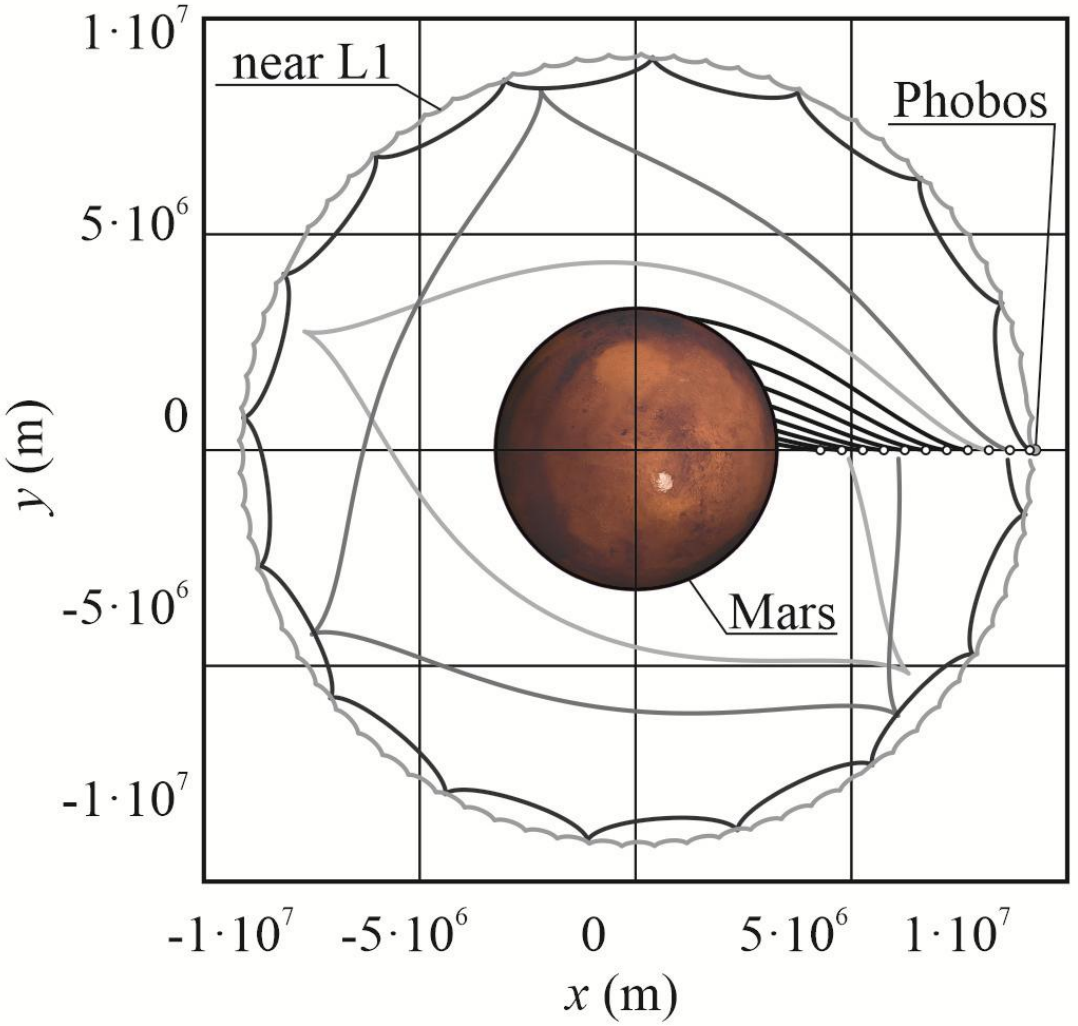

Figure 6.2. The two-impulse Moon-Planet transfer in the frame Oxy.

6.2. Equations of motion of a spacecraft accounting the influence of the planet's atmosphere

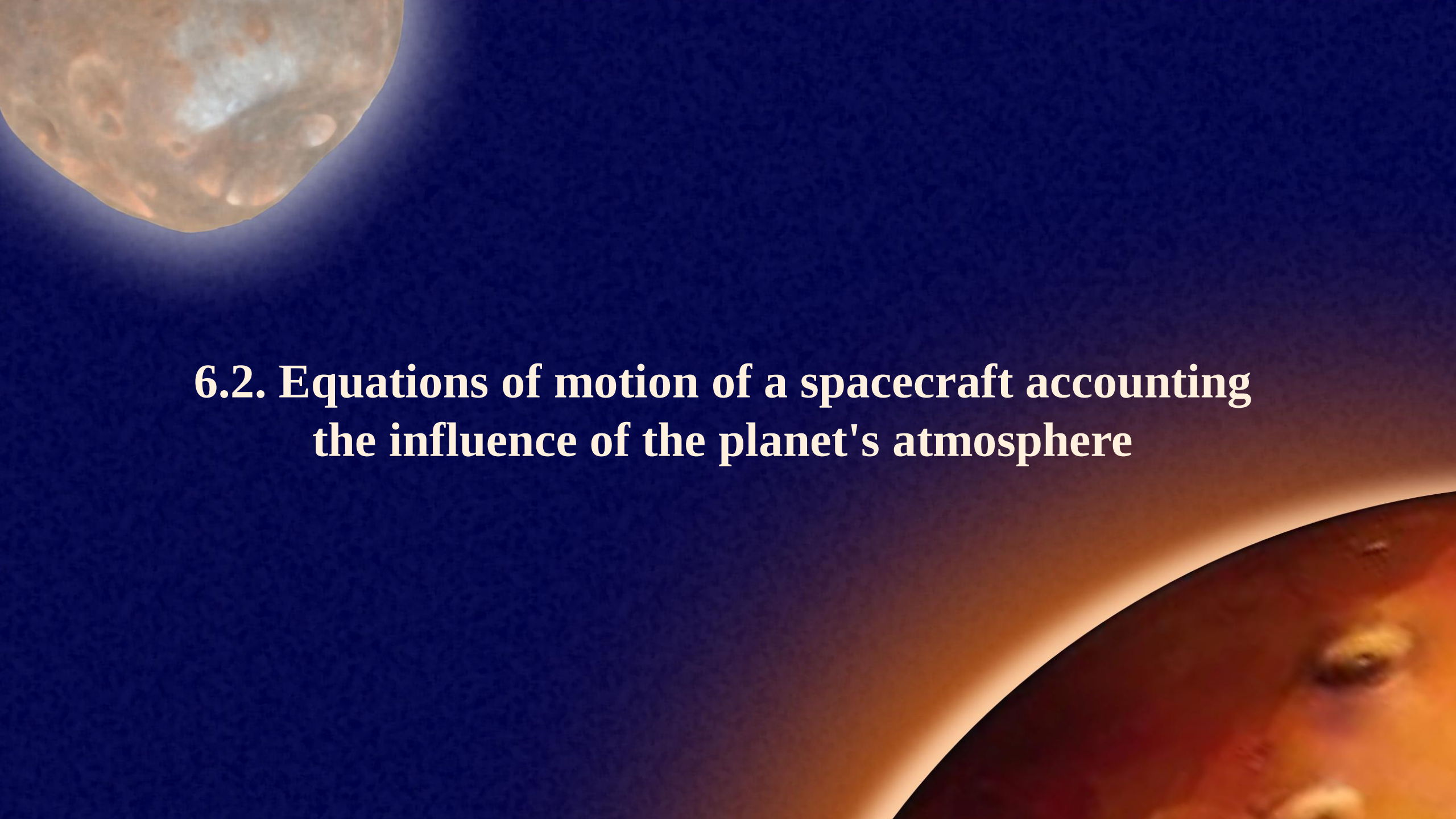

Equations of motion in the planar elliptic restricted three-body problem with consideration of aerodynamic force

$$\ddot{x} - \dot{f}^2 x - 2\dot{f}\,\dot{y} - \ddot{f}\,y = -\frac{C_D S}{m}\frac{\rho V^2}{2}\cos\beta + \frac{\partial U}{\partial x}$$

$$\ddot{y} - \dot{f}^2 y + 2\dot{f}\,\dot{x} + \ddot{f}\,x = -\frac{C_D S}{m}\frac{\rho V^2}{2}\sin\beta\frac{\partial U}{\partial y} \qquad (6.6)$$

- C_d is the aerodynamic drag coefficient.
- ρ is the atmospheric density.
- S is the cross-section of spacecraft.
- V is the velocity of the spacecraft.

$$\tan\beta = \frac{\dot{y} + r\dot{f}\cos\alpha}{\dot{x} - r\dot{f}\sin\alpha} \qquad (6.7)$$

- β is the angle between the axis Ox and the velocity vector.

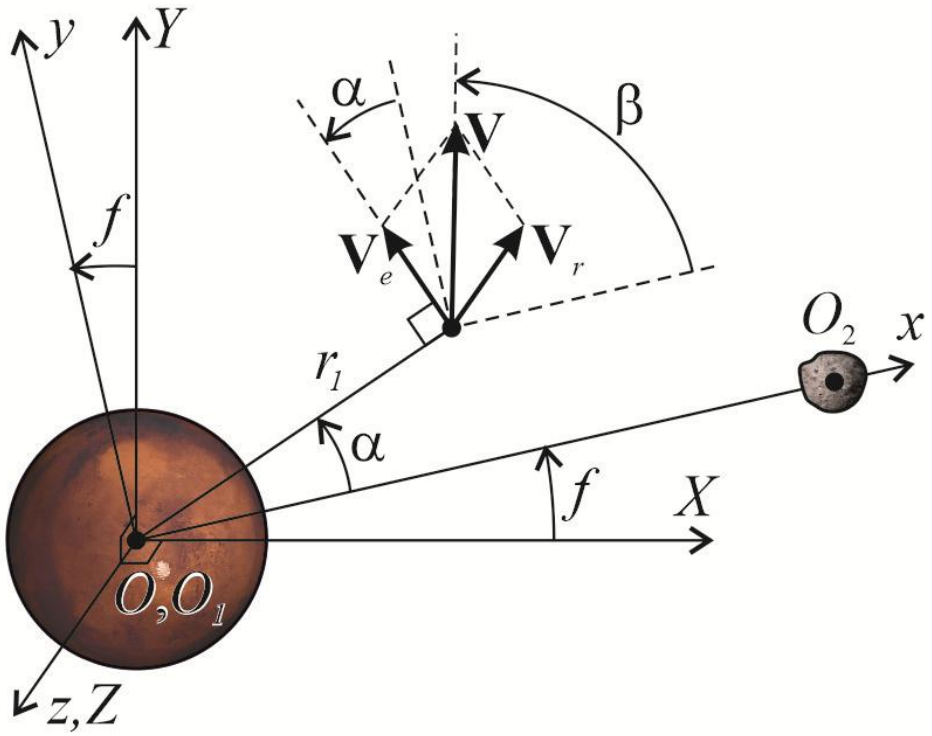

Figure 6.3. The reference frames.

Equations of the spacecraft's atmospheric entry

$$\dot{h} = V \sin\gamma$$
$$\dot{V} = -\frac{C_D S}{m}\frac{\rho V^2}{2} - g\sin\gamma \qquad (6.8)$$
$$\dot{\gamma} = \left(\frac{V}{h+R_p} - \frac{g}{V}\right)\cos\gamma$$

- h is the altitude.
- γ is the flight path angle .
- g is the gravitational acceleration defined as

$$g = g_0\left(\frac{R_0}{h+R_0}\right)^2 \qquad (6.9)$$

- g_0 is the gravitational acceleration at the ground level.

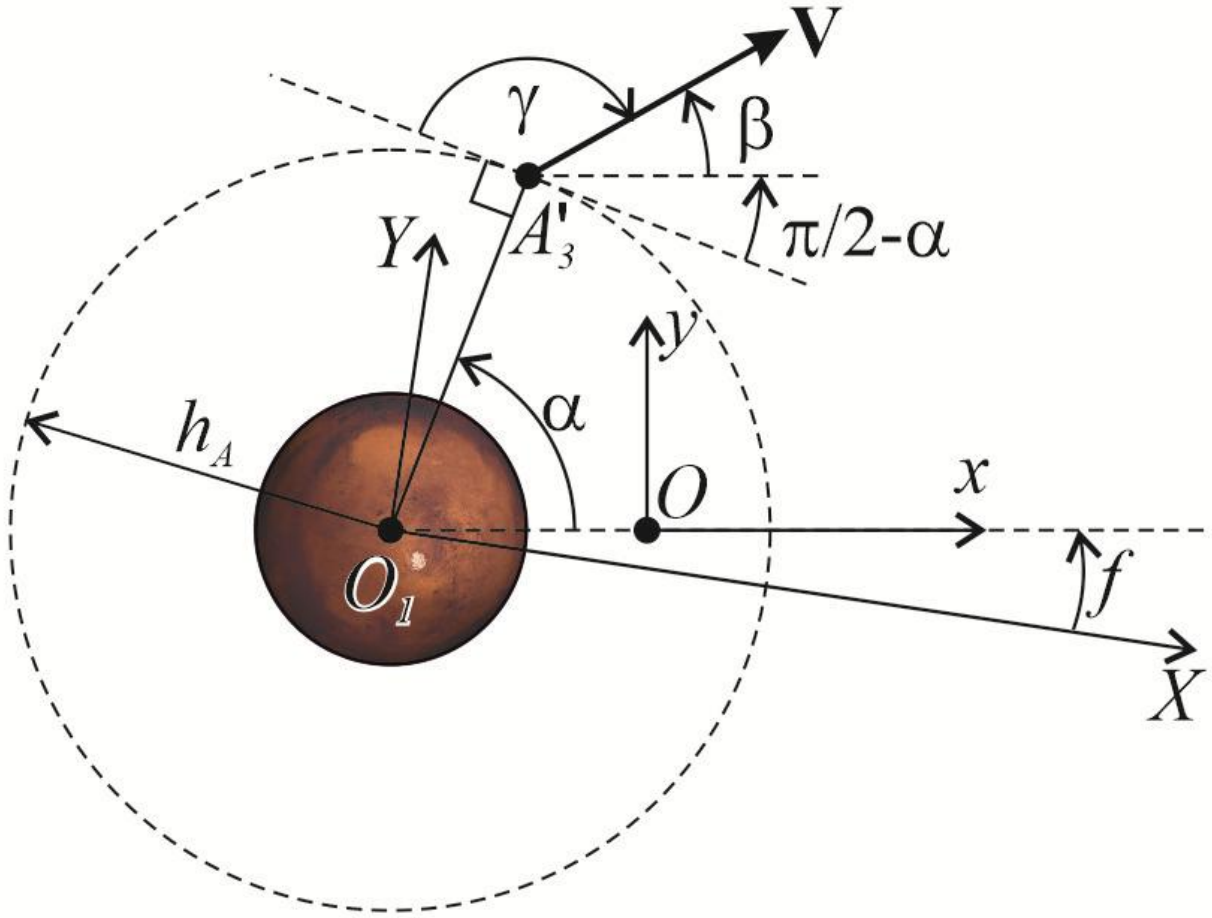

Figure 6.4. The reference frames.

6.3. Simulation of the Phobos-Mars transfer mission

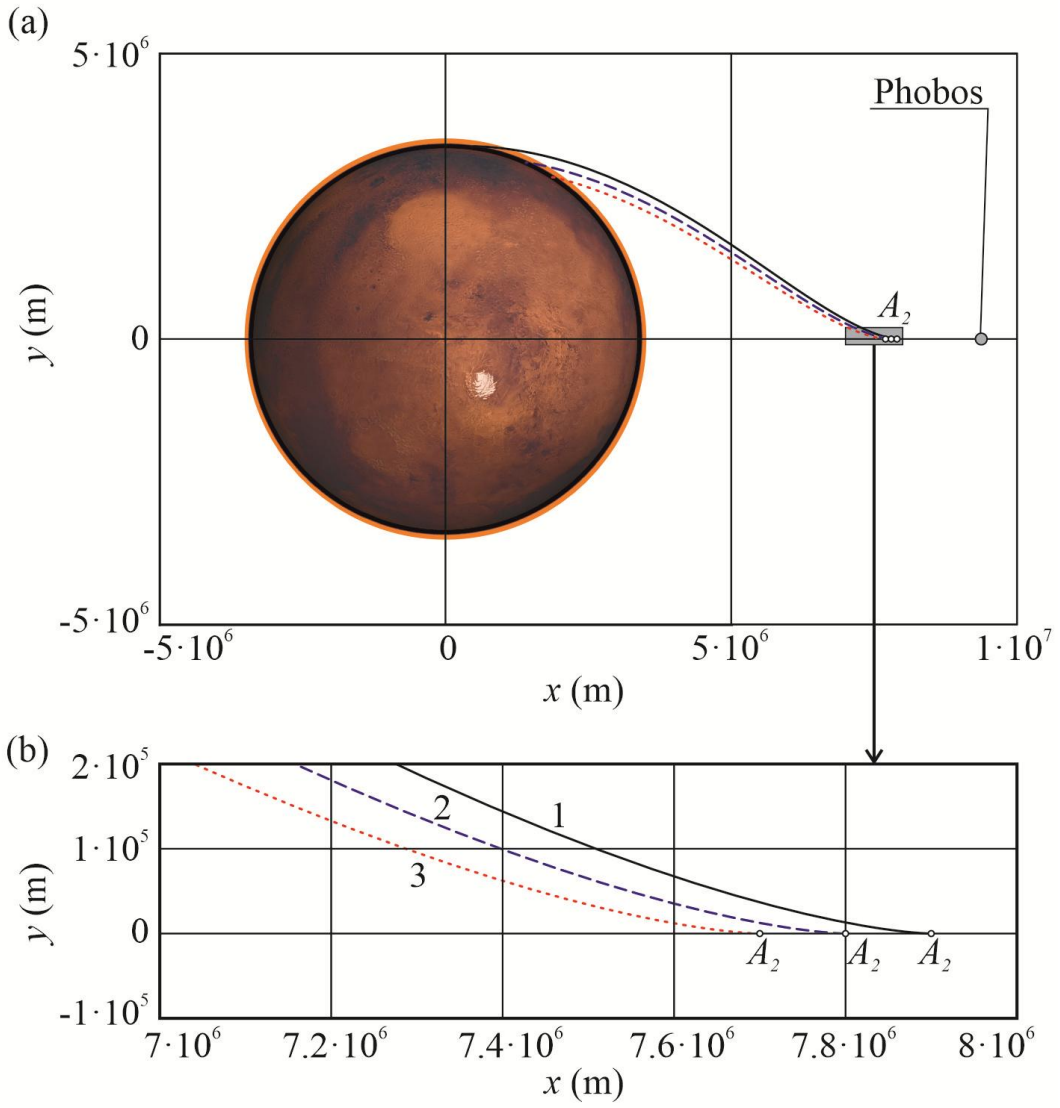

Figure 6.5. Landing trajectories for various transition points A_2

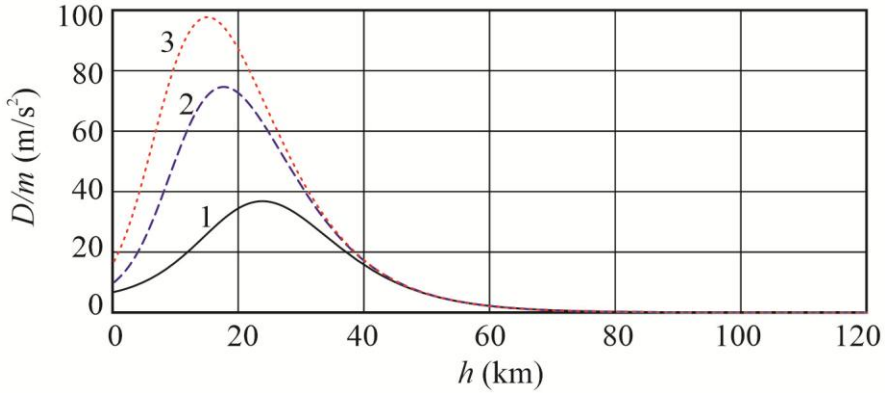

Figure 6.6. The aerodynamic force acceleration for various transition points A_2

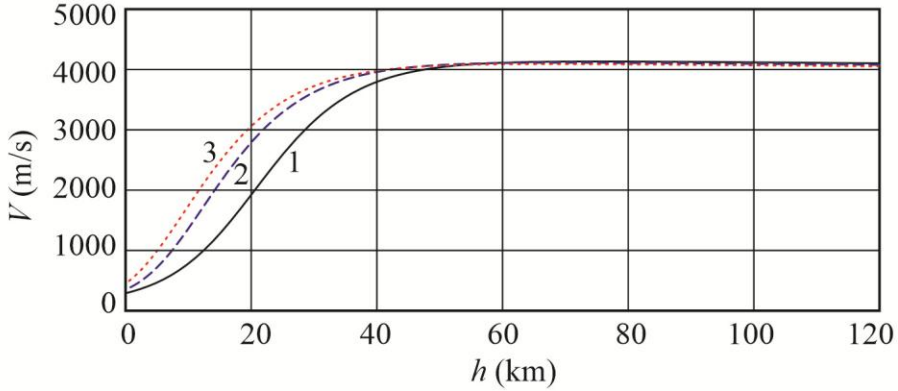

Figure 6.7. The spacecraft's velocity for various transition points A_2

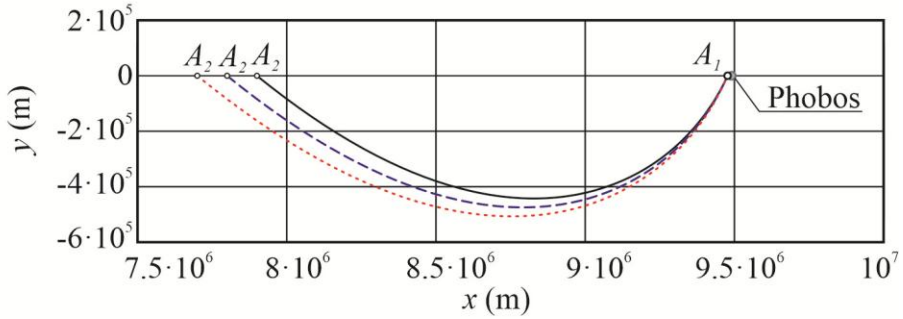

Figure 6.8. The launch trajectories for various transition points A_2

6.4. Simulation of the Moon-Earth transfer mission

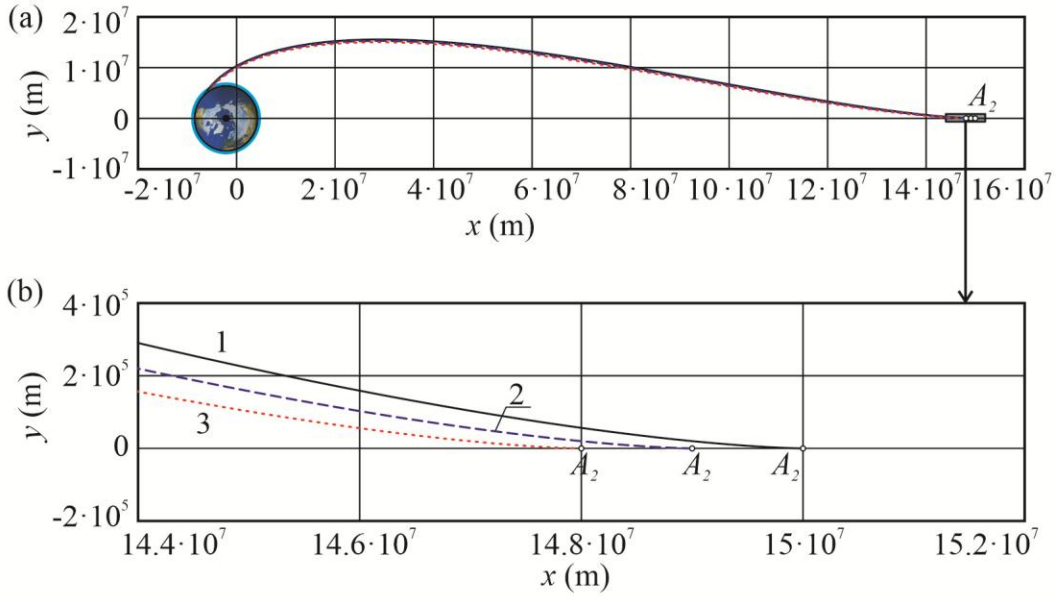

Figure 6.5. The landing trajectories for various transition points A_2

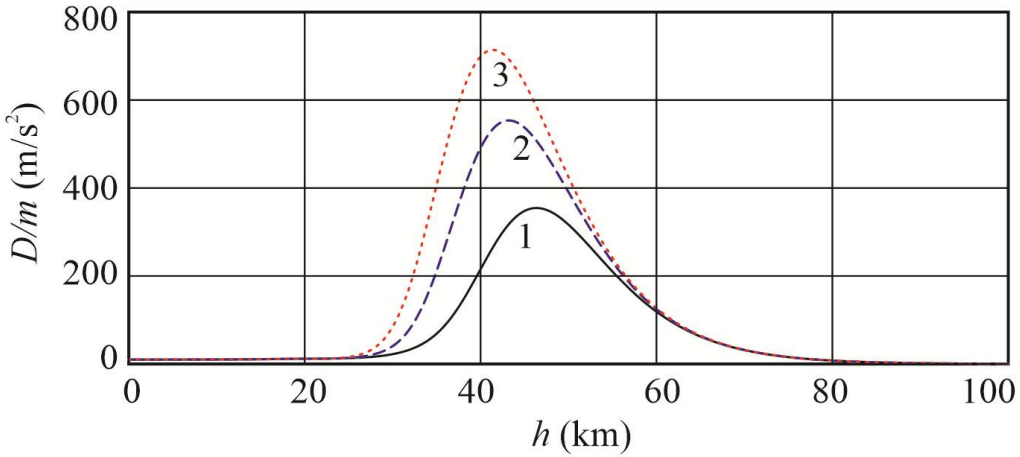

Figure 6.9. The aerodynamic force acceleration for various transition points A_2

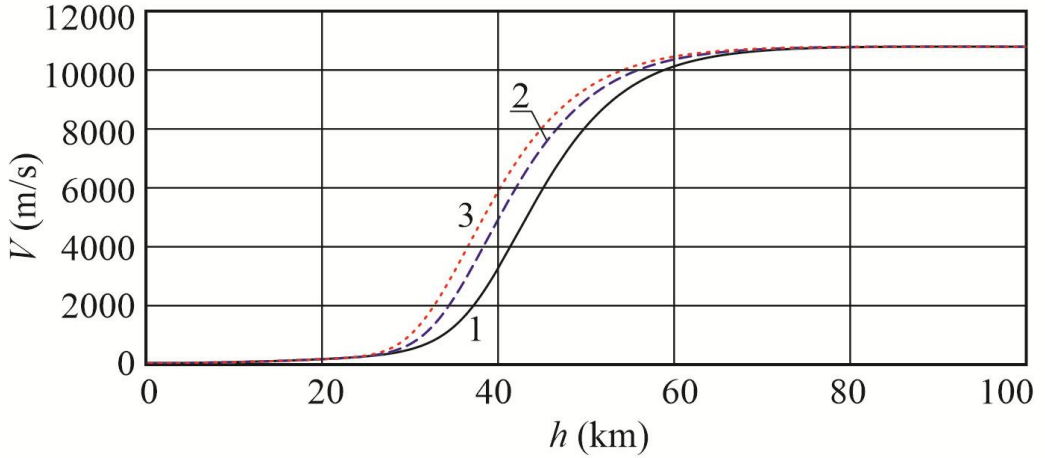

Figure 6.10. The spacecraft's velocity for various transition points A_2

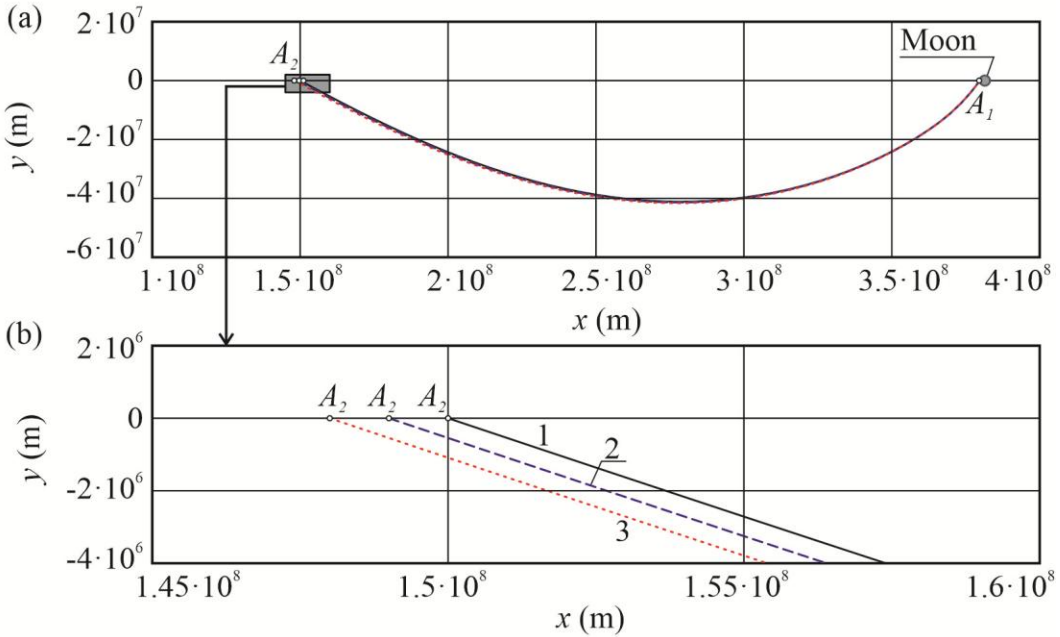

Figure 6.11. The launch trajectories for various transition points A_2

The book contains the following papers

(published on *aslanov.ssau.ru*)

1. **V.S. Aslanov**, *A novel scenario of two-impulse Moon-Planet transfer*, **Aerospace Science and Technology**, Vol. 168, pp. 111258, 2026.
2. **V.S. Aslanov**, *An anchored space elevator under the L1 Mars-Phobos libration point*, **Acta Astronautica**, Vol. 235, pp. 38-46, 2025.
3. **V.S. Aslanov**, *A double pendulum anchored at the surface of a moon below the L1 libration point: the impossibility of building a space elevator*, **Nonlinear Dynamics**, Vol. 113, No. 11, pp. 12959-12970, 2025.
4. **V.S. Aslanov**, *A space elevator deployed at the L1 Mars–Phobos libration point*, **Nonlinear Dynamics**, Vol. 112, No. 17, pp. 1-11, 2024.
5. **V.S. Aslanov**, *Suppressing chaotic oscillations of a tether anchored to the Phobos surface under the L1 libration point*, **Chaos, Solitons & Fractals**, Vol. 181, pp. 114-663, 2024.
6. **V.S. Aslanov**, *A double pendulum fixed at the L1 libration point: a precursor to a Mars–Phobos space elevator*, **Nonlinear Dynamics**, Vol. 112, pp. 775-791, 2024.
7. **V.S. Aslanov**, *Tether System in Martian-Moons-eXploration-Like Mission for Phobos Surface Exploration*, **Journal of Spacecraft and Rockets**, Vol. 61, No. 1, pp. 319-326, 2024.
8. **V.S. Aslanov**, *Attitude Motion of Cylinder in Variable Electrostatic Field Near L1 Libration Point*, **Journal of Spacecraft and Rockets**, Vol.60, No. 4, pp. 1230-1241, 2023.
9. **V.S. Aslanov**, *Dynamics of a Phobos-anchored tether near the L1 libration point*, **Nonlinear Dynamics**, Vol. 111, No. 2, pp. 1269-1283, 2022.
10. **V.S. Aslanov**, *Capture Trajectories into Vicinity of Collinear Libration Points by Variable Electrostatic Field*, **Jounans of Spacecraft and Rockets**, Vol. 59, No. 3, pp. 1039-1043, 2022.
11. **V.S. Aslanov**, *Prospects of a tether system deployed at the L1 libration point*, **Nonlinear Dynamics**, Vol. 106, No. 3, pp. 2021-2033, 2021
12. **V.S. Aslanov**, *Prospects of Phobos Sample Return Mission Using Electrostatic Container*, **Journal of Spacecraft and Rockets**, Vol. 58, No. 6, pp. 1799-1805, 2021
13. **V.S. Aslanov**, *A splitting of collinear libration points in circular restricted three-body problem by an artificial electrostatic field*, **Nonlinear Dynamics**, Vol. 103, pp. 2451-2460, 2021.
14. **V. S. Aslanov**, *Stability of a pendulum with a moving mass: the averaging method*, **Journal of Sound and Vibration**, Vol. 445, pp. 261-269, 2019.
15. **V. S. Aslanov**, *Debris Removal in GEO by Heavy Orbital Collector*, **Acta Astronautica**, Vol. 164, pp. 184-191, 2019.
16. **V. S. Aslanov**, *Gravitational Trap for Space Debris in Geosynchronous Orbit*, **Journal of Spacecraft and Rockets**, Vol. 56, No. 4, 2019.

Advanced Mission Scenarios of the Three-Body Problem introduces one of the classical problems of celestial mechanics through the prism of the problems and challenges of modern astrodynamics.

This book is intended for space systems and spacecraft engineering industry experts and researchers studying space transportation and modern challenges in astronautics.

Preview published on *aslanov.ssau.ru*

Buy it online at *routledge.com*

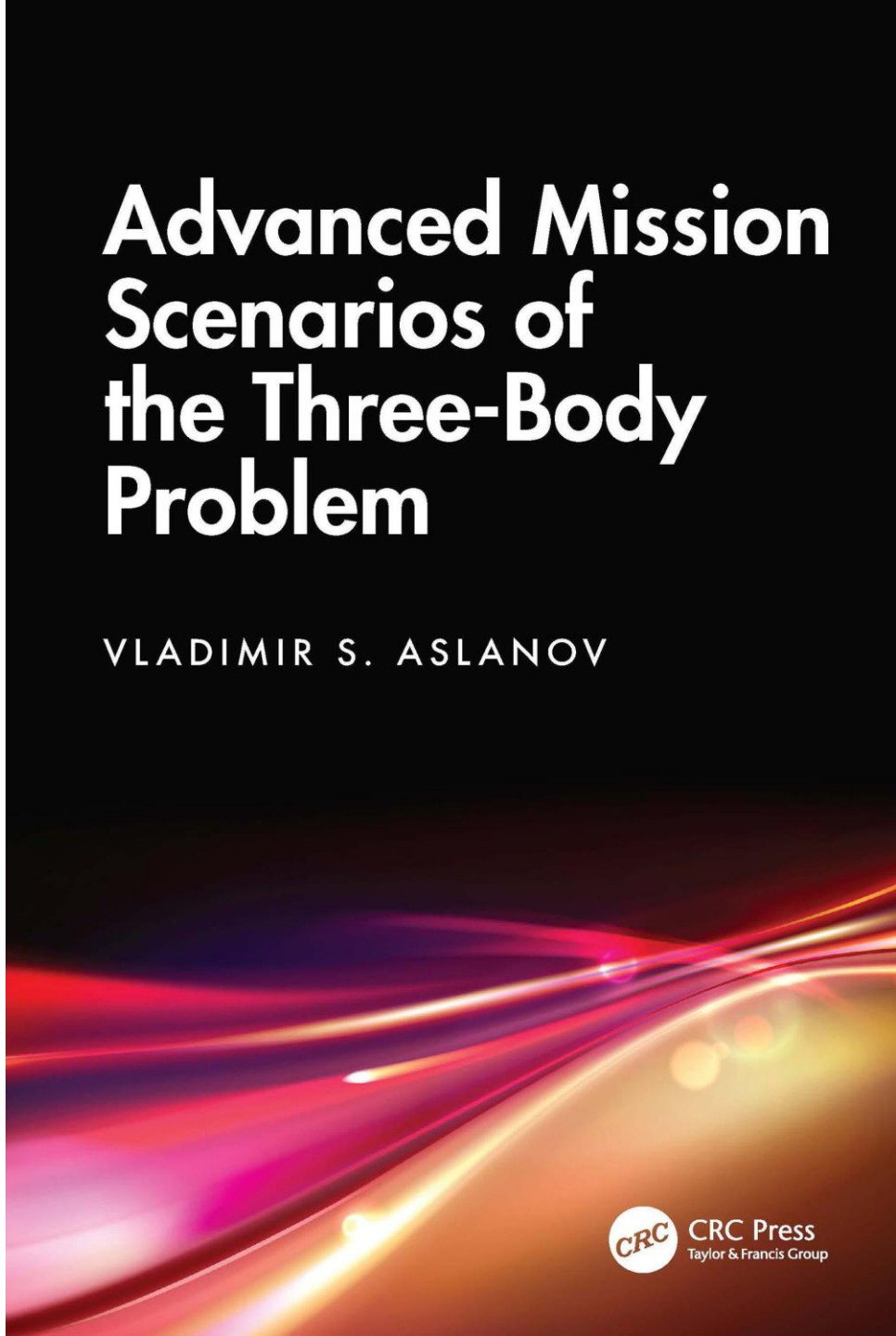

Thank You

Prof. Vladimir S. Aslanov

aslanov.vladimir@gmail.com

aslanov.ssau.ru